TU Delft

Delft University of Technology

Layer-specific imaging and monitoring using seismic interferometry and the Marchenko method

Shirmohammadi, F.

DOI
10.4233/uuid:425a6761-cb96-4326-aeb8-e2a312588765

Publication date
2024

Document Version
Final published version

Citation (APA)
Shirmohammadi, F. (2024). *Layer-specific imaging and monitoring using seismic interferometry and the Marchenko method*. [Dissertation (TU Delft), Delft University of Technology]. https://doi.org/10.4233/uuid:425a6761-cb96-4326-aeb8-e2a312588765

Important note
To cite this publication, please use the final published version (if applicable).
Please check the document version above.

Copyright
Other than for strictly personal use, it is not permitted to download, forward or distribute the text or part of it, without the consent of the author(s) and/or copyright holder(s), unless the work is under an open content license such as Creative Commons.

Takedown policy
Please contact us and provide details if you believe this document breaches copyrights.
We will remove access to the work immediately and investigate your claim.

This work is downloaded from Delft University of Technology.
For technical reasons the number of authors shown on this cover page is limited to a maximum of 10.

LAYER-SPECIFIC IMAGING AND MONITORING USING SEISMIC INTERFEROMETRY AND THE MARCHENKO METHOD

LAYER-SPECIFIC IMAGING AND MONITORING USING SEISMIC INTERFEROMETRY AND THE MARCHENKO METHOD

Dissertation

for the purpose of obtaining the degree of doctor
at Delft University of Technology
by the authority of the Rector Magnificus, Prof. dr. ir. T.H.J.J. van der Hagen,
chair of the Board for Doctorates,
to be defended publicly on
Wednesday, 18 December 2024 at 10:00 o'clock

by

Faezeh SHIRMOHAMMADI

Master of Science in Geophysics, University of Tehran, Iran
born in Tehran, Iran.

This dissertation has been approved by the promotors.

Composition of the doctoral committee:

Rector Magnificus,	chairperson
Dr. ir. D.S. Draganov,	Delft University of Technology, *promotor*
Prof. dr. ir. C.P.A. Wapenaar,	Delft University of Technology, *promotor*
Independent members:	
Prof. dr. A. Curtis,	University of Edinburgh
Prof. dr. L.V. Socco,	Delft University of Technology
Prof. dr. ir. F.C. Vossepoel,	Delft University of Technology
Prof. dr. ir. E.C. Slob,	Delft University of Technology
Dr. ir. E.N. Ruigrok,	KNMI, Utrecht University

This work has received funding from NWO Science domain (NWO-ENW), Grant Number: DEEP.NL.2018.048 and European Research Council (ERC) under the European Union's Horizon 2020 research and innovation programme (Grant Agreement No. 742703).









Keywords: Seismic interferometry, monitoring, imaging, Marchenko method

Printed by: Gildeprint

Front & Back: The Groningen velocity model used for numerical modelling in Chapter 3

Copyright © 2024 by F. Shirmohammadi

ISBN 978-94-6384-688-2

An electronic version of this dissertation is available at http://repository.tudelft.nl/.

To my family and friends

CONTENTS

Summary ix

Samenvatting xi

1 Introduction 1
- 1.1 Seismic interferometry . . . 2
- 1.2 The Marchenko method . . . 4
- 1.3 Aim and outline of the thesis . . . 5
- References . . . 7

2 Shallow-subsurface characterisation using ghost reflections 11
- 2.1 Introduction . . . 12
- 2.2 Method . . . 14
- 2.3 Results . . . 16
  - 2.3.1 Numerically modelled data . . . 16
  - 2.3.2 Field data . . . 22
- 2.4 Discussion . . . 24
- 2.5 Conclusion . . . 26
- 2.6 Supplementary Material . . . 26
  - 2.6.1 Comparison of the zero-offset sections . . . 26
  - 2.6.2 Ghost reflections retrieved from SI by CC . . . 27
- 2.7 Data availability . . . 29
- References . . . 29

3 Reservoir monitoring using ghost reflections 33
- 3.1 Introduction . . . 34
- 3.2 Method . . . 35
- 3.3 Results . . . 38
  - 3.3.1 Numerically modelled data . . . 38
  - 3.3.2 Time-lapse investigation using ghost reflections . . . 42
  - 3.3.3 Sources and receivers configuration . . . 46
- 3.4 Discussion . . . 49
- 3.5 Conclusion . . . 50
- 3.6 Supplementary Material . . . 51
  - 3.6.1 Correlation panels . . . 51
- 3.7 Data availability . . . 54
- References . . . 54

4 Investigating the amplitude of ghost reflections **57**
4.1 Introduction . . . 58
4.2 Method . . . 58
4.3 Results . . . 59
4.4 Discussion . . . 66
4.5 Conclusion . . . 67
4.6 Supplementary Material . . . 67
4.6.1 The amplitudes of ghost reflections retrieved from SI by CC . . . 67
4.7 Data availability . . . 69
References . . . 69

5 Recursive interferometric surface-wave suppression **71**
5.1 Introduction . . . 72
5.2 Recursive interferometric surface-wave suppression (RISS) . . . 73
5.2.1 Surface-wave retrieval by seismic interferometry . . . 73
5.2.2 Adaptive subtraction . . . 75
5.3 Seismic data acquisition . . . 76
5.4 Results . . . 78
5.5 Discussion . . . 84
5.6 Conclusion . . . 85
5.7 Data availability . . . 85
References . . . 86

6 Application of Marchenko-based isolation to a land seismic dataset **87**
6.1 introduction . . . 88
6.2 Method . . . 89
6.2.1 Green's functions representation . . . 89
6.2.2 Over- and underburden removal . . . 90
6.3 Seismic data acquisition . . . 92
6.4 Data pre-processing . . . 93
6.5 Results . . . 94
6.6 Discussion . . . 97
6.7 Conclusion . . . 98
6.8 Data availability . . . 98
References . . . 98

7 Conclusions and future outlook **101**
7.1 Conclusions . . . 101
7.2 Future outlook . . . 104

Acknowledgements **107**

Curriculum Vitæ **109**

Publications **111**

SUMMARY

Seismic imaging and monitoring with reflected waves, originally used in the oil and gas industry to identify and assess potential hydrocarbon reservoirs and later monitor their exploitation, also have diverse applications in near-surface geophysics, mineral exploration, geothermal energy, and CO_2 or H_2 storage. Beyond revealing subsurface structures, these techniques enhance our understanding of how the subsurface responds to human activities, such as induced seismicity due to extraction processes. Seismic imaging and monitoring often focus on specific target layers within the subsurface, but challenges from interferences with surrounding layers and small changes within the specific layer(s) can distort the specific signals and lower the accuracy. Our research aims to address these challenges and provide practical solutions for more accurate and reliable seismic imaging and monitoring with reflected waves.

In this thesis, we aim to develop seismic data-driven methods for layer-specific imaging and monitoring, with a primary focus on advancing the technique of ghost-reflection retrieval using seismic interferometry (SI) and showing how the Marchenko method could be used with land seismic data.

SI often involves the cross-correlation of seismic observations at different receiver locations and the consecutive summation over the available sources, allowing the retrieval of new seismic responses from virtual sources located at the receiver positions. When using sources and receivers only at the surface, the virtual-source gathers retrieved by SI contain not only pseudo-physical reflections but also ghost (non-physical) reflections. These ghost reflections result mainly from the cross-correlation (CC) or auto-correlation (AC) of primary reflections from two different depths, representing reflections from inside specific subsurface layer(s), as measured with a virtual ghost source and a virtual ghost receiver positioned directly on top of the specific layer(s). Consequently, the ghost reflections can provide information about the specific layer(s) without the effects of the overburden and underburden layers.

We first explore the use of ghost reflections for layer-specific characterisation of the shallow subsurface using SI by AC, utilising numerically modelled data for a layered subsurface model down to 30 m depth, incorporating a lateral change in velocity, a velocity gradient with depth, a thickness change, and a velocity change in the target layer. Additionally, we present the first application of ghost reflections to shallow subsurface field data. Ghost reflections typically exhibit similar characteristics to other reflection events, appear close to or interfere with other events with only slight temporal differences. This makes their identification a significant challenge. To address this, we eliminate surface-related multiples and demonstrate how specific ghost reflections can be more efficiently retrieved by muting undesired reflections in the dataset before applying SI.

To extend the application of ghost reflections to deep structures, we focus on the feasibility of monitoring pore-pressure changes in the Groningen gas field in the Netherlands. We utilise numerical modelling to simulate scalar reflection data, deploying sources and

receivers at the surface. We conduct an ultrasonic transmission laboratory experiment to measure S-wave velocities at different pore pressures. This data is used to create subsurface models, which are then utilized to simulate scalar reflection seismic data for monitoring purposes. We retrieve zero-offset ghost reflections by applying SI by AC to the modelled datasets. We then use a correlation operator to determine time differences between a baseline survey and monitoring surveys. Additionally, we investigate the effects of the sources and receivers' geometry and spacing, as well as the number of virtual sources and receivers, on retrieving ghost reflections with high interpretability and resolution. Besides observing time shifts in the ghost reflections, we also explore the feasibility of using the amplitude of ghost reflections for reservoir monitoring.

Having clear reflections from both the top and bottom of the specific layer(s) is crucial for retrieving ghost reflections, which can be challenging when using land seismic datasets due to the usual presence of strong surface waves. Conventionally, surface waves are suppressed during data processing using frequency-offset, frequency-wavenumber, or bandpass filters. However, these approaches can prove ineffective when the surface waves are scattered and/or overlap with the frequency regions of the reflected body waves that we intend to preserve. To overcome some of these challenges, we show the efficacy of the interferometric surface-wave suppression using a 2D seismic reflection dataset from Scheemda, Groningen province, the Netherlands. Interferometric surface-wave suppression can be used to effectively suppress surface waves by applying SI to first estimate the surface waves and second followed by their adaptive subtraction from the original data. We propose to apply these two steps recursively, i.e., several times, which yields better results than a single application in terms of clearer and more continuous reflections. This technique can function as a standalone technique or as part of a pre-processing flow.

When applying the seismic reflection method for monitoring purposes, specific reflections, e.g., from the top and bottom of the reservoir, are of interest. The reflections from both the top and bottom of the specific layer(s) can also be distorted by other events from the surrounding layers. To eliminate such distortions, the Marchenko-redatuming method was introduced. Several Marchenko-redatuming methods have been applied successfully to marine field data. We demonstrate, for the first time, the application of the Marchenko-based isolation technique to field land seismic data to isolate the target response by removing the overburden and underburden. Land data are intrinsically elastic, known for dominant surface waves and a low signal-to-noise ratio, posing a challenge for the Marchenko method, which requires high-quality reflection data. After we carefully apply several pre-processing steps, including recursive interferometric surface-wave suppression, we apply the Marchenko method twice: first, to remove the overburden effects by choosing a focal depth of 30 m, and then to remove the underburden effects by choosing a focal depth of 270 m. This process generates a new reflection response from the target area, providing clearer subsurface responses. The Marchenko method is particularly beneficial for data-driven techniques such as ghost-reflection retrieval, seismic imaging, and time-lapse studies using land seismic datasets.

SAMENVATTING

Seismische beeldvorming en monitoring met gereflecteerde golven, oorspronkelijk gebruikt in de olie- en gasindustrie om potentiële koolwaterstofreservoirs te identificeren en te beoordelen en later de exploitatie ervan te controleren, hebben ook diverse toepassingen in de geofysica van de ondiepe ondergrond, de exploratie van mineralen, geothermische energie en de opslag van CO_2 of H_2. Deze technieken brengen niet alleen structuren in de ondergrond aan het licht, maar vergroten ook ons begrip van hoe de ondergrond reageert op menselijke activiteiten, zoals geïnduceerde aardbevingen door extractieprocessen. Seismische beeldvorming en monitoring richten zich vaak op specifieke doellagen in de ondergrond, maar interferentie met omliggende lagen en kleine veranderingen binnen de specifieke laag of lagen kunnen de specifieke signalen vervormen en de nauwkeurigheid verlagen. Ons onderzoek is erop gericht deze uitdagingen aan te pakken en praktische oplossingen te bieden voor nauwkeurigere en betrouwbaardere seismische beeldvorming en monitoring met reflecties.
In dit proefschrift willen we seismische data-gestuurde methoden ontwikkelen voor laagspecifieke beeldvorming en monitoring, met een primaire focus op het verbeteren van de techniek van het verkrijgen van spookreflecties met behulp van seismische interferometrie (SI) en het laten zien hoe de Marchenko methode gebruikt kan worden met seismische land-data.
Seismische interferometrie (SI) behelst de kruis-correlatie van seismische observaties op verschillende ontvanger locaties, gevolgd door een som over de beschikbare bronnen. Dit maakt het mogelijk om nieuwe seismische waarnemingen van virtuele bronnen op de plek van de ontvangers te creëren. Wanneer bronnen en ontvangers alleen aan het oppervlak worden gebruikt, bevatten de virtuele bronnen die door SI worden verkregen niet alleen pseudo-fysische reflecties, maar ook spookreflecties. Deze spookreflecties zijn voornamelijk het resultaat van de kruiscorrelatie (CC) of autocorrelatie (AC) van primaire reflecties van twee verschillende diepten, die interne reflecties vertegenwoordigen van specifieke ondergrondlaag of -lagen, zoals gemeten met een virtuele spookbron en een virtuele spookontvanger die direct boven de specifieke laag of lagen zijn geplaatst. Bijgevolg kunnen de spookreflecties informatie verschaffen over de specifieke laag of lagen zonder de effecten van de lagen boven en onder de specifieke laag of lagen.
Eerst verkennen we het gebruik van spookreflecties voor laagspecifieke karakterisering van de ondiepe ondergrond met SI door AC, waarbij we gebruikmaken van numeriek gemodelleerde data voor een gelaagd ondergrondmodel tot 30 m diepte, met een laterale snelheidsverandering, een snelheidsgradiënt met diepte, een dikteverandering en een snelheidsverandering in de doellaag. Daarnaast presenteren we de eerste toepassing van spookreflecties op veld-data van de ondiepe ondergrond. Spookreflecties vertonen meestal dezelfde kenmerken als fysische reflecties, verschijnen dichtbij of interfereren met andere reflecties, met slechts kleine temporele verschillen. Dit maakt hun identificatie een grote uitdaging. Om dit aan te pakken, elimineren we oppervlakte-gerelateerde

meervoudige reflecties en laten we zien hoe specifieke spookreflecties efficiënter kunnen worden gevonden door ongewenste reflecties in de dataset te onderdrukken voordat SI wordt toegepast.
Om de toepassing van spookreflecties uit te breiden naar diepe structuren, richten we ons op de haalbaarheid van het monitoren van veranderingen in de porie-druk in het Groningen-gasveld in Nederland. We gebruiken numerieke modellering om scalaire reflectie-data te simuleren, waarbij bronnen en ontvangers aan het oppervlak worden opgesteld. In het laboratorium voeren we een ultrasone transmissie meetmethode uit om S-golfsnelheden te meten bij verschillende porie-drukken. Deze gegevens worden gebruikt om ondergrondmodellen te maken, die vervolgens worden gebruikt om scalaire seismische reflectie-data te simuleren voor monitoringdoeleinden. We verkrijgen zero-offset spookreflecties door SI door AC toe te passen op de gemodelleerde datasets. Vervolgens gebruiken we een correlatieoperator om tijdsverschillen tussen een basis- en monitoringonderzoek te bepalen. Daarnaast onderzoeken we de effecten van de geometrie en de onderlinge afstand van de bronnen en ontvangers, evenals het aantal virtuele bronnen en ontvangers, op het verkrijgen van spookreflecties met een hoge interpreteerbaarheid en resolutie. Naast het waarnemen van tijdverschuivingen in de spookreflecties, onderzoeken we ook de haalbaarheid van het gebruik van de amplitude van spookreflecties voor reservoirmonitoring.
Duidelijke reflecties van zowel de boven- als de onderkant van de specifieke laag of lagen zijn cruciaal voor het verkrijgen van spookreflecties, wat een uitdaging kan zijn bij het gebruik van seismische land-datasets vanwege de gebruikelijke aanwezigheid van sterke oppervlaktegolven. Gewoonlijk worden oppervlaktegolven onderdrukt tijdens de dataverwerking met behulp van frequentie-golfgetal of bandfilters. Deze benaderingen kunnen echter ineffectief blijken wanneer de oppervlaktegolven worden verstrooid en/of overlappen met de frequentiegebieden van de gereflecteerde ruimtelijke golven die we willen behouden. Om enkele van deze uitdagingen te overwinnen, tonen we de doeltreffendheid van de interferometrische oppervlaktegolf-onderdrukkingsmethode met behulp van een 2D seismische reflectiedataset uit Scheemda, provincie Groningen, Nederland. De interferometrische oppervlaktegolf-onderdrukkingsmethode kan worden gebruikt om effectief oppervlaktegolven te onderdrukken. Dit gebeurt door SI toe te passen om eerst de oppervlaktegolven te schatten en vervolgens deze adaptief van de originele data af te trekken. We stellen voor om deze twee stappen recursief toe te passen, dat wil zeggen meerdere keren, wat betere resultaten oplevert dan een enkele toepassing, met duidelijkere en meer continue reflecties. Deze techniek kan op zichzelf staan of deel uitmaken van een voorbewerkingsproces.
Bij het toepassen van de seismische reflectiemethode voor monitoringdoeleinden zijn specifieke reflecties, bijvoorbeeld van de boven- en onderkant van het reservoir, van belang. De reflecties van zowel de boven- als de onderkant van de specifieke laag of lagen kunnen ook worden vervormd door andere reflecties in de omringende lagen. Om dergelijke vervormingen te elimineren, werd de Marchenko-methode geïntroduceerd. De Marchenko-methode is reeds met succes toegepast op mariene veld-data. Wij demonstreren voor het eerst de toepassing van een op de Marchenko-methode gebaseerde isolatie op seismische land-data om de doelrespons te isoleren door de boven- en onderlagen te verwijderen. Land-data zijn intrinsiek elastisch, staan bekend om dominante

oppervlaktegolven en een lage signaal-ruisverhouding, wat een uitdaging vormt voor de Marchenko-methode, die reflectie-data van hoge kwaliteit vereist. Nadat we zorgvuldig verschillende voorbewerkingsstappen hebben toegepast, waaronder recursieve interferometrische onderdrukking van oppervlaktegolven, passen we de Marchenko-methode twee keer toe: eerst om de bovenliggende lagen te verwijderen door een focale diepte van 30 m te kiezen, en vervolgens om de onderliggende lagen te verwijderen door een focale diepte van 270 m te kiezen. De Marchenko-methode is vooral nuttig voor data-gedreven technieken zoals het verkrijgen van spookreflecties, seismische beeldvorming en tijdsafhankelijke onderzoeken met seismische land-datasets.

1

INTRODUCTION

Seismic imaging with reflected waves is a geophysical method used to create images of the Earth's subsurface at various scales, utilising seismic waves generated by either active or passive sources (e.g., Yilmaz, 2001). This technique facilitates the obtaining of detailed images of subsurface structures and can also be used to monitor the properties of the subsurface. The primary application of seismic imaging and monitoring with reflected waves is still within the oil and gas industry, as it plays a pivotal role in identifying and assessing potential hydrocarbon reservoirs. However, the use of seismic imaging and monitoring finds diverse applications in fields such as near-surface geophysics, mineral exploration, geothermal energy resources, and CO_2 or H_2 storage.

Beyond providing information about the features and structures of the subsurface, seismic imaging and monitoring play a crucial role in enhancing the understanding of how the subsurface responds to various human activities. For example, the extraction process could induce seismic events; therefore, understanding and investigating the changes inside a reservoir is essential for ensuring the safety and sustainability of such extraction operations. Moreover, seismic imaging and monitoring can be used to optimise resource-development strategies, particularly for sustainable energy sources such as geothermal energy, by analysing subsurface structures (Salaun et al., 2020). This enables more efficient and sustainable utilisation of geothermal energy resources while mitigating geological hazards. Additionally, seismic imaging and monitoring are invaluable in the context of carbon capture and storage (CCS) projects, where CO_2 captured from industrial processes or separated from the air is injected deep underground for long-term storage in geological formations, such as depleted oil and gas reservoirs or saline aquifers, or permanent storage in basalts. Seismic monitoring plays a crucial role in assessing the integrity of reservoir storage sites, ensuring the containment of the injected CO_2 and mitigating the risk of leakage or induced seismicity (Lumley, 2010).

Overall, seismic imaging and monitoring are indispensable tools in our efforts to understand and manage the potential of the shallow and deep subsurface for various human endeavours, such as energy transition. We often focus on specific target layers within the subsurface in many seismic imaging and monitoring applications, like

those for geothermal energy extraction (Barbier, 2002) or CO_2 (Wang et al., 2022) and H_2 storage (Kumar et al., 2022). These target layers may be characterised by their unique geological properties, such as rock type, porosity, or fluid content. However, the challenges associated with seismic imaging and monitoring these target layers can be substantial. One common issue is the presence of overlying layers, known as overburden, which can distort seismic signals and hinder the accurate imaging of the specific layer beneath (Calvert, 2005). Additionally, even within the specific layer itself, small changes in geological properties or fluid content may affect the reliability of seismic-data interpretation.

To address these challenges, we aim to develop seismic layer-specific imaging and monitoring techniques. To provide this tool, we develop a technique for ghost (non-physical) reflection retrieval using seismic interferometry (SI). We investigate the retrieval of ghost reflections in shallow and deep structures using land seismic datasets, focusing on retrieving ghost reflections from primary reflections. When applying the technique to land data, it is challenging to use reflections due to the stronger wave attenuation, lower signal-to-noise ratio, and presence other, undesired events, like surface waves, that mask the reflections. Therefore, we employ two data-driven approaches to enhance the resolution of primary reflections in land seismic data. First, we develop a technique for surface-wave suppression using SI. Second, we utilise the Marchenko-based isolation to remove the effects of the overburden and underburden. Both techniques help enhance the resolution of reflections, which is essential for data-driven techniques such as ghost-reflection retrieval using SI.

In the next section, we briefly explain SI and the Marchenko method. Finally, this chapter concludes with a description of the outline of this thesis.

1.1. SEISMIC INTERFEROMETRY

SI most often refers to the principle of retrieving new seismic responses from virtual sources located at the position of receivers by using the responses of two receivers (Lobkis and Weaver, 2001; Wapenaar and Fokkema, 2006; Curtis et al., 2006; Snieder et al., 2007; Draganov et al., 2007; Schuster, 2009; Wapenaar et al., 2010). This virtual-source response can be retrieved using correlation, coherence, convolution, or deconvolution of the seismic responses (e.g., Slob et al., 2007; Nakata et al., 2011; Wapenaar et al., 2011). For example, in Figure 1.1a, SI by cross-correlation applied to observations at two receivers at X_A and X_B (blue triangles) retrieves a signal from a virtual source located at the exact location as one of the receiver (X_A) as recorded at the location of the other receiver (X_B), effectively removing the common travel path from X_S to X_A where the seismic signal was emitted by the source at X_S (red circles). The cross-correlated results must be summed over all the surrounding sources to retrieve the complete response between the two receivers. The sources, such as X_S, that provide travel paths successively passing through X_A and X_B are at stationary-phase region (Snieder, 2004). Having the contributions from only the stationary-phase region would be sufficient to retrieve an estimate of the response between two receivers as the other sources contribute destructively to each other (Wapenaar, 2004; Snieder et al., 2006).

SI requires that the source surface surrounds the two receivers completely. When part of this boundary is a free surface, like the Earth's surface, then only sources in the

subsurface (red circles in Figure 1.1b) are required because the free surface effectively serves as a mirror and, through reflection, turns the half-sphere into a full sphere. In seismic exploration, the employed sources are not in the subsurface but at the surface, as illustrated by white-filled circles in Figure 1.1b. Nevertheless, the wavefields generated by surface sources contain ray paths between positions X_A and X_B that coincide with those of wavefields generated by subsurface sources (red circles in Figure 1.1b). Consequently, equivalent surface sources (white-filled circles) can be identified for all subsurface sources (Halliday and Curtis, 2008). By using sources and receivers at the surface, the so-called one-sided illumination of the receivers occurs (Wapenaar, 2006). A consequence of the one-sided illumination is that the application of SI retrieves not only the desired physical reflections but also ghost (non-physical) arrivals (Draganov et al., 2012; King et al., 2011).

The retrieved physical events include direct body waves, reflections, and refractions, but also scattered, diving, and surface waves. For instance, to retrieve the desired physical reflections, one needs to correlate, e.g., the primary reflection at X_A (the blue arrow in Figure 1.1b) with its first free-surface multiple (the dotted blue arrow in Figure 1.1b). The correlation process effectively eliminates the common ray path and facilitates the retrieval of the reflection at X_B due to a virtual source at X_A, which is shown by the brown arrow in Figure 1.1c. However, as a consequence of using sources at the surface, the amplitude and phase of this retrieved reflection are not correct, and we refer to it as a pseudo-physical reflection (Löer et al., 2013; Boullenger and Draganov, 2016). If the recorded traces at the two receivers also contain surface waves, the retrieved result by cross-correlation would also contain surface waves between these receivers as shown by the purple arrow in Figure 1.1c.

In addition to pseudo-physical reflections, one-sided illumination of sources leads to retrieval of ghost (non-physical) reflections, as shown by the orange arrow in Figure 1.1c. Ghost reflections result from the correlation of two primary reflections or internal multiples. In this example, it is the result of the cross-correlation of the primary reflections from the top and bottom of the second layer (the blue and green arrows in Figure 1.1b, respectively). The ghost reflections could provide valuable information about the physical rock properties of the subsurface, such as velocity or thickness changes because they represent reflections from inside specific subsurface layers - as they would be measured with a virtual ghost source and a virtual ghost receiver positioned directly on top of the specific layers, which means ghost reflections only propagate inside the specific layer. Consequently, the ghost reflections can provide information on a specific layer without the kinematic effect of changes in the overburden and underburden layers (Draganov et al., 2012).

In this thesis, we investigate the application of SI for retrieving ghost reflections, which can be used for layer-specific imaging and monitoring and for retrieving surface waves in the context of surface-wave suppression.

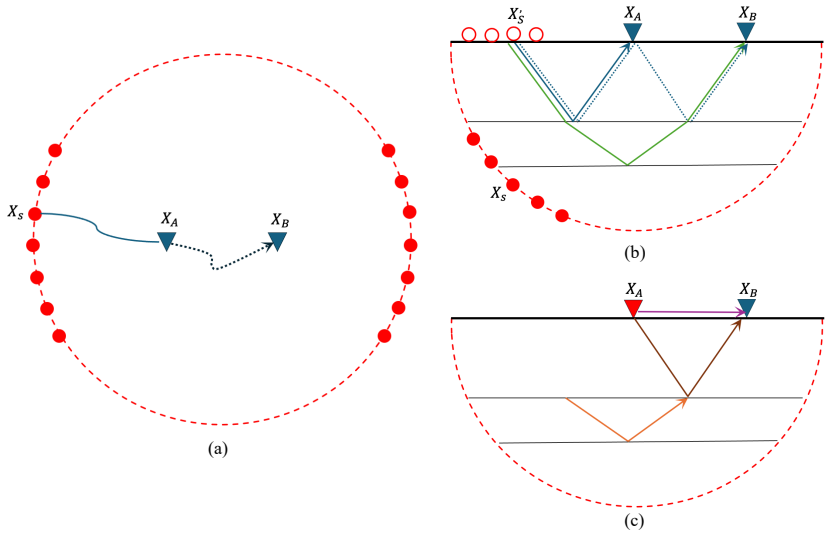

Figure 1.1: (a) Theoretical configuration for seismic interferometry (SI) between two receivers X_A and X_B (blue triangles) in an inhomogeneous medium. Retrieving the response between these two receivers requires the summation of the cross-correlated signals over a boundary of sources (red circles) enclosing the receivers. (b) Configuration for the sources and receives at the earth's free surface: retrieving reflections requires the recordings from a subsurface boundary of sources. The contribution of the subsurface source X_S (red circles) to the reflected wave path can also be kinematically achieved with a source at the surface (white-filled circles). The blue arrow shows the primary reflection from the first layer, the dotted blue arrow shows its surface-related multiple, and the green arrow shows the reflection from the bottom of the second layer. (c) The result of the application of SI using the configuration is shown in (b), where the receiver at X_A acts as a virtual source (red triangle). The orange arrow shows the ghost reflection from inside the second layer, the brown arrow shows the pseudo-physical reflection, and the purple arrow shows the surface waves.

1.2. THE MARCHENKO METHOD

The Marchenko method enables the creation of virtual sources or receivers in the subsurface at arbitrary depth positions, requiring only reflection data and a smooth macro-velocity model (Broggini et al., 2012; Slob et al., 2014; Wapenaar et al., 2014). I.e., the Marchenko method retrieves the Green's function from a virtual source in the subsurface, where no physical receivers were present, to receivers at the surface. By introducing initial focusing functions in a truncated medium similar to the actual medium, the Marchenko equations can be solved, allowing for the retrieval of Green's function representing upgoing and downgoing one-way wavefields.

Once the upgoing and downgoing Green's functions are retrieved at subsurface points, the complete influence above those points can be eliminated by retrieving a redatumed response for virtual sources and receivers at those points. This can be obtained either by applying SI by multidimensional deconvolution (MDD) to the upgoing and downgoing Green's functions retrieved through the Marchenko method (Broggini et al., 2014; Ravasi et al., 2016) or by using a double focusing function (van der Neut et al., 2015; Staring et al., 2018) on the retrieved Green's functions. Consequently, an image of the subsur-

face can be produced from the redatumed data, free from artefacts caused by internal multiples from the overburden above the redatumed level.

To reduce the sensitivity of the Marchenko method to the macro-velocity model, it was suggested that the virtual sources and receivers be extrapolated upward to the acquisition surface (Meles et al., 2016; van der Neut and Wapenaar, 2016). This class of Marchenko methods focuses on eliminating internal multiples from reflection data while keeping the sources and receivers at the surface. In this thesis, we use such extrapolated Green's functions and focusing functions to remove the effects of the overburden and underburden. A complete overview of the Marchenko redatuming, imaging, and multiple elimination can be found in Wapenaar et al. (2021).

1.3. AIM AND OUTLINE OF THE THESIS

This thesis focuses on developing seismic data-driven methods for layer-specific imaging and monitoring applicable to various scenarios, such as imaging and monitoring the shallow and deep subsurface. Our primary focus is on developing the technique of ghost-reflection retrieval using SI. We demonstrate the application of this technique through numerical modelling of both shallow-subsurface and deep structures, as well as field datasets. Retrieving ghost reflections requires primary reflections, making retrieval of ghost reflections from land seismic datasets challenging. To address this, we also develop a technique based on SI for surface-wave suppression and utilise the Marchenko-based isolation technique to remove the interference from the overburden and underburden. The outline of this thesis is as follows:

Chapter 2: Shallow-subsurface characterisation using ghost reflections.
In this chapter, we demonstrate the potential of ghost reflection retrieval from SI for layer-specific characterisation of the shallow subsurface. To achieve this, we use synthetic data for a subsurface model down to 30 meters depth, incorporating a lateral change in velocity, a velocity gradient with depth, a thickness change, and a velocity change in the target layer. We then apply the technique to shallow subsurface field data. Additionally, we focus on improving the retrieval of ghost reflections by removing free-surface multiples and muting undesired events in active-source gathers before applying SI.

Chapter 3: Reservoir monitoring using ghost reflections.
In this chapter, we extend the approach of ghost-reflection retrieval for deeper structures. This chapter has several distinct sections. First, we focus on the feasibility of monitoring small changes in the Groningen gas field in the Netherlands, a well-known example of induced seismicity due to gas extraction. We perform an ultrasonic transmission laboratory experiment to build a realistic subsurface model to measure pore-pressure changes. Second, we determine time differences between baseline and monitoring surveys using a correlation operator. We also discuss how it is possible to enhance the sensitivity of detecting small changes by interpolating ghost reflections. Finally, we investigate the effect of the sources and receivers' geometry and spacing and the number of virtual sources and receivers on retrieving ghost reflections with high interpretability and resolution.

Chapter 4: Investigating the amplitude of ghost reflections.
In this chapter, we focus on another crucial aspect of ghost reflection for layer-specific monitoring – its amplitude. Using numerically modelled data for the Groningen subsurface, we demonstrate the potential of utilising the amplitude of ghost reflections to track small changes within the reservoir. We employ various methods, including SI by autocorrelation (AC) using muted common-source gathers, SI by AC using separated reflections, SI by AC using normalised separated reflections, and trace deconvolution. These approaches increase our chances of accurately investigating the amplitude of ghost reflections.

Chapter 5: Recursive interferometric surface-wave suppression.
In Chapters 2 and 3, we show that clear reflections from both the top and bottom of the specific target layer are required for retrieving ghost reflections. The reflections from the top and the bottom could be masked by surface waves. In this chapter, we show the effectiveness of SI for surface-wave suppression in an active-source reflection seismic dataset acquired in Scheemda, Groningen province, the Netherlands. We obtain a dominant surface wave at each virtual-source position by applying SI. Subsequently, we employ adaptive subtraction of the retrieved surface waves from the active-source data to suppress the surface waves in a recursive mode. The results are promising, as this process not only aids enhancing the clarity of reflections for retrieving ghost reflections in the active-source data, but it can also be used as a new data-driven technique for surface-wave suppression in land seismic datasets.

Chapter 6: Application of Marchenko-based isolation to a land seismic dataset
Following the very effective recursive interferometric suppression of surface waves in Chapter 5, which is important for successful application of Marchenko redatuming, this chapter focuses on employing the Marchenko-based isolation to eliminate the interference from the overburden and underburden by using the field dataset from Chapter 5. Our approach involves a two-step strategy: first, removing the overburden, followed by removing the underburden. This process generates a new reflection response from the target area. As a result, this method is particularly effective for obtaining clear subsurface responses, making it advantageous for data-driven methods such as ghost-reflection retrieval, seismic imaging, or time-lapse studies using land seismic datasets.

Chapter 7: Conclusions and future outlook
The final chapter summarises the results and provides general conclusions about the research presented in this thesis. Additionally, recommendations for future research are made, which can help further develop the ideas and techniques proposed in this thesis.

REFERENCES

Barbier, E. (2002). Geothermal energy technology and current status: An overview. *Renewable and Sustainable Energy Reviews*, *6*, 3–65. https://doi.org/10.1016/S1364-0321(02)00002-3

Boullenger, B., & Draganov, D. (2016). Interferometric identification of surface-related multiples. *Geophysics*, *81*(6), Q41–Q52. https://doi.org/10.1190/GEO2015-0450.1

Broggini, F., Snieder, R., & Wapenaar, K. (2012). Focusing the wavefield inside an unknown 1d medium: Beyond seismic interferometry. *Geophysics*, *77*, A25–A28. https://doi.org/10.1190/geo2012-0060.1

Broggini, F., Snieder, R., & Wapenaar, K. (2014). Data-driven wavefield focusing and imaging with multidimensional deconvolution: Numerical examples for reflection data with internal multiples. *Geophysics*, *79*, WA107–WA115. https://doi.org/10.1190/GEO2013-0307.1

Calvert, R. (2005). 4d technology: Where are we, and where are we going? *Geophysical Prospecting*, *53*, 161–171. https://doi.org/10.1111/j.1365-2478.2004.00469.x

Curtis, A., Gerstoft, P., Sato, H., Snieder, R., & Wapenaar, K. (2006). Seismic interferometry—turning noise into signal. *The Leading Edge*, *25*, 1082–1092. https://doi.org/10.1190/1.2349814

Draganov, D., Heller, K., & Ghose, R. (2012). Monitoring CO2 storage using ghost reflections retrieved from seismic interferometry. *International Journal of Greenhouse Gas Control*, *11*(SUPPL), S35–S46. https://doi.org/10.1016/j.ijggc.2012.07.026

Draganov, D., Wapenaar, K., Mulder, W., Singer, J., & Verdel, A. (2007). Retrieval of reflections from seismic background-noise measurements. *Geophysical Research Letters*, *34*, 1–4. https://doi.org/10.1029/2006GL028735

Halliday, D., & Curtis, A. (2008). Seismic interferometry, surface waves and source distribution. *Geophysical Journal International*, *175*, 1067–1087. https://doi.org/10.1111/j.1365-246X.2008.03918.x

King, S., Curtis, A., & Poole, T. L. (2011). Interferometric velocity analysis using physical and nonphysical energy. *Geophysics*, *76*(1), SA35–SA49. https://doi.org/10.1190/1.3521291

Kumar, K. R., Honorio, H. T., & Hajibeygi, H. (2022). Simulation of the inelastic deformation of porous reservoirs under cyclic loading relevant for underground hydrogen storage. *Scientific Reports*, *12*, 1–23. https://doi.org/10.1038/s41598-022-25715-z

Lobkis, O. I., & Weaver, R. L. (2001). On the emergence of the green's function in the correlations of a diffuse field. *The Journal of the Acoustical Society of America*, *110*, 3011–3017. https://doi.org/10.1121/1.1417528

Löer, K., Meles, G. A., Curtis, A., & Vasconcelos, I. (2013). Diffracted and pseudo-physical waves from spatially limited arrays using source-receiver interferometry (SRI). *Geophysical Journal International*, *196*(2), 1043–1059. https://doi.org/10.1093/gji/ggt435

Lumley, D. (2010). 4d seismic monitoring of CO2 sequestration. *The Leading Edge*, *29*, 150–155. https://doi.org/10.1190/1.3304817

Meles, G. A., Wapenaar, K., & Curtis, A. (2016). Reconstructing the primary reflections in seismic data by Marchenko redatuming and convolutional interferometry. *Geophysics*, *81(2)*, Q15–Q26. https://doi.org/10.1190/geo2015-0377.1

Nakata, N., Snieder, R., Tsuji, T., Larner, K., & Matsuoka, T. (2011). Shear wave imaging from traffic noise using seismic interferometry by cross-coherence. *Geophysics*, *76*, SA97–SA106. https://doi.org/10.1190/geo2010-0188.1

Ravasi, M., Vasconcelos, I., Kritski, A., Curtis, A., Filho, C. A. d. C., & Meles, G. A. (2016). Target-oriented Marchenko imaging of a North Sea field. *Geophysical Journal International*, *205*(1), 99–104. https://doi.org/10.1093/gji/ggv528

Salaun, N., Toubiana, H., Mitschler, J.-B., Gigou, G., Carriere, X., Maurer, V., & Richard, A. (2020). High-resolution 3d seismic imaging and refined velocity model building improve the image of a deep geothermal reservoir in the upper rhine graben. *The Leading Edge*, *39*, 857–863. https://doi.org/10.1190/tle39120857.1

Schuster, G. T. (2009). *Seismic Interferometry*. Cambridge University Press. https://doi.org/10.1017/CBO9780511581557

Slob, E., Draganov, D., & Wapenaar, K. (2007). Interferometric electromagnetic green's functions representations using propagation invariants. *Geophysical Journal International*, *169*, 60–80. https://doi.org/10.1111/j.1365-246X.2006.03296.x

Slob, E., Wapenaar, K., Broggini, F., & Snieder, R. (2014). Seismic reflector imaging using internal multiples with Marchenko-type equations. *Geophysics*, *79*(2), S63–S76. https://doi.org/10.1190/GEO2013-0095.1

Snieder, R. (2004). Extracting the green's function from the correlation of coda waves: A derivation based on stationary phase. *Physical Review E*, *69*, 046610. https://doi.org/10.1103/PhysRevE.69.046610

Snieder, R., Wapenaar, K., & Larner, K. (2006). Spurious multiples in seismic interferometry of primaries. *Geophysics*, *71*(4), SI111–SI124. https://doi.org/10.1190/1.2211507

Snieder, R., Wapenaar, K., & Wegler, U. (2007). Unified green's function retrieval by cross-correlation; connection with energy principles. *Physical Review E*, *75*, 036103. https://doi.org/10.1103/PhysRevE.75.036103

Staring, M., Pereira, R., Douma, H., van der Neut, J., & Wapenaar, K. (2018). Source-receiver Marchenko redatuming on field data using an adaptive double-focusing method. *Geophysics*, *83*(6), S579–S590. https://doi.org/10.1190/geo2017-0796.1

van der Neut, J., Thorbecke, J., Wapenaar, k., & Slob, E. (2015). Inversion of the multi-dimensional Marchenko equation. *77th EAGE Conference and Exhibition 2015: Earth Science for Energy and Environment*, 1–5. https://doi.org/10.3997/2214-4609.201412939

van der Neut, J., & Wapenaar, K. (2016). Adaptive overburden elimination with the multidimensional Marchenko equation. *Geophysics*, *81*(5), T265–T284. https://doi.org/10.1190/GEO2016-0024.1

Wang, Y., Vuik, C., & Hajibeygi, H. (2022). Analysis of hydrodynamic trapping interactions during full-cycle injection and migration of CO2 in deep saline aquifers. *Advances in Water Resources*, *159*, 104073. https://doi.org/10.1016/j.advwatres.2021.104073

Wapenaar, K. (2004). Retrieving the elastodynamic green's function of an arbitrary inhomogeneous medium by cross correlation. *Physical Review Letters*, *93*, 254301. https://doi.org/10.1103/PhysRevLett.93.254301

Wapenaar, K. (2006). Green's function retrieval by cross-correlation in case of one-sided illumination. *Geophysical Research Letters*, *33*(19), L19304. https://doi.org/10.1029/2006GL027747

Wapenaar, K., Brackenhoff, J., Dukalski, M., Meles, G., Reinicke, C., Slob, E., Staring, M., Thorbecke, J., van der Neut, J., & Zhang, L. (2021). Marchenko redatuming, imaging, and multiple elimination and their mutual relations. *Geophysics*, *86*(5), WC117–WC140. https://doi.org/10.1190/geo2020-0854.1

Wapenaar, K., Draganov, D., Snieder, R., Campman, X., & Verdel, A. (2010). Tutorial on seismic interferometry: Part 1 — basic principles and applications. *Geophysics*, *75*, 75A195–75A209. https://doi.org/10.1190/1.3457445

Wapenaar, K., & Fokkema, J. (2006). Green's function representations for seismic interferometry. *Geophysics*, *71*(4), SI33–SI46. https://doi.org/10.1190/1.2213955

Wapenaar, K., Thorbecke, J., van der Neut, J., Broggini, F., Slob, E., & Snieder, R. (2014). Marchenko imaging. *Geophysics*, *79*(3), WA39–WA57. https://doi.org/10.1190/GEO2013-0302.1

Wapenaar, K., van der Neut, J., Ruigrok, E., Draganov, D., Hunziker, J., Slob, E., Thorbecke, J., & Snieder, R. (2011). Seismic interferometry by crosscorrelation and by multidimensional deconvolution: A systematic comparison. *Geophysical Journal International*, *185*, 1335–1364. https://doi.org/10.1111/j.1365-246X.2011.05007.x

Yilmaz, Ö. (2001). *Seismic data analysis*. Society of Exploration Geophysicists. https://doi.org/10.1190/1.9781560801580

2

LAYER-SPECIFIC CHARACTERISATION OF THE SHALLOW SUBSURFACE USING GHOST REFLECTIONS

Seismic interferometry (SI) retrieves the Green's function between two receiver locations using their recordings from a boundary of sources. When using sources and receivers only at the surface, the virtual-source gathers retrieved by SI contain pseudo-physical reflections as well as ghost (non-physical) reflections. These ghost reflections are the results of the cross-correlation or auto-correlation (AC) of primary reflections from two different depth levels, and they contain information about the seismic properties of specific layers in the subsurface. We investigate the application of ghost reflections for layer-specific characterisation of the shallow subsurface using SI by AC. First, we show the technique's potential using synthetic data for a subsurface model with a lateral change in velocity, a gradient in depth for velocity, a thickness change, and a velocity change of the target layer. Then, we apply the technique to shallow subsurface field data. We also focus on improving the retrieval of ghost reflections by removing the free-surface multiples and muting undesired events in active-source gathers before applying SI. Our results demonstrate that the ghost reflections can be used advantageously to characterise the layer that causes them to appear in the results of SI. Consequently, they can also provide valuable information for imaging and monitoring shallow subsurface structures.

This Chapter was published as Shirmohammadi, F., Draganov, D., & Ghose, R. (2024) The utilisation of ghost reflections retrieved by seismic interferometry for layer-specific characterisation of the shallow subsurface. *Near Surface Geophysics*, *22*, 92–105. https://doi.org/10.1002/nsg.12275
Minor modifications have been applied to keep consistency within the thesis.

2.1. INTRODUCTION

Seismic interferometry (SI) is a method for estimating the Green's function between different receivers using correlation, convolution, or deconvolution of the recordings from surrounding sources by turning the receivers into virtual sources (Wapenaar and Fokkema, 2006; Snieder et al., 2009). In the case of using correlation, the Green's function between two receivers is retrieved by cross-correlating recorded responses generated by each source and then summing the correlation results over the surrounding sources. Moreover, Curtis et al. (2009) showed that it is possible to estimate the Green's function between two sources surrounded by a boundary of receivers where one source acts as a virtual receiver.

The theory behind SI assumes certain conditions. Among others, it is assumed that there are no intrinsic losses in the medium, although, in reality, the Earth is strongly attenuating. Additionally, the receivers are presumed to be evenly surrounded by a complete and sufficiently dense boundary of either passive or active sources. In practice, these assumptions are rarely met, particularly when applied to surface exploration data (i.e., sources and receivers located at or near the surface). As a result, not only the pseudo-physical reflections are retrieved, but also the ghost (non-physical) reflections (Snieder et al., 2009, Draganov et al., 2010, King et al., 2011). The pseudo-physical reflections and lower-order multiples are retrieved through the correlation of primary reflections with their surface-related multiples or a multiple with its next-order multiple (Löer et al., 2013, and Boullenger and Draganov, 2016). In contrast, ghost reflections are caused by the correlation of primary reflections from two different depth levels (Draganov et al., 2012, King and Curtis, 2012).

The ghost reflections could provide valuable information about the physical rock properties of the subsurface, such as velocity or thickness changes, because they represent reflections from inside specific subsurface layers - as measured with a virtual ghost source and a virtual ghost receiver positioned directly on top of the specific layers, which means ghost reflections only propagate inside the specific layer (Draganov et al., 2013). Consequently, the ghost reflections can provide information of a specific layer without the effect of changes in overburden and underburden layers. Through realistic numerical modelling using a horizontally layered model, Draganov et al. (2012) showed that ghost reflections are sensitive only to the thickness and velocity of the target layers. Ma et al. (2021, 2022) illustrated the application of ghost reflections in estimating the layer-specific velocity of a fluid-mud layer in a water/fluid-mud system, using ultrasonic experiments. They clearly showed that the retrieved ghost reflections propagate only inside the fluid-mud layer, and the travel paths inside the water layer are eliminated. Also, Draganov et al. (2013) applied SI to records from receivers at the Earth's surface from sources in wells. They showed, using a horizontal well, that the identified ghost reflections could be employed to monitor the changes in velocity and quality-factor inside a layer at a depth of 600 m.

In this study, we use numerical modelling and field data to investigate the utilisation of ghost reflections retrieved by SI for monitoring and imaging purposes, particularly in shallow subsurface applications. Few studies have investigated the application of ghost arrivals from SI in shallow subsurface studies, especially using field data. Harmankaya et al. (2013) showed the application of ghost arrivals in locating near-surface scatters. To

do that, they inverted the travel time of ghost arrivals by solving the inverse problem for several numerically modelled datasets with increasing complexity by including lateral inhomogeneity, and they demonstrated that the location of the scatterer can be estimated with good accuracy from ghost scattered waves. Moreover, Nichols et al. (2010) presented the first application of ghost refractions (the so-called virtual refractions) to field data for near-surface characterisation. They determined seismic velocities of unsaturated and saturated sand layers, and the relative variable depth by combining information from the virtual shot record, the correlation gather, and the actual field shot record.

In this Chapter, we first illustrate the potential of ghost reflections using numerically modelled data for a layered subsurface model in different conditions, including a lateral change in velocity, a gradient change in velocity, and a thickness change. We retrieve virtual zero-offset sections using SI by auto-correlation (AC). Studies on retrieving ghost reflections have been mostly restricted to using cross-correlation (CC) in SI. However, the SI by AC can provide extra information on the subsurface in imaging and monitoring, because the result of SI by AC is directly a zero-offset section obtained without any other seismic processing. Additionally, we present the first application of ghost reflections to shallow subsurface field data. The site is located near Rotterdam, the Netherlands. The geology of this site, known from earlier borehole measurements, comprises flat alternating Holocene clay and sand layers (Ghose and Goudswaard, 2004). We retrieve zero-offset sections by turning shots into virtual receivers, and receivers into virtual sources. In both cases, we investigate the trend of ghost reflections for directly imaging and monitoring the target layer.

Ghost reflections usually exhibit similar characteristics to other reflection events, appearing in close proximity to each other with only slight temporal differences. So, one of the most significant challenges in using ghost reflections is their identification. Draganov et al. (2010) showed that ghost reflections could be identified by a change of their polarity after the application of a damping-compensation factor. Curtis and Halliday (2010) showed that ghost arrivals could be identified either through wavefield separation or by reversing the order of the CC in perturbed acoustic media. Draganov et al. (2013) proposed using a vertical-well geometry to identify ghost reflections. Ruigrok et al. (2009) showed that the identification could be achieved by applying both SI by CC with full responses and SI by CC between a full response and only the first arrival at the other receiver.

Here, to address the challenge of identification of the ghost reflections, we eliminate the surface-related multiples in the synthetic dataset, which could be achieved through using an absorbing boundary condition at the surface in the numerical modelling. As a result, the retrieved events include only the ghost reflections. Furthermore, we show how the specific ghost reflections can be retrieved more efficiently by muting undesired reflections in the dataset before applying SI. Using the muted active-source gathers also helps retrieve robust and clear ghost reflections from the field data.

Below, we first present a brief overview of the methodology of retrieving ghost reflections with SI in section 2.2. Then, in section 2.3.1, we show the results of SI by AC when applied to data from numerical modelling for several subsurface models. There, we discuss how to retrieve the ghost reflections more efficiently. After that, we illustrate

in section 2.3.2 the application of this technique to a field dataset. This is followed by discussion and conclusions.

2.2. METHOD

Through reciprocity theorems of the correlation type, Wapenaar and Fokkema (2006) showed that the acoustic Green's function $\hat{G}(x_B, x_A, \omega)$ between two points at x_A and x_B can be obtained from

$$\hat{G}^*(x_B, x_A, \omega) + \hat{G}(x_B, x_A, \omega) \approx \frac{2}{\rho c} \int_{\partial D} \hat{G}^*(x_A, x, \omega) \hat{G}(x_B, x, \omega)\, d^2x, \tag{2.1}$$

where c and ρ are the constant propagation velocity and mass density, respectively, at and outside of the source-boundary surface ∂D, which effectively encloses x_A and x_B. The asterisk $(*)$ denotes complex conjugation in the frequency domain, which corresponds to a time-reversed version of a quantity in the time domain. To derive relation 2.1 from the exact relation of seismic interferometry (equation 19 from Wapenaar and Fokkema, 2006) the following assumptions and approximations are made:

- A high-frequency approximation is used to reduce the original double integral to the above single integral by representing normal derivatives as a term involving the cosine of the angle between the pertinent ray and the normal on ∂D;
- The medium at and outside D is homogeneous, which eliminates a term that would otherwise result in the retrieval of certain types of ghost events due to the correlation of fields emitted by the sources toward inside and outside ∂D.
- ∂D is a sphere with a large radius, which reduces the correlation between dipole sources and monopole sources to only the correlation between monopole sources.

The right-hand side of relation 2.1 represents the CC of recordings at points x_A and x_B from sources at positions x and on ∂D in the subsurface. When the sources surround the two receivers, physical reflections (the black arrows in Figure 2.1a) are retrieved from the correlation of direct arrivals (the dotted blue line in Figure 2.1a) with their corresponding surface-related multiples (the dotted green line in Figure 2.1a), where one receiver acts as a virtual source (as indicated by a yellow star in Figure 2.1a). Here, the free surface acts as a mirror, meaning, through reflection, it turns the half-sphere of sources into a full sphere. As a result, there is a complete surface of sources that surround the receivers, and only physical reflections are retrieved. The above might result in amplitude errors. However, the phases are correct (Wapenaar and Fokkema, 2006).

In exploration seismology, where the sources are usually restricted to the surface (such as the red dots in Figure 2.1b), we can consider a stationary point on ∂D is equivalent to a stationary point at the surface by using simple geometric arguments (Halliday et al., 2007 and Draganov et al., 2012) and applying the stationary-phase method (Snieder et al., 2006). As a result, we can replace the integration over ∂D in relation 2.1 by a summation over N active sources at the surface (Halliday et al., 2007):

$$\hat{G}^*(x_B, x_A, \omega) + \hat{G}(x_B, x_A, \omega) \propto \sum_{n=1}^{N} \hat{G}^*(x_A, x_n, \omega) \hat{G}(x_B, x_n, \omega). \tag{2.2}$$

The right-hand side of this relation is, in the time domain, a CC between two observations at positions x_A and x_B, both originating from active sources located at x_n at the surface (such as the red dots in Figure 2.1b). The retrieved Green's function in the left-hand side of relation 2.2 comprises pseudo-physical reflections, as well as ghost reflections. These ghost reflections are retrieved in the time domain from the CC of primary reflections from two different interfaces due to insufficient destructive interferences (Draganov et al., 2012, Ma et al., 2022).

Ghost reflections are similarly retrieved from correlation of internal multiples with primaries or other internal multiples. For example, the result of CC of the primary reflection from the second interface recorded at x_B (the orange arrows in Figure 2.1b) with the primary reflection from the first interface (the blue arrows in Figure 2.1b) retrieves a ghost reflection which propagates only inside the second layer (the cyan arrows in Figure 2.1b). The retrieved ghost reflection can be intuitively interpreted as the wavefield reflected from the second interface as a ghost virtual source (the red star in Figure 2.1b) and a ghost virtual receiver (the white triangle in Figure 2.1b) are positioned at the first interface. We labelled them as a ghost virtual source or a ghost virtual receiver because they cannot be physically placed there. Note that the retrieved pseudo-physical reflection arrivals exhibit kinematics coinciding with those of reflection events in active-source reflection data, but the amplitudes and phases are not directly comparable. So, they are labelled pseudo-physical reflections (Löer et al., 2013, Boullenger and Draganov, 2016).

In relation 2.2, if we substitute the response x_A instead of x_B in the right-hand side, the retrieved Green's function on the left-hand side is the result of AC of the arrivals at receiver x_A, which means x_A acts as a co-located virtual source and receiver:

$$\hat{G}^*(x_A, x_A, \omega) + \hat{G}(x_A, x_A, \omega) \propto \sum_{n=1}^{N} \hat{G}^*(x_A, x_n, \omega)\hat{G}(x_A, x_n, \omega). \tag{2.3}$$

Similar to CC, besides the pseudo-physical reflections, ghost reflections are also retrieved. The retrieved ghost reflection propagates inside a specific layer which represents a reflection for a ghost virtual source to a receiver co-located exactly at the top of that specific layer. Besides the specific ghost reflection which propagates inside one layer, it is possible to retrieve ghost reflections from inside multiple layers, e.g., the ghost reflection from inside the second and the third layer in Figure 2.1c (the red arrows). This retrieved ghost reflection is the result of correlation of the primary reflections from the bottom of the first layer (the blue arrows in 2.1c) and the bottom of the third layer (the purple arrows in Figure 2.1c), and it propagates vertically as the layers are horizontal.

The retrieved ghost reflection in Figure 2.1c (the red arrows) represents a zero-offset reflection arrival. If we use multiple surface receivers at the surface as x_A in relation 2.3 and repeat the AC and summation process, the result is a virtual zero-offset section which provides an image of specific subsurface structures directly in two-way travel time.

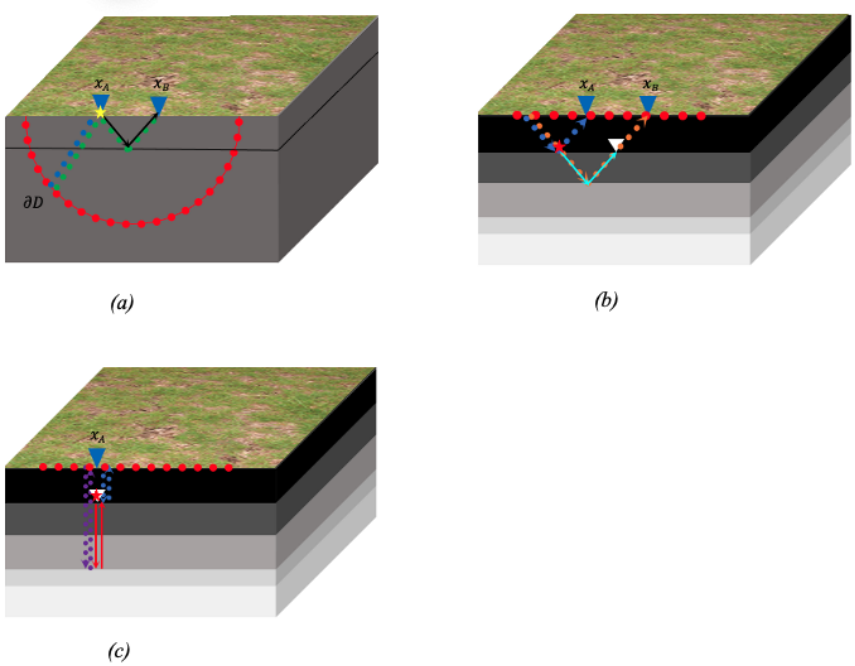

Figure 2.1: Schematic representation of seismic interferometry (SI). (a) The sources (the red dots) are at the source-boundary surface ∂D, which effectively encloses the receivers at x_A and x_B (blue triangles) due to the Earth's free surface. The retrieved virtual-source response contains physical reflections (the black arrow) from the CC of a direct arrival (the blue dotted line) with its surface-related multiple (the green dotted line). The yellow star indicates the virtual source. (b) The sources are on the surface. The retrieved virtual-source response includes pseudo-physical and ghost reflections (e.g., the cyan arrows), in which the ghost reflection is the result of the CC of the primary reflection from the top and the bottom of the second layer (the blue and orange dotted arrows). (c) Same as (b) but for SI by AC. The retrieved virtual-source response includes pseudo-physical and ghost reflections (e.g., the red arrows), in which the ghost reflection is the result of the CC of the primary reflections from the bottom of the first and the bottom of the third layer (the blue and purple dotted arrows). The red star indicates the ghost virtual source, and the white triangle indicates the ghost virtual receiver.

2.3. RESULTS

In this section, we first use numerically modelled data to demonstrate how the ghost reflections can be used for monitoring purposes of shallow subsurface structures. We discuss the results of SI by AC for different conditions of the subsurface model. Second, we show the method's applicability to a shallow subsurface field dataset.

2.3.1. NUMERICALLY MODELLED DATA

We illustrate the potential of SI on data derived from numerical modelling using a shallow subsurface structure from around Rotterdam, the Netherlands
(Ghose and Goudswaard, 2004). Figure 2.2a shows the subsurface model, which consists of five horizontal layers below a free surface.

The fixed receivers were placed from 45.25 m to 95.25 m and the sources were placed

from 30 m to 110 m at the free surface with spacing between neighbouring points of 0.5 m and 1.0 m, respectively. A Ricker wavelet with a centre frequency of 45 Hz was used as a source signature, and a finite-difference modelling code (Thorbecke and Draganov, 2011) in an acoustic mode generates the seismic reflection dataset. This approach is valid as we imitate a 2D field survey for which the shear-wave sources and the horizontal-component receivers are oriented in the direction perpendicular to the line. Because of this orientation and assuming no 3D scattering, the horizontally polarized shear waves (SH-waves) which we record are completely decoupled from the compressional and vertically polarized shear waves.

Figure 2.2b shows the modelled common-source gather for a source located at 70 m. Next to the primary reflections, such as the reflections from the bottom of the first, second, and third layer (the arrivals indicated in Figure 2.2b by the blue, orange, and purple arrows, respectively), also free-surface multiples are present in the shot gather, such as the free-surface multiple of the first layer (the event indicated by the green arrow in Figure 2.2b). Table 2.1 lists the colours corresponding to events in the directly modelled reflection response and the result from SI in Figures 2.1- 2.4.

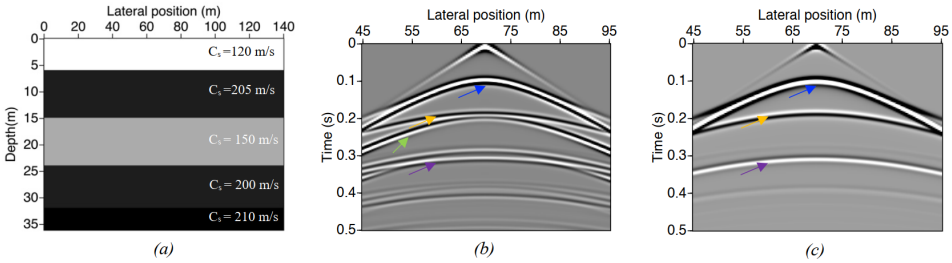

Figure 2.2: (a) Shear-wave velocity (CS) model for the base survey, (b) directly modelled reflection response for an active source at (70,0) m, (c) same as (b) but when the model has an absorbing boundary condition at the surface. The colour-coded arrows indicate the events described in Table 2.1.

Table 2.1: Colour coding of events in the directly modelled reflection response and in the result from SI in Figures 2.1- 2.4

Colour codes in Figure 2.1-2.4	**Explanation**
Blue	Primary reflection from the bottom of the first layer
Orange	Primary reflection from the bottom of the second layer
Purple	Primary reflection from the bottom of the third layer
Green	Surface-related multiple from the bottom of the first layer
Yellow	Combination of pseudo-physical reflections and ghost reflections
Cyan	Ghost reflection from inside the second layer
Pink	Ghost reflection from inside the third layer
Red	Ghost reflection from inside the second and third layer

We applied SI by AC (relation 2.3) to the simulated reflection dataset, such as the active-source gather in Figure 2.2b, to investigate the retrieval of the ghost reflections,

which means that we correlated each signal with itself. Consequently, the zero-offset sections can be retrieved at each receiver location. The virtual zero-offset sections (Figure 2.3) perfectly match the geometry of the specific subsurface interfaces. In our numerical modelling, the subsurface model is horizontal. Therefore, we retrieve the horizontal events in the results of SI by AC, and it is easier to separate different reflections and interpret them. To enhance the clarity of the depicted events in the virtual zero-offset sections, we also show the trace of one receiver at 70.25 m in Figure 2.3.

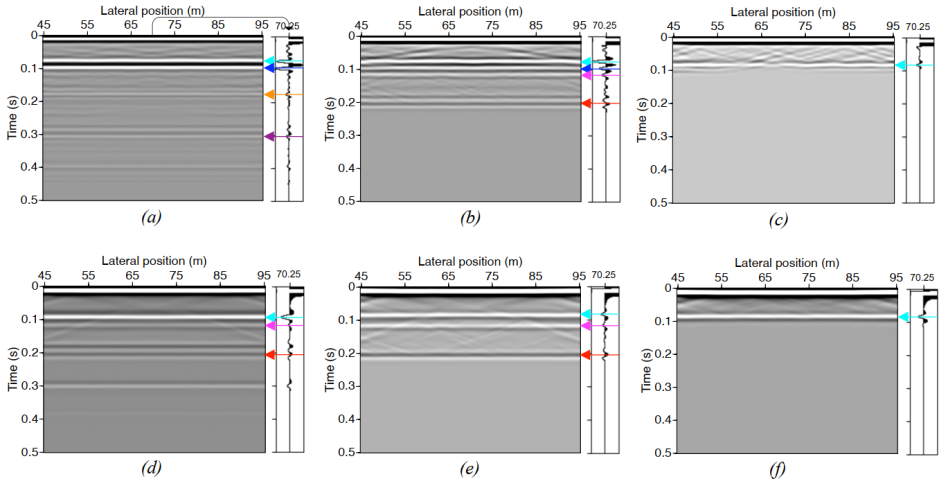

Figure 2.3: Retrieved results of the application of SI by AC to (a) the full active-source gathers, (b) the active-source gathers, which are muted before the reflection from the bottom of the first layer and after the reflection from the bottom of the 3rd layer, (c) the active-source gathers which are muted before the reflections from the bottom of the first layer and after reflection from the bottom of the second layer, (d, e, f) same as (a, b, c) but when the model has an absorbing boundary condition at the surface. The seismic trace next to each image represents the retrieved result for the receiver located at 70.25 m. The colour-coded arrows indicate the events described in Table 2.1.

Figure 2.3a shows the virtual zero-offset section when full active-source gathers are used in SI by AC. We retrieved several horizontal reflections including pseudo-physical and ghost reflections such as the events shown by the cyan, orange, blue and purple arrows. But identifying all ghost reflections is challenging when the full recordings are used for SI by AC, because different retrieved arrivals interfere with each other.

One way to make the result from SI by AC clearer for interpretation of the ghost reflections is to mute the arrivals recorded before and after the reflections that contribute to the retrieval of specific target ghost reflections. Figure 2.3b shows the virtual zero-offset section when we manually muted all events before the reflection from the bottom of the first layer (the arrival indicated by the blue arrow in Figure 2.2b) and after the reflection from the bottom of the third layer (the arrival indicated by the purple arrow in Figure 2.2b). As we can see in Figure 2.3b, we retrieved better the ghost reflections inside the third layer at approximately 0.12 s (the pink arrow) or the ghost reflection from the combination of the second and third layer with an arrival time at approximately 0.21 s (the red arrow). However, the ghost reflection from inside the second layer is unclear

(the cyan arrow in Figure 2.3b). The two-way travel time of each of these ghost reflections corresponds to a specific layer velocity and thickness. E.g., the ghost reflection at 0.21 s traverses the second and the third layers, so its two-way travel time is characterised by the effective velocity of these two layers.

To retrieve the specific ghost reflection that propagates only inside the second layer, we muted the arrivals before the reflection from the bottom of the first layer and after the reflection from the bottom of the second layer in the active-source gathers (the arrivals indicated in 2.2b by blue and orange arrows, respectively) before applying SI by AC. As shown in Figure 2.2b, muting of all unwanted events, such as all direct arrivals at far offsets, is difficult. However, this has very little impact on the result of SI since the direct-wave energy is already weak, and we perform stacking over all active-source gathers. By muting, we expected to retrieve the ghost reflection from the correlation of the primary reflections from top and bottom of the second layer, which propagates only inside the second layer as measured from a ghost virtual source to ghost virtual receivers - both placed directly at the top of the second layer.

Figure 2.3c shows the virtual zero-offset sections derived from application of SI by AC using the thus-muted active-source gathers. We see a clear event at 0.09 s which is the ghost reflection from inside the second layer (the cyan arrow). Some artefacts are observed because it is impossible to mute all undesired reflections for some active-source gathers, especially for the far offsets. Moreover, the primary reflections may be contaminated with free-surface multiples.

As mentioned above, it is still challenging to discriminate all ghost reflections from the pseudo-physical reflections in the results of SI. A better way of achieving this discrimination is to remove the free-surface multiples in the active-source gathers. This precludes retrieval of pseudo-physical reflections and leads to retrieval of only ghost reflections. In numerical modelling, removing the free-surface multiples is easily achieved by defining an absorbing boundary condition at the surface. With this condition, we have only the primaries in the active-source gathers. In field data, it is possible to use surface-related multiples elimination (SRME) (Verschuur, 1991) or estimate the primaries through sparse inversion (EPSI) (van Groenestijn and Verschuur, 2009), which are the two widely accepted tools for free-surface-multiple elimination.

Figure 2.2c shows the common-source gather for an active source located at 70 m, when the absorbing boundary condition is used at the surface. The primary reflections from the bottom of all layers are observable (the blue, orange, and purple arrows in Figure 2.3c). By applying SI to such gathers, we retrieve only ghost reflections. Figure 2.3d shows the zero-offset section retrieved from SI by AC when we define an absorbing boundary condition at the surface. As shown in this figure, we retrieve all ghost reflections from inside all the layers, or the ghost reflections from inside more than one layer. Consequently, it is not easy to separate the specific ghost reflections. Therefore, we used the muted active-source gathers before correlation. Figure 2.3e shows the result of SI by AC when we used the muted active-source gathers containing only the reflection from the bottom of the first, second, and third layers. We retrieved better the ghost reflection inside the second, third, and from inside the second and the third layers together (the cyan, the pink, and the red arrows, respectively, in Figure 2.3e) in comparison with Figure 2.3d. Moreover, by removing the surface-related multiples in the active-source

gathers, we retrieved stronger the ghost reflections, compared to those in Figure 2.3b.

Figure 2.3f shows the virtual zero-offset section resulting from SI by AC using muted active-source gathers that contain reflections only from top and bottom of the second layer. The event around 0.09 s is the ghost reflection from inside the second layer. By comparing with Figure 2.3c, which results from SI by AC using the subsurface model with a free surface at the top, we can see that the retrieved ghost reflection is more robust.

To investigate the application of ghost reflections for monitoring in specific subsurface structures, we looked into retrieving the ghost reflections for different subsurface models shown in Figure 2.4(a-e). Our target layer for monitoring is the second layer. The five models in Figure 2.4 include a base subsurface model (Figure 2.4a (i)) lateral change in velocity in the second layer (Figure 2.4b (i)), a gradual change of velocity with depth in the second layer (Figure 2.4c (i)), a thickness change of the second layer (Figure 2.4d (i)), and finally a 10% velocity increase in the second layer (Figure 2.4e (i)). We applied SI by AC (relation 2.3) to the modelled active-source reflection responses for these subsurface models. Based on the results of SI by AC using the base survey (Figure 2.3), we focused on the result of SI by AC for the muted active-source gathers with an absorbing boundary condition at the surface.

Figures 2.4a-e (ii) show the result of SI by AC for the base subsurface models and the other subsurface models with an absorbing boundary condition at the surface, when we use active-source gathers muted to contain reflections from the bottom of the first, second, and third layers. Figure 2.4a (ii) shows the result of the model for the base survey. This Figure shows, as shown also earlier, we could retrieve the ghost reflection inside the second layer (the cyan arrow), the ghost reflection inside the third layer (the pink arrow), and also the ghost reflection from the combination of these two layers (the red arrow). Similar to Figure 2.3, we have included a single trace from the receiver positioned at 70.25 m to provide a more detailed depiction of the indicated events.

Figure 2.4b (ii) shows the result of SI by AC for the model with a lateral velocity change in the second layer. The ghost reflection of the combination of the second and the third layer is clear at approximately 0.24 s at the horizontal distance of 45 m (the red arrow). It is not possible to distinguish the ghost reflection from inside the second layer and the ghost reflection from inside the third layer clearly. Also, for the model with a gradient change of velocity with depth in the second layer, it is difficult to see the ghost reflection inside the second layer. Again, the ghost reflection inside the third layer (the pink arrow in Figure 2.4c (ii)) and the combination of the second and the third layer (the red arrow in Figure 2.4c (ii)) are clearer.

Figure 2.4d (ii) shows the result of SI by AC for a thickness change in the second layer, while Figure 2.4e (ii) shows the result of SI by AC for a 10% velocity change inside the second layer. In both cases, we retrieved the ghost reflection inside the second and the third layer (the cyan and the pink arrows, respectively) and the ghost reflection from inside these two layers (the red arrow in Figures 2.4d (ii) and 2.4e (ii)).

By comparing the SI result in Figure 2.4a-e (ii), it is obvious that the ghost reflection from inside the second and the third layer (the red arrow) can be used for monitoring purposes, because the differences in time and amplitude as a result of respective changes in the subsurface models are clearly recognisable. However, retrieving the ghost reflections from inside the second layer (the cyan arrow in Figure 2.4a-e (ii)) is more challeng-

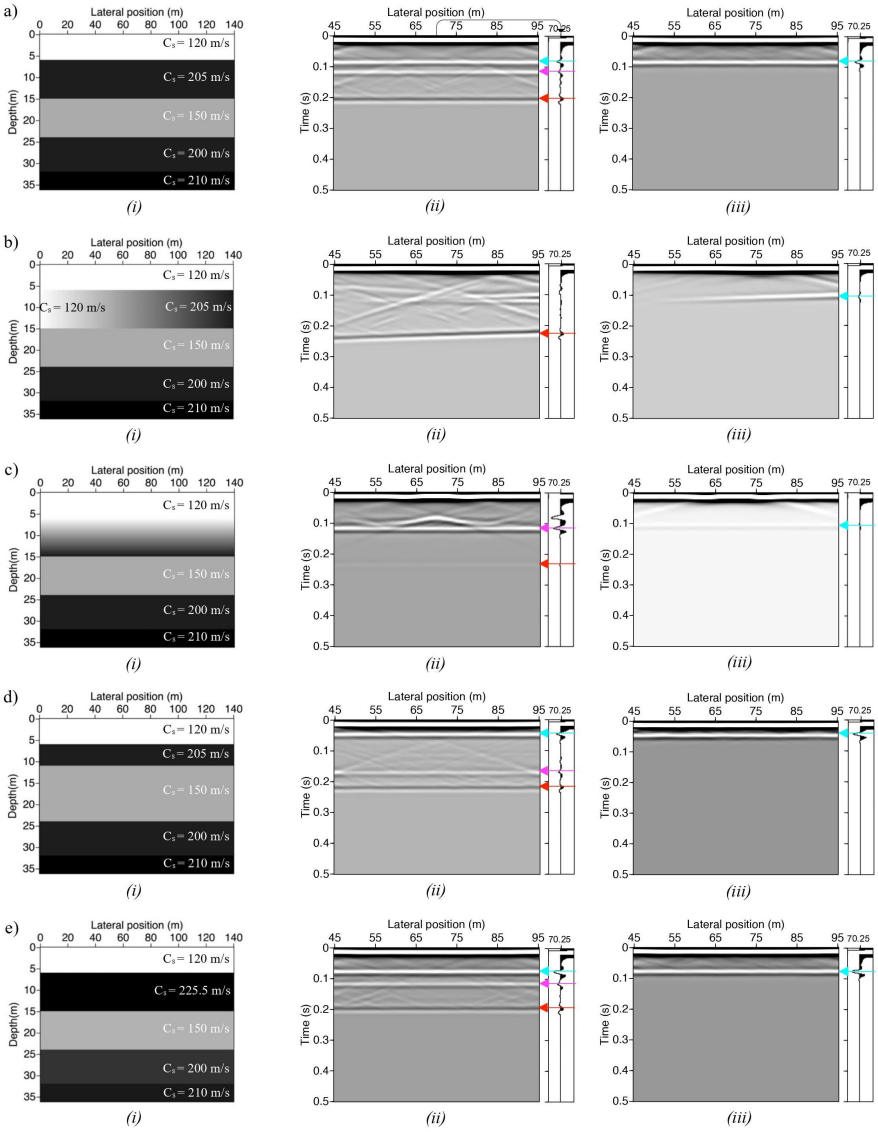

Figure 2.4: (i) Shear-wave velocity (CS) subsurface models used to test the idea of monitoring in case of (a) a base subsurface model, (b) a lateral change in the velocity of the second layer, (c) a gradient change with depth in the velocity of the second layer, (d) a thickness change in the second layer, (e) a 10% velocity change in the second layer. (ii) Retrieved results of SI by AC applied to active-source gathers in which events before the reflections from the bottom of the first layer and after the reflection from the bottom of the third layer are muted for the subsurface models in (i), respectively. (iii) Same as (ii), but SI by AC applied to active-source gathers which were muted before the reflections from the bottom of the first layer and after the reflection from the bottom of the second layer. The seismic trace next to each represents the retrieved result for the receiver located at 70.25 m, and the colour-coded arrows indicate the events described in Table 2.1.

ing with this type of muting because of the interference with the ghost reflection inside the third layer. Nevertheless, the ghost reflection from inside the second layer is recognisable, as indicated by the cyan arrow, and it reveals changes in comparison with the base model (Figure 2.4a (ii)) for the case of the thickness change (Figure 2.4d (ii)) and the velocity change (Figure 2.4e (ii)).

As all changes occur in the second layer of our subsurface models, we further focus on retrieving the ghost reflection from inside the second layer, resulting from the correlation of the primary reflection from the top and the bottom of the second layer. As explained above, we used muting before the reflection from the top of the second layer and after the reflection from the bottom of the second layer, and then applied SI by AC.

Figure 2.4a-e (iii) shows the result of SI by AC applied to the muted active-source gathers. We retrieved only the ghost reflection from inside the second layer (the cyan arrow in Figure 2.4a-e (iii)) – we retrieved a clear and robust arrival at 0.09 s for the base survey (Figure 2.4a (iii)). For the model with a lateral change, we can see that the retrieved ghost reflection has a weak amplitude at a place where it is expected, i.e., at shorter lateral distances (Figure 2.4b (iii)). Figure 2.4c (iii) shows the ghost reflection from inside the second layer for the model with a gradient change of velocity in depth. The retrieved ghost reflection has a lower amplitude than in Figure 2.4d (iii). Figure 2.4e (iii) shows the result of SI by AC in case of thickness change. We see the ghost reflection from inside the second layer at around 0.05 s, which corresponds with the two-way travel time inside the second layer. In the case of a velocity change of 10% (higher than that in the base-survey model), the ghost reflection from inside the second layer shows a time difference of approximately 0.008 s (Figure 2.4e (iii)). For a comparison of the retrieved ghost reflection from inside the second layer, we conclude that the use of layer-specific ghost reflection does allow monitoring the change in thickness and/or velocity of or inside the second layer.

2.3.2. FIELD DATA

After showing the usefulness of retrieving ghost reflections from SI using the numerically modelled data for the five subsurface models, we next test the technique on field data. The site where the data were recorded is located in the western part of the Netherlands, near Rotterdam. The total profile length was 190 m with shot and receiver interval of 1.0 m and 0.5 m, respectively. The sources and receivers moved along a line following an end-on acquisition geometry, which means that the receivers are positioned on the right-hand side of each shot. As shear-wave source, a high-frequency electrodynamic horizontal vibrator (Ghose et al., 1996; Brouwer et al., 1997; Ghose, 2012) oriented in the direction perpendicular to the line was used. The receivers recorded the horizontal particle velocity also in a direction perpendicular to the line. Therefore, we could directly apply to the recorded data the methodology described in the previous subsection.

The geology of this site, known from earlier borehole measurements, comprises of flat alternating layers of Holocene clay and sand (Figure 2.5 (a-b)). The sand is relatively homogeneous. In the topmost part (Holocene), the appearance of sand layers at around 1–2 m, 4–5 m, and 7–12 m depths were marked in several boreholes (Ghose and Goudswaard, 2004).

Figure 2.5c shows one example of the recorded shot gathers after the application of

a pre-processing step, which also included surface-wave suppression via SRME (Verschuur, 1991). Ghose and Goudswaard (2004) illustrated the successful application of SRME on this shallow shear-wave field dataset. Several strong reflection events are visible in the gather corresponding to various sand-clay interfaces. Some examples of raw and preprocessed shot gathers can be found in Figure 5 of Ghose and Goudswaard, 2004.

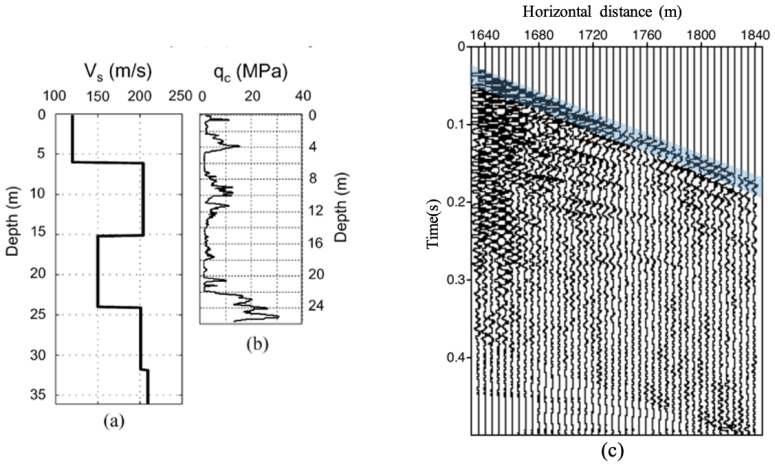

Figure 2.5: (a) Interval velocity obtained from the root-mean-square velocity, and (b) the CPT cone-tip resistance at the same site (Ghose and Goudswaard, 2004). (c) Example of an active-source shot gather, where the source is located at horizontal position 163.5 m (the blue highlighted region shows the extracted reflection arrivals used for SI by AC).

We illustrated in the previous section that, to retrieve better the ghost reflections from inside a specific layer, it is better to use the dataset without surface-related multiples. Therefore, we used the recorded data after the application of the free-surface-related multiple elimination. Moreover, to retrieve a specific ghost reflection, we used tapered muting to extract only the two earliest reflections from the active-source gathers (indicated by the transparent blue area in Figure 2.5c).

We applied SI by AC to all available active-source gathers from these data. We used SI not only to turn sources into virtual receivers (Figure 2.6a), but also to turn the receivers into virtual sources (Figure 2.6b). When we turn the sources into virtual receivers, we sum the AC results over the receivers whose spacing is 0.5 m. The so-retrieved zero-offset section is more reliable, because the spacing of the stacked traces is shorter than the dominant wavelength. When we turn the receivers into virtual sources, we sum over the available sources whose spacing is 1 m. In this case, the spacing is similar to the dominant wavelength, but there are more traces in the ghost zero-offset section, because there are more receiver points than source points. Comparing the result in Figure 2.6a to that in Figure 2.6b, we ascertain the validity of the latter. Thus, for interpretation, we use both results. Note that the retrieval of ghost reflections eliminates any surface statics. Therefore, we have similar ghost reflections in Figures 2.6a and 2.6b, despite the fact that we use common-source gather and common-receiver gather, respectively.

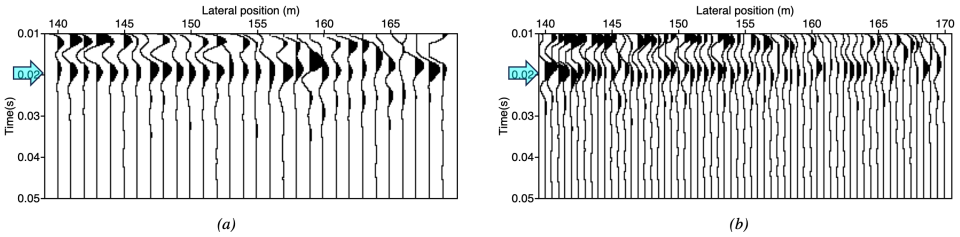

Figure 2.6: Result of SI by AC applied to field data: (a) to turn active sources into virtual receivers and (b) to turn the receivers into virtual sources. The cyan arrows indicate the retrieved ghost reflection.

The ghost zero-offset sections in Figure 2.6 exhibit a ghost reflection at approximately 20 ms (as indicated by the cyan arrows). This ghost reflection is related to the subsurface layer located at 4-6 m depth. It shows a generally horizontal layer with constant thickness except at horizontal distances 156-166 m, where the retrieved ghost reflection indicates local thinning. Based on known geology, we interpret this change in thickness of this specific layer as possibly indicating the appearance of the sand layer at this depth. It is, therefore, possible to use such retrieved ghost reflection for imaging and monitoring of the shallow subsurface.

2.4. DISCUSSION

Applying SI using surface reflection data results in the appearance of ghost reflections in the retrieved virtual-source or virtual-receiver gathers. The ghost reflections result from the correlation of the primary reflections from different depth levels. These ghost reflections are comparable to the spurious multiples as described by Snieder et al. (2006) for one-sided illumination, to virtual refractions (Nichols et al., 2010), and also to ghost reflections due to intrinsic losses (Draganov et al., 2013).

Our study was designed to determine the application of ghost reflections for monitoring and imaging purposes for shallow subsurface applications. In the previous section, we showed that we could successfully retrieve a ghost reflection from the field dataset. The ghost reflection indicated a horizontal layer with constant thickness except at greater horizontal distances, where it indicated local thinning. Using a ghost zero-offset section directly allows us to make such an interpretation, as the retrieved ghost reflections depend kinematically only on the properties of the layer (or layers) that caused them to be retrieved. Draganov et al. (2013) showed that applying SI for the retrieval of ghost reflections eliminates the kinematic influence of the layers above the target one. This means that any possible kinematic influence of the layers above the target layer in the field data is eliminated.

Ghose and Goudswaard (2004) showed a stacked time section of the subsurface structures for the same field data in their Figure 6. They obtained the stacked section through careful data processing, including surface-related multiple elimination as mentioned above, but also careful velocity analysis for normal-moveout correction and stacking. In their Figure 6, one can also observe that the layer between 60 ms and 100 ms exhibits

local thinning between common-midpoint numbers 670 and 700. This is also the target layer for which we retrieved the ghost zero-offset section in Figure 2.6. Our results actually confirm that the local thinning is indeed real and not caused by less accurate velocity picking for layers above the target one. This comparison shows that the stacked time section or depth section can be utilised for interpreting the changes in ghost reflections by observing the specific primary reflections used for retrieving ghost reflections. However, they cannot be directly employed for a straightforward comparison with the retrieved ghost reflections because the ghost reflections can only be observed in the virtual zero-offset section retrieved from SI (by AC). We show the comparison of the zero-offset section obtained directly from full active-source data for the subsurface model shown in Figure 2.2a, and the virtual zero-offset section retrieved from SI by AC in section 2.6.1.

We showed the first application of ghost reflections in shallow subsurface studies. We applied SI to turn receivers into virtual sources and to turn shots into virtual receivers. Choosing one and/or the other would depend on the used acquisition geometry of a dataset that is available, e.g., on shot and receiver spacings and on the number of traces in common-receiver gathers and common-source gathers.

As mentioned earlier, the result of SI by AC is a zero-offset section which is retrieved without any other processing. The results we showed are obtained for a horizontally layered medium. It is also possible to retrieve ghost reflections in complex structures such as faults, dipping layers, pinch-outs, etc. (Shirmohammadi et al., 2022 and Draganov et al., 2012). Moreover, the significant advantage of ghost reflections of being sensitive to the changes only inside the layer that caused them to appear in the SI results makes the developed methodology for retrieval of ghost reflections very interesting not only for monitoring shallow subsurface structures but also for the deep structure such as fluid reservoirs or temporal and cyclic storage of H_2 and CO_2.

We showed that eliminating the surface-related multiples and muting all other events but the specific primary reflections from the top and bottom of the target layer(s) results in retrieved ghost reflections that are clearer and more robust (see Figure 2.3(e,f) in comparison with Figures 2.3d and 2.3(b-c)). However, extracting reflection signals from both the top and bottom of the target layer from a field dataset requires those events to be clearly interpretable in the field data set. This might pose a challenge due to interference with surface waves, surface-related multiples, and other undesired events, highlighting a constraint in our suggested approach. Therefore, it is advisable to implement careful data processing prior to SI, as demonstrated in our field dataset example. Nevertheless, for specific subsurface situations, the retrieved ghost reflections could still be contaminated by artefacts in some receiver locations because of the effect of other undesired reflections in the active-source gathers (Figure 2.4b-c (ii)). Therefore, it is worth mentioning that for some conditions where retrieving a strong ghost reflection of a specific layer is problematic, it is also possible to look at the ghost reflections which propagate inside more than one layer, such as the one shown in Figure 2.4a-e (ii).

We also applied SI by CC, which resulted in retrieved multi-offset gathers (see section 2.6.2). The results of SI by CC are particularly important for further use of ghost reflections in velocity analysis for estimating the velocity inside specific layers. We attempted to apply velocity analysis to the SI results on the field dataset, but the result was not very stable. The reason for this might be the low, and thus insufficient, number of traces in

the retrieved common-midpoint gathers. Therefore, using a fixed receiver geometry in field acquisitions for the application of SI for the retrieval of ghost reflections is recommended.

2.5. CONCLUSION

We investigated the application of ghost reflections for shallow subsurface imaging and monitoring purposes. We retrieved ghost reflections using seismic interferometry (SI) by auto-correlation (AC) applied to seismic reflection data recorded with active sources and receivers at the surface.

Using a numerically modelled dataset for a horizontally layered subsurface, we illustrated that the retrieved ghost reflections can be used to monitor changes in a specific layer that causes the ghost reflections to appear in the SI results. Additionally, we proposed to eliminate the surface-related multiples in the active-source gathers and mute undesired events before applying SI to improve the retrieval of the ghost reflections.

We applied the methodology for retrieval of ghost reflections using SI by AC to shallow subsurface shear-wave data acquired at a site located close to Rotterdam, the Netherlands. The retrieved zero-offset section directly showed the geometry of a layer at a depth of 4-6 m. The retrieved virtual zero-offset section allowed interpreting of the local thinning of this specific layer. Our study can be helpful in other ghost-reflection applications in monitoring and/or imaging shallow or deeper subsurface structures.

2.6. SUPPLEMENTARY MATERIAL

2.6.1. COMPARISON OF THE ZERO-OFFSET SECTIONS RETRIEVED FROM SI AND EXTRACTED FROM THE ACTIVE-SOURCE DATA

We compared the virtual zero-offset section retrieved from seismic SI by AC with the zero-offset section obtained using active-source data. Figure 2.7(a) shows the zero-offset gathers obtained directly from full active-source data for the subsurface model shown in Figure 2.2a without any processing. We can see various primary reflections, such as those from the bottom of the first, second, and third layers (marked by the blue, orange, and purple arrows, respectively), as well as free-surface multiples (for illustration, one marked by the green arrow). Figure 2.7(a) can be directly compared with Figure 2.7(b), which is the virtual zero-offset section obtained from SI by AC using full active-source data. Comparing these two sections, we can see that several horizontal reflections are retrieved in the virtual zero-offset section, both pseudo-physical and ghost reflections. The pseudo-physical reflections exhibit kinematics similar to those of reflection events in the active-source reflection data (marked by the blue, orange, and purple arrows). But we can only observe ghost reflections in the virtual zero-offset gathers, such as the ghost reflection from inside the second layer (marked by the cyan arrow in Figure 2.7(b)) and the ghost reflection from the combination of the second and third layer (marked by the red arrow in Figure 2.7(b)).

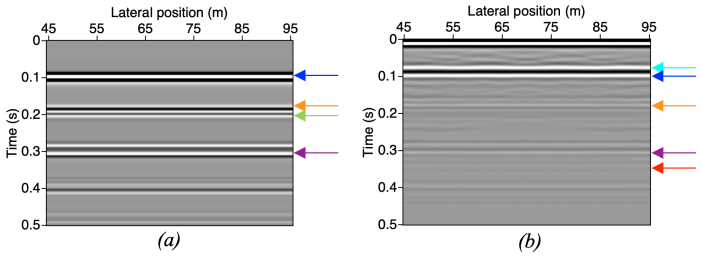

Figure 2.7: (a) The zero-offset section obtained using the full active-source data for the subsurface model shown in Figure 2.7a, (b) the virtual zero-offset section retrieved from SI by AC using the full active-source gathers. the colour-coded arrows indicate the events described in Table 2.1.

2.6.2. GHOST REFLECTIONS RETRIEVED FROM SEISMIC INTERFEROMETRY BY CROSS-CORRELATION (SI BY CC)

Besides SI by AC, we applied SI by CC. We used the synthetic dataset, like the active-source gather in Figure 2.2b, to retrieve a virtual-source gather for a virtual source at 70 m. We applied the CC and summation process from relation 2.2 to all the modelled active-source gathers. Here, we show the summation of the causal and acausal parts of the retrieved responses. We can do that as we expect the causal and acausal times to be symmetric around t=0 s because there are active sources and receivers on both sides of the virtual source. If, for example, the virtual source is chosen at the position of one of the left-most receivers, most of the useful retrieved arrivals (pseudo-physical and ghost reflections) will be retrieved at acausal times (Ruigrok et al., 2010), and thus only the acausal part can be used.

Figure 2.8(a) shows the retrieved virtual-source gather for a virtual source at 70 m using SI by CC. It shows that we retrieve different arrivals from the subsurface layers, including pseudo-physical and ghost reflections; the yellow arrows at 0.12 s and 0.21 s for a horizontal distance of 70 m in Figure 2.8(a) indicate interference of such reflections. In general, the pseudo-physical reflections result from the correlation of primaries with their surface-related multiples, while the ghost reflections are the result of the correlation of primaries, internal multiples, or their combination. For example, the correlation of the primary reflection from the bottom of the first layer (the blue arrow in Figure 2.2b) with its free-surface multiple (the green arrow in Figure 2.2b) results in the retrieval of the pseudo-physical reflection from the bottom of the first layer. On the other hand, the correlation of the primary reflection from the bottom of the first layer (the blue arrow in Figure 2.2b) with the primary reflection from the bottom of the third layer (the purple arrow in Figure 2.2b) results in the retrieval of a ghost reflection that appears to have propagated only inside the second and third layer. However, identifying the ghost reflections might be challenging when the full recordings are used for SI by CC, as can be seen in Figure 2.8(a), because different retrieved arrivals interfere with each other.

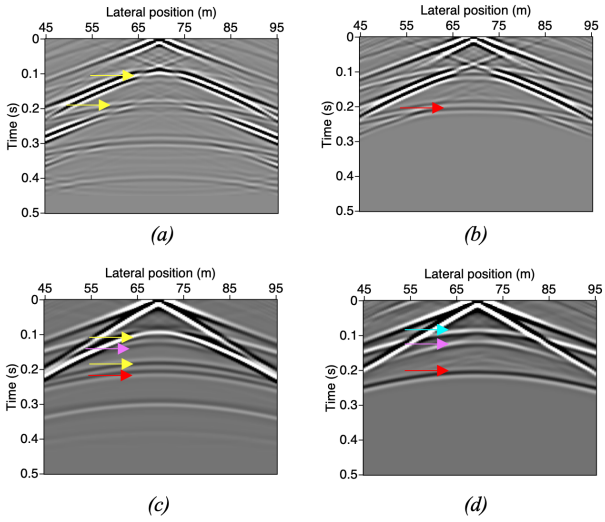

Figure 2.8: (a) Retrieved results of SI by CC for a virtual source at (70,0) m. (b) As in (a), but for active-source gathers which are muted before the reflection from the bottom of the 1st layer and after the reflection from the bottom of the 3rd layer, (c, d) same as (a, b) but when the model has an absorbing boundary condition at the surface. The colour-coded arrows indicate the events described in Table 2.1

As mentioned in the result section, one way to make the result of SI clearer for interpretation of the ghost reflections is to mute the arrivals recorded before and after the reflections that contribute to the retrieval of specific target ghost reflections. Figure 2.8(b) shows the result retrieved from SI by CC for a virtual source at a lateral position 70 m when we used reflection panels with muted arrivals before the reflection from the bottom of the first layer (the arrival indicated by the blue arrow in Figure 2.2b) and after reflection from the bottom of the third layer (the arrival indicated by the purple arrow in Figure 2.2b).

Comparing the result in Figure 2.8(b) with the result in Figure 2.8(a), we can see that the retrieved ghost reflection in Figure 2.8(b) (the red arrow) is clearer and more robust, which is a result of selecting and correlating specific arrivals in the recorded reflection panels. This ghost reflection results from the correlation of the primary reflections from the bottom of the first and the third layer (the blue and the purple arrows in Figure 2.2b, respectively).

We applied SI by CC to the modelled common-source gathers where an absorbing boundary condition is defined at the surface, like the one in the example of an active-source gather in Figure 2.2c. Figure 2.8(c) exhibits the resulting virtual common-source gather for a virtual source at 70 m. The observed events are all ghost reflections, but some of them interfere with each other (the yellow arrows). Nevertheless, the ghost reflection from inside the third layer (the pink arrow in Figure 2.8(c)), and the ghost reflection from inside the second and the third layer are retrieved clearer than in Figure 2.8(a) (the red arrow in Figure 2.8(c)). Thus, to retrieve even clearer ghost reflections that propagate inside specific target layers, it is better to mute the events other than the primary reflec-

tions in the active-source gathers, as we did above.

Figure 2.8(d) shows the result retrieved from SI by CC for a virtual source at 70 m for muted arrivals before the reflection from the bottom of the first layer (the blue arrow in Figure 2.2c) and after the reflection from the bottom of the third layer (the purple arrow in Figure 2.2c). Comparing Figure 2.8(d) with Figure 2.8(c), we can see we retrieve clearer, i.e., better ghost reflections. Such as the ghost reflection from the second layer at 0.09 s for the receiver at 70 m (the cyan arrow in Figure 2.8(d)), which is a result of the correlation of the primary reflections from the top and the bottom of the second layer (the blue and the orange arrows in 2.2c). We can also distinguish the ghost reflection from inside the third layer at 0.12 s for the receiver at 70 m (the pink arrow in Figure 2.8(d)) and the ghost reflection from inside the second and the third layer at 0.21 s for the receiver at 70 m (the red arrow in Figure 2.8(d)).

2.7. DATA AVAILABILITY

The data and codes underlying this chapter are available in repository 4TU.ResearchData at https://doi.org/10.4121/2a36a6ae-07fc-4592-8c27-19e3efafd696.

REFERENCES

Boullenger, B., & Draganov, D. (2016). Interferometric identification of surface-related multiples. *Geophysics*, *81*(6), Q41–Q52. https://doi.org/10.1190/GEO2015-0450.1

Brouwer, J., Ghose, R., Helbig, K., & Nijhof, V. (1997). The improvement of geotechnical subsurface models through the application of S-wave reflection seismic exploration. *3rd EEGS Meeting*, 95–00027. https://doi.org/10.3997/2214-4609.201407288

Curtis, A., & Halliday, D. (2010). Directional balancing for seismic and general wavefield interferometry. *Geophysics*, *75*(1), SA1–SA14. https://doi.org/10.1190/1.3298736

Curtis, A., Nicolson, H., Halliday, D., Trampert, J., & Baptie, B. (2009). Virtual seismometers in the subsurface of the Earth from seismic interferometry. *Nature Geoscience*, *2*(10), 700–704. https://doi.org/10.1038/ngeo615

Draganov, D., Heller, K., & Ghose, R. (2012). Monitoring CO2 storage using ghost reflections retrieved from seismic interferometry. *International Journal of Greenhouse Gas Control*, *11*(SUPPL), S35–S46. https://doi.org/10.1016/j.ijggc.2012.07.026

Draganov, D., Ghose, R., Heller, K., & Ruigrok, E. (2013). Monitoring changes in velocity and Q using non-physical arrivals in seismic interferometry. *Geophysical Journal International*, *192*(2), 699–709. https://doi.org/10.1093/gji/ggs037

Draganov, D., Ghose, R., Ruigrok, E., Thorbecke, J., & Wapenaar, K. (2010). Seismic interferometry, intrinsic losses and Q-estimation. *Geophysical Prospecting*, *58*(3), 361–373. https://doi.org/10.1111/j.1365-2478.2009.00828.x

Ghose, R., Brouwer, J., & Nijhof, V. (1996). A Portable S-wave vibrator for high-resolution imaging of the shallow subsurface, 1–2. https://doi.org/10.3997/2214-4609.201408721

Ghose, R. (2012). A microelectromechanical system digital 3C array seismic cone penetrometer. *Geophysics*, *77*(3), WA99–WA107. https://doi.org/10.1190/geo2011-0266.1

Ghose, R., & Goudswaard, J. (2004). Integrating S-wave seismic-reflection data and cone-penetration-test data using a multiangle multiscale approach. *Geophysics*, *69*(2), 440–459. https://doi.org/10.1190/1.1707064

Halliday, D., Curtis, A., Robertsson, J. O., & van Manen, D. J. (2007). Interferometric surface-wave isolation and removal. *Geophysics*, *72*(5), A69–A73. https://doi.org/10.1190/1.2761967

Harmankaya, U., Kaslilar, A., Thorbecke, J., Wapenaar, K., & Draganov, D. (2013). Locating near-surface scatterers using non-physical scattered waves resulting from seismic interferometry. *Journal of Applied Geophysics*, *91*, 66–81. https://doi.org/10.1016/j.jappgeo.2013.02.004

King, S., & Curtis, A. (2012). Suppressing nonphysical reflections in Green's function estimates using source-receiver interferometry. *Geophysics*, *77*(1), Q15–Q25. https://doi.org/10.1190/geo2011-0300.1

King, S., Curtis, A., & Poole, T. L. (2011). Interferometric velocity analysis using physical and nonphysical energy. *Geophysics*, *76*(1), SA35–SA49. https://doi.org/10.1190/1.3521291

Löer, K., Meles, G. A., Curtis, A., & Vasconcelos, I. (2013). Diffracted and pseudo-physical waves from spatially limited arrays using source-receiver interferometry (SRI). *Geophysical Journal International*, *196*(2), 1043–1059. https://doi.org/10.1093/gji/ggt435

Ma, X., Kirichek, A., Heller, K., & Draganov, D. (2022). Estimating P- and S-Wave velocities in fluid mud using seismic interferometry. *Frontiers in Earth Science*, *10*, 1–11. https://doi.org/10.3389/feart.2022.806721

Ma, X., Kirichek, A., Shakeel, A., Heller, K., & Draganov, D. (2021). Laboratory seismic measurements for layer-specific description of fluid mud and for linking seismic velocities to rheological properties. *The Journal of the Acoustical Society of America*, *149*(6), 3862–3877. https://doi.org/10.1121/10.0005039

Nichols, J., Mikesell, D., & Van Wijk, K. (2010). Application of the virtual refraction to near-surface characterization at the Boise Hydrogeophysical Research Site. *Geophysical Prospecting*, *58*(6), 1011–1021. https://doi.org/10.1111/j.1365-2478.2010.00881.x

Ruigrok, E., Campman, X., Draganov, D., & Wapenaar, K. (2010). High-resolution lithospheric imaging with seismic interferometry. *Geophysical Journal International*, *183*(1), 339–357. https://doi.org/10.1111/j.1365-246X.2010.04724.x

Ruigrok, E., Wapenaar, K., Van Der Neut, J. R., & Draganov, D. S. (2009). A review of crosscorrelation and multidimensional deconvolution seismic interferometry for passive data. *Passive Seismic Workshop: Case Studies and Applications for Field Development and Exploration*, 1–7. https://doi.org/10.3997/2214-4609.20146735

Shirmohammadi, F., Draganov, D., Balestrini, F., & Ghose, R. (2022). Application Of seismic interferometry with non-Physical reflections using near-surface seismic field

data. *NSG2022 28th European Meeting of Environmental and Engineering Geophysics*, *2022*(1), 1–5. https://doi.org/10.3997/2214-4609.202220075

Snieder, R., Miyazawa, M., Slob, E., Vasconcelos, I., & Wapenaar, K. (2009). A comparison of strategies for seismic interferometry. *Surveys in Geophysics*, *30*(4-5), 503–523. https://doi.org/10.1007/s10712-009-9069-z

Snieder, R., Wapenaar, K., & Larner, K. (2006). Spurious multiples in seismic interferometry of primaries. *Geophysics*, *71*(4), SI111–SI124. https://doi.org/10.1190/1.2211507

Thorbecke, J. W., & Draganov, D. (2011). Finite-difference modeling experiments for seismic interferometry. *Geophysics*, *76*(6), H1–H18. https://doi.org/10.1190/geo2010-0039.1

van Groenestijn, G. J., & Verschuur, D. J. (2009). Estimating primaries by sparse inversion and application to near-offset data reconstruction. *Geophysics*, *74*(3), A23–A28. https://doi.org/10.1190/1.3111115

Verschuur, D. J. (1991). *Surface-related multiple elimination, an inversion approach* [Ph.D. thesis]. Delft University of Technology [Available at http://resolver.tudelft.nl/uuid:09df29e2-9487-4fe6-87e0-c2a9470933d7].

Wapenaar, K., & Fokkema, J. (2006). Green's function representations for seismic interferometry. *Geophysics*, *71*(4), SI33–SI46. https://doi.org/10.1190/1.2213955

3

FEASIBILITY OF RESERVOIR MONITORING IN THE GRONINGEN GAS FIELD USING GHOST REFLECTIONS

We aim to use the ghost reflections for monitoring subsurface changes, to address challenges associated with detecting and isolating changes within the target layer in monitoring. We focus on the feasibility of monitoring pore-pressure changes in the Groningen gas field in the Netherlands using ghost reflections. To achieve this, we utilise numerical modelling to simulate scalar reflection data, deploying sources and receivers at the surface. To build up subsurface models for monitoring purposes, we perform an ultrasonic transmission laboratory experiment to measure S-wave velocities at different pore pressures. Applying SI by auto-correlation to the modelled datasets, we retrieve zero-offset ghost reflections. Using a correlation operator, we determine time differences between a baseline survey and monitoring surveys. To enhance the ability to detect small changes, we propose interpolating the ghost reflections to finer time sampling before the correlation operator and using only virtual sources with a complete illumination of receivers. We demonstrate that the retrieved time differences between the ghost reflections exhibit variations corresponding to velocity changes inside the reservoir. This highlights the potential of ghost reflections as valuable indicators for monitoring even small changes. We also investigate the effect of the sources and receivers' geometry and spacing and the number of virtual sources and receivers in retrieving ghost reflections with high interpretability resolution.

This Chapter was published as Shirmohammadi, F., Draganov, D., Veltmeijer, A., Naderloo, M., & Barnhoorn, A. (2024) Feasibility of reservoir monitoring in the Groningen gas field using ghost reflections from seismic interferometry. *Geophysical Journal International, 237(2)*, 1018–1029. https://doi.org/10.1093/gji/ggae099
Minor modifications have been applied to keep consistency within the thesis.

3.1. INTRODUCTION

Subsurface activities, such as CO_2 storage, oil and gas production, and geothermal energy production, involve substantial transportation of fluids, either into or out of geological formations. The changed pore-fluid pressure can result in potential risks such as induced seismicity (Bourne et al., 2014) or surface subsidence. Therefore, detecting temporal variations in subsurface characteristics is crucial for risk mitigation. Numerous time-lapse seismic studies have demonstrated the feasibility of detecting temporal variations in subsurface characteristics.

Time-lapse seismic studies compare an initial baseline study with subsequent monitoring studies (Lumley, 2001, MacBeth et al., 2020). For instance, Landrø (2001) explored the use of seismic amplitude analysis to assess changes in pressure and fluid saturation. Roach et al. (2015) employed two 3D time-lapse surveys at a CO_2 storage site to monitor CO_2 injection processes. Additionally, Hatchell and Bourne (2005) investigated the observation of compaction in reservoirs through seismic-attributes analysis.

Amplitude, travel time, and their combination can be used as seismic attributes for the purpose of time-lapse studies (MacBeth et al., 2020; van IJsseldijk et al., 2023; Trani et al., 2011). However, complex overburden structures can complicate the seismic response and obscure the desired temporal variations. The presence of geological features such as faults or heterogeneities in the overlying layers can distort the seismic signals and make isolating the changes of the target layer challenging. Moreover, detecting small reservoir changes presents a significant challenge due to noise interference and limited sensitivity. These factors can make detecting changes in the subsurface more difficult. In order to address those challenges, we aim to show the feasibility of using ghost reflections retrieved from seismic interferometry (SI) to monitor small temporal variations in subsurface characteristics.

SI refers to retrieving seismic responses through, e.g., cross-correlation, auto-correlation, or deconvolution of seismic observations at locations of seismic receivers or sources (Wapenaar and Fokkema, 2006, Schuster, 2009, Wapenaar et al., 2010). When using a dataset from active sources and receivers at the surface, ghost (non-physical) reflections are retrieved from SI because of insufficient destructive interferences (Snieder et al., 2006, Draganov et al., 2010, King and Curtis, 2012). Such ghost reflections propagate inside a specific layer or group of layers. This can be used advantageously for monitoring changes inside those specific layers, e.g., a gas reservoir or CO_2 reservoir. Draganov et al. (2012) verified this concept by conducting numerical modelling and scaled laboratory experiments to monitor CO_2 storage. Furthermore, Ma et al. (2022) showed that ghost reflections can be used to monitor the geotechnical behaviour of fluid mud using ultrasonic reflection measurements in a laboratory. In another study, Shirmohammadi et al. (2024) investigated the potential application of ghost reflections for characterising specific layers in the shallow subsurface as shown in Chapter 2. They demonstrated the technique's effectiveness using synthetic data for a subsurface model with a lateral change in velocity, a velocity gradient in depth, a thickness change, a velocity change of the target layer, and also a shallow field dataset.

To demonstrate the feasibility of using ghost reflections for monitoring reservoir pressure changes, we use the Groningen gas field as a well-known example of an onshore gas field in Europe, located in the Netherlands. The extraction of natural gas from this field

since 1963 has led to a series of seismic events (van Eijs et al., 2006, and Muntendam-Bos et al., 2022). The occurrence of such seismic activity has raised concerns regarding the need for effective monitoring methods. A number of studies suggest using SI for monitoring the Groningen subsurface. Brenguier et al. (2020) used a passive-seismic monitoring approach to detect velocity changes in the Groningen reservoir using ballistic waves recovered from seismic noise correlations. Their methodology requires dense arrays of seismic sensors. For the same gas reservoir, Zhou and Paulssen (2020) investigated the potential of passively recorded deep borehole noise data to detect temporal variations using SI by deconvolution. They showed the possibility of monitoring small temporal changes in the Groningen gas field if repeating noise sources are available. Using the same approach, Zhou and Paulssen (2022) showed that the observed travel-time changes in P-wave and P-to-S converted waves could be related to fluctuations of the gas-water contact in the observation well.

We use a synthetic reflection dataset from the Groningen subsurface model to illustrate our approach of using ghost reflections for monitoring. To build up the subsurface model for the baseline survey and the monitoring surveys, we perform an ultrasonic laboratory experiment to measure the direct S-wave velocities for variations in the reservoir-rock pore pressures using in-situ conditions of pore pressure, stress, and confining pressure. We use the velocities measured in the laboratory experiment at different pore pressures to determine the effect of pressure depletion on the time-lapse changes of seismic velocity of the Groningen reservoir to see whether we can pick up those velocity changes using ghost reflections.

After building up subsurface models, we apply SI by auto-correlation (SI by AC) to the synthetic reflection data to retrieve ghost reflections from inside the Groningen reservoir for the baseline survey and monitoring surveys. To determine the time difference in the reservoir, we use a correlation operator between the ghost reflection retrieved from the baseline survey and the monitoring surveys. To validate our approach, we also calculate the (relative) time difference of the ghost reflections from monitoring surveys with the baseline survey using the expected time difference. Moreover, we discuss the source and receiver configuration for future practical applications of ghost-reflection retrieval using the field dataset.

Below, we first present in section 3.2 the methodology of retrieving ghost reflections with SI and calculating the time differences between the baseline survey and the monitoring surveys, as well as the validation process. Then, in section 3.3.1, we show the results of SI by AC when applied to data from numerical modelling for the baseline survey. Subsequently, in section 3.3.2, we discuss time-lapse investigation using ghost reflections. In section 3.3.3, we also investigate the influence of the source and receiver configuration in retrieving high-resolution ghost reflections. This is followed by a discussion to address challenges, provide recommendations for the practical application of our approach, and then draw conclusions.

3.2. METHOD

For an active-source reflection seismic survey, where the sources (the red stars in Figure 3.1) and receivers (the blue triangles in Figure 3.1) are restricted to the surface, the frequency-domain response $\hat{G}(x_B, x_A, \omega)$ and its complex conjugate at x_B from a virtual

source at x_A can be obtained from the equation (Halliday et al., 2007):

$$\hat{G}^*(x_B, x_A, \omega) + \hat{G}(x_B, x_A, \omega) \propto \sum_{n=1}^{N} \hat{G}^*(x_A, x_n, \omega)\hat{G}(x_B, x_n, \omega). \tag{3.1}$$

The right-hand side of this equation corresponds in the time domain to a cross-correlation between two observations at positions x_A and x_B, both originating from active sources located at x_n at the surface. The symbol $(*)$ shows the complex conjugate in the frequency domain, while N represents the total number of active sources at the surface. Given the source-receiver reciprocity theorem, x_A and x_B can also represent the positions of the active sources, and the obtained response on the left-hand side of Equation 3.1 corresponds to the frequency domain response at virtual receivers. In this case, we turn the active sources into virtual receivers, while N represents the number of receivers at the surface.

The theory behind SI requires having sources which effectively surround the receivers completely. When the positions x_n are at the surface, like for Equation 3.1 (the red stars in Figure 3.1) as in a typical active-source exploration survey, one-sided illumination of the receivers occurs (Wapenaar, 2006). A consequence of the one-sided illumination is that the application of Equation 3.1 will retrieve not only the desired (pseudo-) physical reflections but also ghost reflections. (Note that we labelled the retrieved reflection arrivals as pseudo-physical reflections because they exhibit kinematics coinciding with those of reflections in active-source reflection data, but the amplitudes and phases are not directly comparable (Löer et al., 2013)).

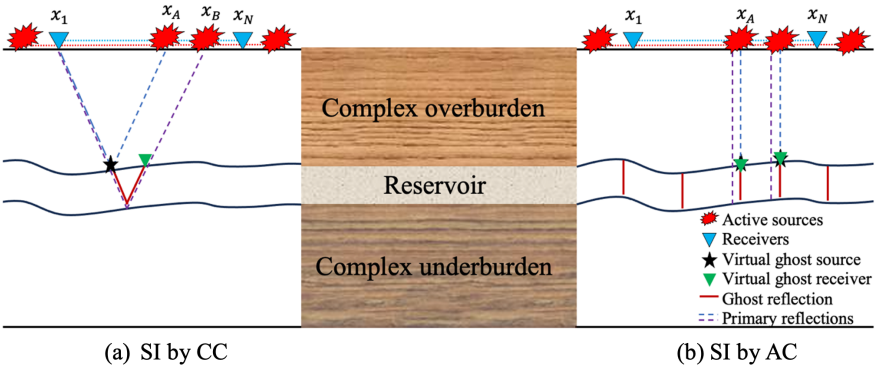

Figure 3.1: Schematic representation of seismic interferometry by (a) cross-correlation (CC) and (b) auto-correction (AC). The ghost reflections (red lines) are retrieved from the correlation of the primary reflections from the top and the bottom of the reservoir (the blue and the purple dotted lines, respectively) from the active sources (the red stars) and recorded at the receivers (the blue triangles) at the surface. The black stars and the green triangles indicate virtual ghost sources and receivers, respectively.

Ghost reflections are retrieved primarily from the correlation of two primary reflections from two different depth levels. For example, the ghost reflection inside the reservoir (red lines in Figure 3.1) can be retrieved by correlation of the primary reflection from the top and bottom of the reservoir (the blue and the purple dotted lines, respectively,

in Figure 3.1). These ghost reflections propagate only inside the reservoir without any kinematic effect of the overburden and underburden; they are equivalent to reflections by a virtual ghost receiver (the green triangle in Figure 3.1) due to a virtual ghost source (the black star in Figure 3.1). Note that this approach is only valid for SI by AC, and for the application of SI by CC, it is necessary to assume that there are no local changes of velocity in the overburden between the points x_A and x_B.

If we substitute the response at x_A instead of the response at x_B in the right-hand side of Equation 3.1, x_A acts as a collocated virtual source and receiver, which means we perform SI by AC and the result represents a zero-offset reflection trace at x_A:

$$\hat{G}^*(x_A,x_A,\omega)+\hat{G}(x_A,x_A,\omega)\propto\sum_{n=1}^{N}\hat{G}^*_{b/m}(x_A,x_n,\omega)\hat{G}_{b/m(}x_A,x_n,\omega). \tag{3.2}$$

In order to improve the accuracy of retrieving a specific ghost reflection, e.g., the ghost reflection inside the reservoir, we implement a process of muting observations before the reflection from the top of the reservoir and after the reflection from the bottom of the reservoir, which are used in the right-hand-side of Equation 3.2 ($\hat{G}_{b/m}(x_A,x_n,\omega)$). As a result, the Green's functions on the left-hand of Equation 3.2 contain only the ghost reflection from inside the reservoir, which we refer to as $C^A_{b/m}(x_A,\omega)$ for simplification in further equations. We apply Equation 3.2 for a baseline survey and a monitoring survey. So, a subscript "b" would denote the baseline survey, while a subscript "m" would denote the monitoring survey. If we apply Equation 3.2 to all the active sources, a ghost zero-offset section is retrieved directly (the red lines of Figure 3.1b) corresponding to both the baseline survey and the monitoring survey. Subsequently, by obtaining these zero-offset sections for both surveys, we determine the time difference (CC^A_m) using a correlation operator between the ghost reflection of the baseline survey and monitoring survey:

$$CC^A_m=|argmax(FT^{-1}(C^{A*}_b(x_A,\omega)C^A_m(x_A,\omega)))|. \tag{3.3}$$

The right-hand side of Equation 3.3 represents multiplication between two terms in the frequency domain: $C^{A*}_b(x_A,\omega)$, which presents the ghost reflection retrieved from the baseline survey at the source (or receiver) location x_A, and $C^A_m(x_A,\omega)$, which represents the ghost reflection retrieved from the monitoring survey at the source (or receiver) location x_A. The symbol $(*)$ denotes the complex conjugate. Thus, we use an inverse Fourier transform of this multiplication as described by (FT^{-1}), then determine the time difference by identifying the absolute value of the maximum within this correlation.

Since our technique is being applied to a numerically modelled dataset, we can evaluate the retrieved time differences. First, we determine the expected time difference for a monitoring survey:

$$\Delta T_m=|t^{cal}_b-t^{cal}_m|, \tag{3.4}$$

where, t^{cal}_b is the calculated arrival time of the ghost reflection for the baseline survey and t^{cal}_m is the calculated time of the ghost reflections for the monitoring survey. Assuming a constant thickness for the reservoir and no lateral velocity changes within the reservoir in our subsurface model for numerical modelling, the ghost reflections exhibit the same arrival time at all virtual receiver positions. Consequently, we can apply averaging of the retrieved time differences over the positions to simplify the validation process.

To accomplish this, we compare the retrieved time difference from the ghost reflection (CC^A_m in Equation 3.3) with the expected time difference (ΔT_m in Equation 3.4). Given that the time difference inside the reservoir may exhibit varying scales across different monitoring surveys, we compute the average relative time difference (RT_m) between the retrieved time differences and expected time difference:

$$RT_m = \sum_{A=1}^{Vr} \frac{|CC^A_m - \Delta T_m|}{\Delta T_m} / Vr, \tag{3.5}$$

where Vr is the number of the virtual receivers. Note that we only use this equation for validation of our technique when we know that there is a difference between the base survey and the monitoring survey and ΔT_m is nonzero.

Up to this point, we have been considering the virtual receivers individually. Given our assumption about the subsurface model, we can also calculate the time difference for the stacked ghost reflection. This involves stacking all the ghost reflections retrieved from all virtual receivers using Equation 3.2:

$$C^T_{b/m} = \sum_{A=1}^{Vr} C^A_{b/m}, \tag{3.6}$$

where, $C^A_{b/m}$ represents the ghost reflection for each virtual receiver. This calculation results in a single trace representing the ghost reflection inside the reservoir for both the baseline survey and the monitoring survey ($C^T_{b/m}$).

We apply the same procedure to calculate the time difference (CC^T_m) and the relative time difference (RT^T_m) using the stacked ghost reflection:

$$CC^T_m = |argmax(FT^{-1}(C^{T*}_b(x_A,\omega)C^T_m(x_A,\omega)))|, \tag{3.7}$$

$$RT^T_m = \frac{|CC^T_m - \Delta T_m|}{\Delta T_m}. \tag{3.8}$$

3.3. RESULTS

In this section, we first show the retrieval of ghost reflections from SI for the baseline survey, utilising the Groningen subsurface model. We then proceed to demonstrate the retrieved ghost reflections for the monitoring surveys, with a specific emphasis on analysing the time differences between the baseline survey and the monitoring surveys. Furthermore, we delve deeper into understanding the influence of source and receiver configurations on successfully retrieving high-resolution ghost reflections.

3.3.1. NUMERICALLY MODELLED DATA

Our objective is to retrieve and analyse ghost reflections from inside the Groningen reservoir to monitor changes occurring within it. One of the key factors contributing to these changes is the pressure depletion resulting from gas extraction. To investigate this phenomenon, we conducted a laboratory experiment to measure velocity variations caused by pressure depletion.

To simulate the conditions of the Groningen gas reservoir, we utilise a Red Felser sandstone cylindrical sample, known as an analogue to the Rotliegend sandstones found in the reservoir. The sample has a porosity of 19% and dimensions of 30 mm in diameter and 60 mm in height. Our experimental setup involves active-source ultrasonic transmission measurements, employing two S-wave transducers integrated into the pistons of the loading system. The transducers are positioned such that one serves as the source at the top while the other acts as the receiver at the bottom. By utilising a centre frequency of 1 MHz, we determine the S-wave velocities (a schematic illustration of the experimental setup can be found in Veltmeijer et al. (2022) and Naderloo et al. (2023)). During the experiment, we systematically reduce the pore pressure from 30 MPa to 1 MPa, employing decrement steps of 5-10 bar. Throughout this process, the axial stress (65 MPa) and confining pressure (33 MPa) are kept constant to investigate the specific impact of pore-pressure depletion. These specific values were adopted from Spiers et al. (2017) and represent the stress regime of the Groningen reservoir. Figure 3.2 shows the measured velocity changes due to the pore pressure changes.

We use the measured S-wave velocities for the pore pressures of 30, 20, 10, 8 and 5 MPa (the blue circles in Figure 3.2) for the Rotliegend reservoir in the Groningen subsurface model (derived from the Groningen Velocity Model 2017 by Nederlandse Aardolie Maatschappij (NAM, 2017), which is one of the best-known realistic velocity models for the Groningen subsurface). We consider a subsurface model with a pore pressure of 8 MPa as the baseline survey and the others as monitoring surveys. Our choice of 8 MPa for the baseline survey is dictated by the current pore pressure in the reservoir (NAM, 2021).

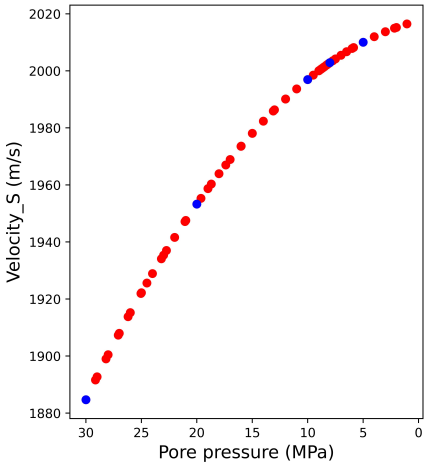

Figure 3.2: Measured velocity in the laboratory experiment as a function of changes in pore pressure. The blue circles indicate the chosen pore pressures for the baseline and monitoring surveys.

Using the subsurface model, we generate a seismic reflection dataset employing a finite-difference modelling code (Thorbecke and Draganov, 2011) in a scalar mode. We use S-wave velocities in our numerical modelling because, in a 2D field survey, it is possi-

ble to use S-wave sources and horizontal-component receivers oriented in the direction perpendicular to the line. As a result, the recorded horizontal S-waves are completely decoupled from the P- and vertical S-waves by assuming that the medium is invariant in the crossline direction.

Figure 3.3 shows the location of the Groningen region and the S-wave velocity model for the baseline survey. The Groningen reservoir is located at a depth of around 3000 m, and we consider a constant thickness of 267 m in our modelling to be able to interpret the result as monitoring velocity changes inside the reservoir and to avoid the velocity/thickness ambiguity. Additionally, in order to avoid using an excessively small grid size in our finite-difference modelling, we have taken into account a higher velocity for the North Sea formation (the top layer in the velocity model). This adjustment aims to reduce computational costs associated with the modelling process without having any conceptual influence on the results. The fixed receiver positions for our numerical modelling range from 3000 m to 7000 m (the blue triangles in Figure 3.3b); the sources are placed from 2001.25 m to 8001.25 m at the surface (the red stars in Figure 3.3b). The receivers and sources are regularly sampled with 1.25 m (the grid length) and 40 m spacing, respectively. We use a Ricker wavelet with a peak frequency of 20 Hz as a source wavelet. We also use an absorbing boundary at the surface to remove free-surface multiples in the numerically modelled data to better retrieve ghost reflections (Shirmohammadi et al., 2024).

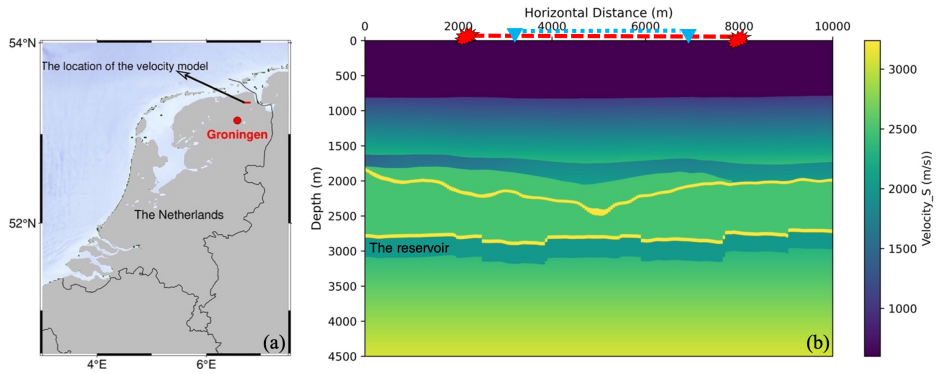

Figure 3.3: a) The location of the velocity model, (b) The Groningen velocity model and the geometry of the active sources (red stars) and the receivers (blue triangles) at the surface used in our numerical modelling.

Figure 3.4a shows the modelled common-source gather for a source at 5001.25 m for the subsurface model for 8 MPa pore pressure as a baseline survey. In this shot gather, we can see primary reflections from subsurface layers, including the reflections from the top and bottom of the reservoir (the blue and the purple arrows, respectively). We apply SI by AC by turning active sources into virtual receivers, which means we correlate each trace with itself for each common-source gather, and then we stack all correlated gathers along the receivers to retrieve a zero-offset section. Figure 3.4b shows the results of SI by AC while all events in the common-source gathers are used. The result contains several retrieved ghost reflections from inside different layers of the subsurface model. They

result from the correlation of all primaries and internal multiples in the source gathers. Note that all the events in the result of SI in our numerical modelling are ghost events because we used an absorbing boundary at the surface, and there are no surface-related multiples in the source gathers to create pseudo-physical reflections.

As indicated in Figure 3.4b by the magenta arrows, it becomes challenging to distinguish specific ghost reflections from target layers, such as the ghost reflection from inside the reservoir. To improve the retrieval of ghost reflections propagating specifically inside the reservoir, which is our target layer, it is essential to correlate only the reflection from the top and the bottom of the target layer (Equation 3.2). Therefore, we mute by manual picking all undesired events arriving earlier than the reflection from the top of the reservoir and later than the reflection from the bottom of the reservoir before applying SI by AC. In this condition, we only correlate the primary reflection from the top and the bottom of the reservoir (the blue and the purple arrows, respectively, in Figure 3.4a). As a result, we only retrieve the ghost reflection from inside the reservoir.

Figure 3.4c shows the retrieved result for the muted common-source gathers. The event indicated by the red arrow is the ghost reflection from inside the reservoir, which represents energy that propagates only inside the reservoir. The arrival time of the retrieved ghost reflection (0.27 s in Figure 3.4c) corresponds to the travel time of a reflection inside the reservoir, which is equivalent to a reflection that would be recorded at a virtual ghost receiver placed directly at the top of the reservoir from a virtual ghost source at the same position. (Because such direct recordings are impossible with our acquisition geometry, we call them virtual ghost receiver and virtual ghost source, respectively.) We aim to use the retrieved ghost reflections from inside the Groningen reservoir for monitoring. So, we continue with retrieving ghost reflections for monitoring surveys.

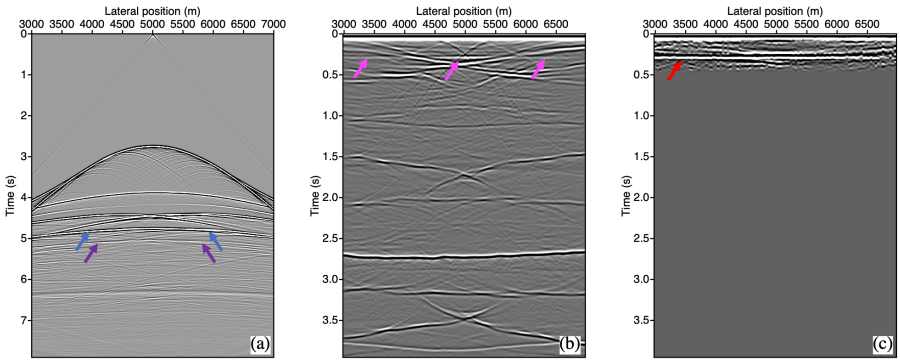

Figure 3.4: (a) Common-source gather for an active shot at 5001.25 m. (b) The result of SI by AC when all events are used. (c) Same as (b) but for muted shot gathers. The blue and purple arrows indicate the reflections from the top and the bottom of the reservoir, the magenta arrows indicate the possible ghost reflections from inside the Rotliegend reservoir or other ghost reflections, and the red arrow shows the specific ghost reflection from inside the Rotliegend reservoir.

3.3.2. TIME-LAPSE INVESTIGATION USING GHOST REFLECTIONS

For retrieving ghost reflections from the subsurface models for the monitoring surveys for pore pressures of 30, 20, 10, and 5 MPa, we apply a procedure similar to the one for the base survey. To better compare the results of SI, we extract one trace for a virtual receiver at 5001.25 m from the retrieved zero-offset sections for all different pore pressures (Figure 3.5a) and a virtual receiver at 3801.25 (Figure 3.5b) and the stacked ghost reflection using all virtual receivers using Equation 3.6 (Figure 3.5c).

As we can see in Figure 3.5, the retrieved ghost reflections show changes in time and amplitude for the different pore pressures. Our goal is to assess the time difference between the ghost reflections retrieved in the baseline survey and those in the monitoring surveys. It is challenging to extract the exact time differences in the ghost reflections by comparing them, as depicted in Figure 3.5. To address this challenge, we employ a correlation technique between the ghost reflections obtained from the baseline survey and the corresponding ghost reflections from the monitoring surveys. By applying this correlation operator across all virtual receivers, we can determine the time at which the correlation yields its maximum amplitude (Equation 3.3). This time value directly corresponds to the time difference between the ghost reflections in the base and monitoring surveys. Note that these ghost reflections exclusively propagate within the reservoir, and, thus, the extracted time difference can be interpreted as a direct measure of the time difference within the reservoir itself.

In Figure 3.6(a-d), we present as the blue areas the retrieved time differences between the ghost reflections from the baseline survey and the monitoring survey for different pore pressure conditions: 30 MPa (Figure 3.6a), 20 MPa (Figure 3.6b), 10 MPa (Figure 3.6c), and 5 MPa (Figure 3.6d), considering all virtual receivers denoted by the blue highlighted region. The thick black line in this figure represents the expected time difference, calculated using Equation 3.4.

As observed in Figures 3.6a and 3.6b, for monitoring surveys for pore pressures of 20 and 30 MPa, the time differences for all virtual receivers are more or less similar to the expected one, especially for those virtual receivers in the middle of the line of the sources. These virtual receivers are characterised by a complete illumination of the actual receivers from both sides. As also illustrated in Figures 3.5a and 3.5b, it becomes evident that the ghost reflections at the virtual receivers positioned in the middle present a better signal-to-noise ratio. So, we further zoom in on the virtual receivers positioned in the middle of the line, as shown in Figure 3.6(e-h), depicting the time differences specifically for this subset of virtual receivers. For the monitoring surveys for pore pressure of 10 and 5 MPa (Figures 3.6c and 3.6d, respectively), the time difference is consistently zero, indicating that the ghost reflections cannot accurately predict time differences in these scenarios.

To increase our ability to estimate time differences between ghost reflections, we employ time series intersampling, which, in this context, involves increasing the number of samples through the use of interpolation (Mikesell et al., 2015). Consequently, we intersample the retrieved ghost reflections before applying the correlation operator for calculating time differences. The time differences derived from the intersampled dataset are depicted in the highlighted orange regions in Figure 3.6. We observe a significant improvement in the time-difference estimation, particularly for pore pressures of 10 MPa

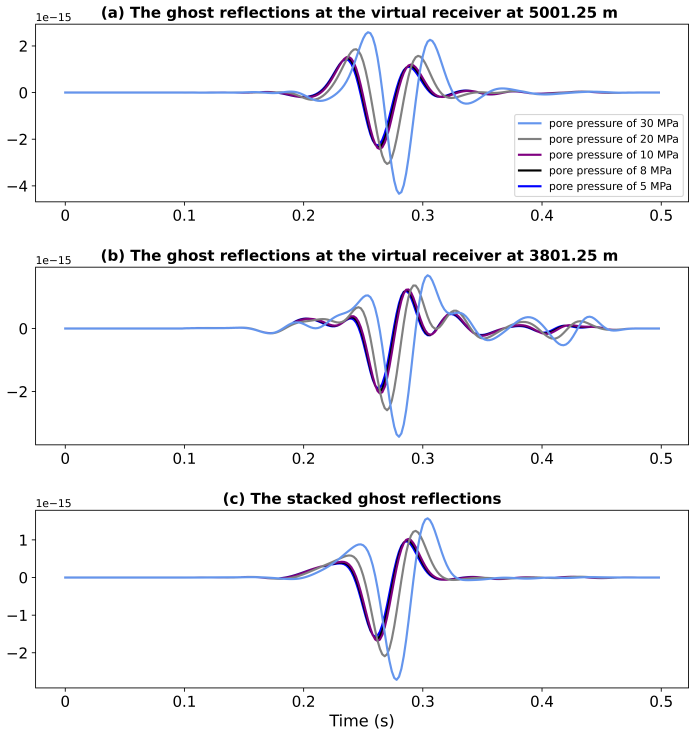

Figure 3.5: (a) Retrieved zero-offset ghost reflections for a virtual receiver at 5001.25 for the baseline survey and the monitoring surveys; (b) same as (a) but for a virtual receiver at 3801.25 m. (c) Results of stacking the retrieved ghost reflections over virtual receivers.

and 5 MPa (Figures 3.6c, 3.6d, 3.6g, and 3.6h), which were previously challenging to predict using the original dataset. Furthermore, there is still a noticeable enhancement in the time-difference estimation for pore pressures of 30 MPa and 20 MPa (Figures 3.6a, 3.6b, 3.6e, and 3.6f).

As mentioned in the methodology section, we validate our retrieved time differences by computing the average relative time difference for the monitoring surveys using Equation 3.5. Figure 3.7 shows the average relative time differences using all virtual receivers (Figure 3.7a) and specifically using selected virtual receivers positioned in the middle of the line (Figure 3.7b) derived from both the original dataset (the blue circles) and the intersampled dataset (the purple triangles). Note that we have chosen to show the average relative time difference due to our assumption of no thickness change or lateral velocity change in our subsurface model. This procedure simplifies the validation process of our technique.

As we can see in Figure 3.7, the relative time differences for pore pressures of 5 MPa and 10 MPa are both equal to 1 (the blue circles for the pore pressure of 5 MPa and 10 MPa). This indicates we are unable to estimate time differences for these monitoring sur-

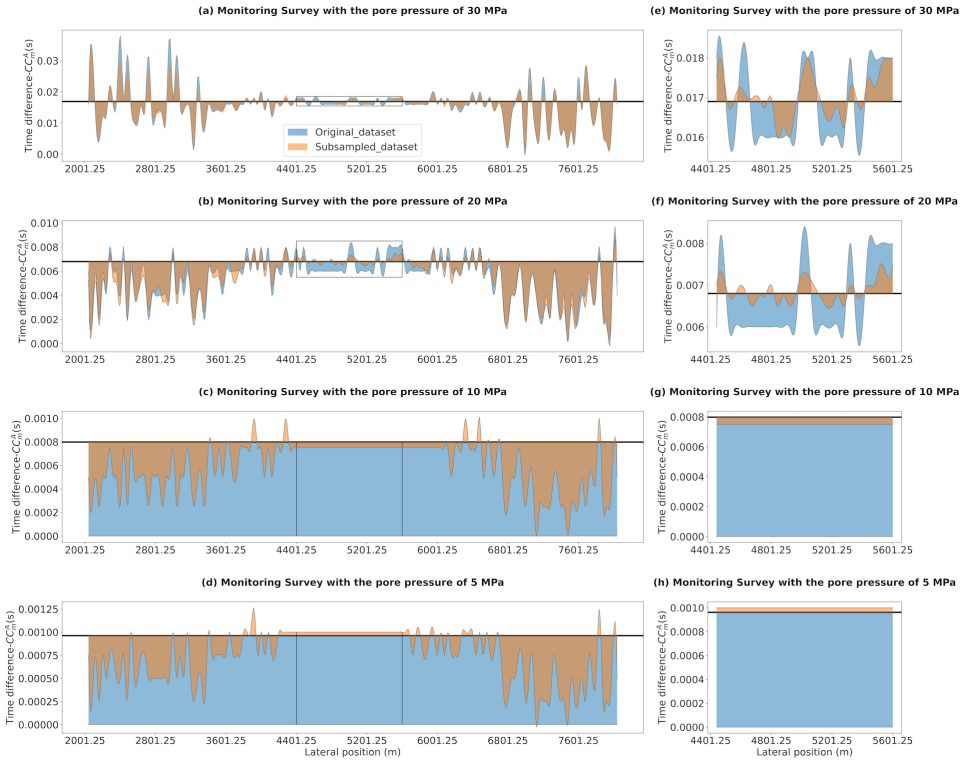

Figure 3.6: The retrieved time differences in the reservoir using ghost reflections for the monitoring surveys with pore pressure of (a) 30 MPa, (b) 20 MPa, (c) 10 MPa, and (d) 5 MPa for all virtual receivers. (e), (f), (g), and (h) Zoomed in results from inside the black rectangles in (a), (b), (c), and (d), respectively. The blue highlighted area shows the time difference using the original dataset, and the orange one shows the time difference using the intersampled dataset. The horizontal black lines show the calculated time differences.

veys, given the very small changes inside the reservoir using the original dataset without intersampling. Contrary to this, after the application of intersampling, we can efficiently estimate time differences for these two pore pressures, approaching an average relative time difference close to zero. Conversely, for pore pressures of 20 MPa and 30 MPa, the relative time differences for both the original dataset and the intersampled dataset remain relatively consistent and close to zero.

Figure 3.7b, illustrating the selected virtual receivers, exhibits a similar trend to Figure 3.7a for both the original dataset and the intersampled dataset (the blue circles and purple triangles, respectively). However, the relative time difference for the selected virtual receivers approaches zero, signifying that they provide better estimates compared to using all virtual receivers. This improvement in results for the virtual receivers positioned in the middle of the source line is because of the complete illumination from both sides.

To mitigate the influence of virtual receivers positioned at the sides, we apply stacking as introduced in Equation 3.6. The stacked ghost reflections are shown in Figure 3.5c.

Subsequently, we calculate the relative time difference for both the original dataset (the black plus symbols in Figure 3.7) and the intersampled (the grey plus symbols) using Equation 3.7. Comparing these relative time differences, it becomes evident that the stacked dataset yields superior results when all virtual receivers are utilised, while there is no significant distinction between the relative time difference of stacked ghost reflections and the average of the time differences of the individual virtual receivers when we use the selected virtual receivers. This implies that stacking effectively mitigates the influence of the virtual receivers positioned at the sides. In conclusion, the intersampled dataset yields the most favourable outcome for all monitoring surveys (the grey plus symbols in Figure 3.7). Consequently, we opt to present the retrieved time differences from the stacked intersampled dataset as the final time difference for different pore pressure conditions of our monitoring surveys.

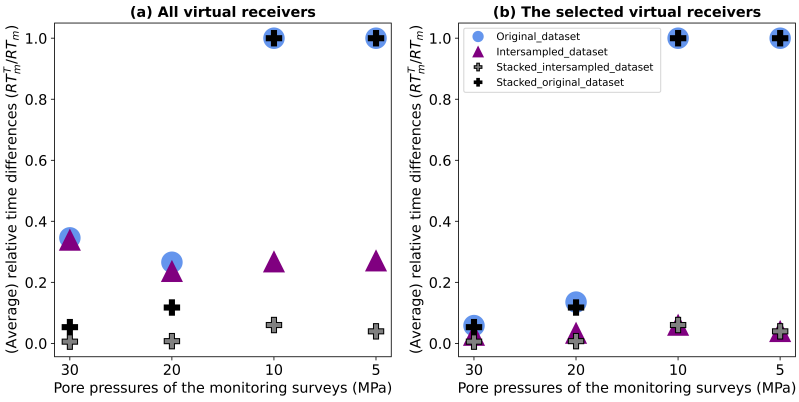

Figure 3.7: The average relative time differences for the monitoring surveys (a) using all virtual receivers and (b) specifically for selected virtual receivers positioned in the middle of the line derived from the original dataset (the blue circles) and the intersampled dataset (the purple triangles). The plus symbols show the relative time differences using the stacked ghost reflections from the original dataset (black) and the intersampled dataset (grey).

Figure 3.8 presents the time difference between the baseline and monitoring surveys, employing the stacked intersampled ghost reflections. In this context, the baseline survey corresponds to a pore pressure of 8 MPa, while the monitoring survey at 5 MPa can be interpreted as representing pore pressure depletion within the reservoir. On the other hand, the monitoring surveys at pore pressures of 10, 20, and 30 MPa can be viewed as examples of an injection mode within the reservoir. In both scenarios, we observe that the time difference remains detectable, even in the presence of small changes within the reservoir. It is worth noting that, as depicted in Figure 3.2, we observe velocity variations in the reservoir ranging from 0.3% to 6%, and the retrieved time differences depicted in Figure 3.8 exclusively reflect changes inside the reservoir that correspond to these velocity variations inside the reservoir.

To recap the procedure for time-lapse monitoring using ghost reflections, we initially apply SI by AC using Equation 3.2. Then, we apply intersampling to the retrieved ghost

reflections, and we extract the time differences between the monitoring survey and the baseline survey using the correlation operator in Equation 3.3 for each individual virtual source, same as shown in Figure 3.6. Note that stacking and averaging are only used to simplify the validation of our technique (in Figures 3.7 and 3.8), which is allowed due to the constant velocity and uniform thickness within the target layer. However, it can be applied to models with homogeneous changes within the target layers or when utilising very localized receivers, assuming that there is no lateral velocity change inside the target layer.

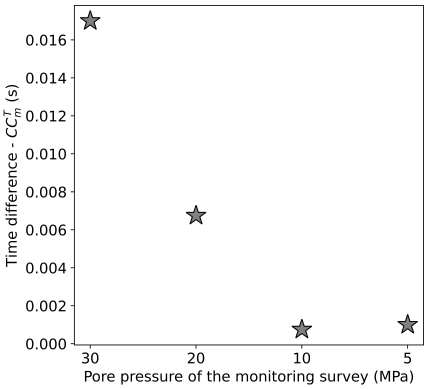

Figure 3.8: The time differences between the monitoring surveys (pore pressure of 30, 20, 10 and 5 MPa) and the baseline survey (pore pressure of 8 MPa) using the stacked ghost reflections.

3.3.3. SOURCES AND RECEIVERS CONFIGURATION

In the previous subsections, we looked at the result of SI by AC, where we turned actual sources into virtual receivers using SI. We opted for this approach because the spacing between the receivers was 1.25 m, which is shorter than the spacing between the sources. In this subsection, we will show the result of SI by turning receivers into virtual sources. Additionally, we demonstrate the effect of the source and receiver configuration, such as the number of sources and receivers, the spacing between them, and their geometry, in the retrieval of ghost reflections. This will offer valuable insights into the future practical applications of ghost reflections using field datasets. Note that in this subsection, we only look at the virtual zero-offset section for the baseline survey.

Figure 3.9a shows the zoomed-in virtual zero-offset section resulting from SI by AC from Figure 3.4c when turning the active sources into virtual receivers, which means we stack the correlated responses over all receivers with 1.25 m spacing. Figure 3.9b shows the obtained virtual zero-offset section by turning receivers into virtual sources. In this situation, we stack the correlated responses for each receiver over all active sources with 40 m spacing. Table 3.1 shows all information regarding the spacing between virtual sources and receivers and spacing between stacked traces for the virtual zero-offset sections in Figure 3.9.

Comparing Figure 3.9a with Figure 3.9b, we can see we have a similar ghost reflections despite different numbers of traces in the zero-offset sections and different spacing

in the responses used for stacking in SI. This is an important finding, especially for the applications of ghost reflections using seismic field data when the number of receivers and sources is different. To better understand the effect of optimal spacing and the number of traces, we reduce the number of active sources and then apply SI by AC.

Figure 3.9c shows the virtual zero-offset section when we use half of the sources as virtual receivers but the same number of receivers for stacking as in Figure 3.9a. By comparing Figure 3.9c with Figure 3.9a, we can see that retrieved ghost reflections using shorter spacing between responses for stacking allow high-resolution interpretation of the target, even with the limited number of virtual receivers. Note that the optimal spacing is determined by half of the dominant wavelength. Figure 3.9d shows a virtual zero-offset section using the same dataset as in Figure 3.9c but now after turning the receivers into virtual sources. Comparing this result with the one in Figure 3.9b, we can see that the retrieved ghost reflections allow interpretability with lower resolution compared to Figure 3.9b, but we can still observe the desired ghost reflection. This means that if we have sub-optimal spacing between traces for stacking, it is necessary to have sufficient virtual sources.

Figure 3.9e shows the virtual zero-offset section for virtual receivers retrieved using receivers ranging from 3000 m to 7000 m with spacing of 40 m and sources from 2001.25 m to 8001.25 m with spacing of 40 m. It is evident that the interpretation resolution of the ghost reflections is lowered compared to the one observed in Figure 3.9a, particularly for virtual receivers at lateral distances before 4000 m and after 6000 m. However, for virtual receivers located in the central interval around 5000 m, we achieve the required interpretation resolution. This difference can be attributed to the fact that we utilise for stacking receivers ranging from 3000 to 7000 m, ensuring complete illumination from both sides of the virtual receivers (i.e., the sources to be turned into virtual receivers). It is crucial to note that, for the retrieval of pseudo-physical or ghost reflections, only a limited number of points fall into the stationary-phase region for a laterally homogenous medium and thus significantly contribute to the Green's function estimate. Consequently, for virtual receivers outside the receiver arrays, there is a higher chance for a limited number of receivers within the stationary-phase region and incomplete illumination.

Figure 3.9f shows the virtual zero-offset section for virtual sources. We used sources from 2001.25 m to 8001.25 m while the receivers are placed from 3000 m to 7000 m with the same 40 m spacing. Comparing this result to the one in Figure 3.9b, we can see that we have achieved a comparable resolution, but due to the courser distance between the virtual sources, the section now appears as if spatially low-pass-filtered.

In summary, for retrieving high-resolution ghost reflections, optimal spacing between sources or receivers (at least one of them), with at least two samples per dominant wavelength and utilising an inline array with uniformly distributed sources or receivers are required.

Table 3.1: Information about the source and receiver configuration used for retrieving the ghost reflection section in Figure 3.9.

Panel	Spacing between virtual sources or receivers (m)	Spacing between traces used for stacking in SI (m)
a	40	1.25
b	1.25	40
c	80	1.25
d	1.25	80
e	40	40
f	40	40

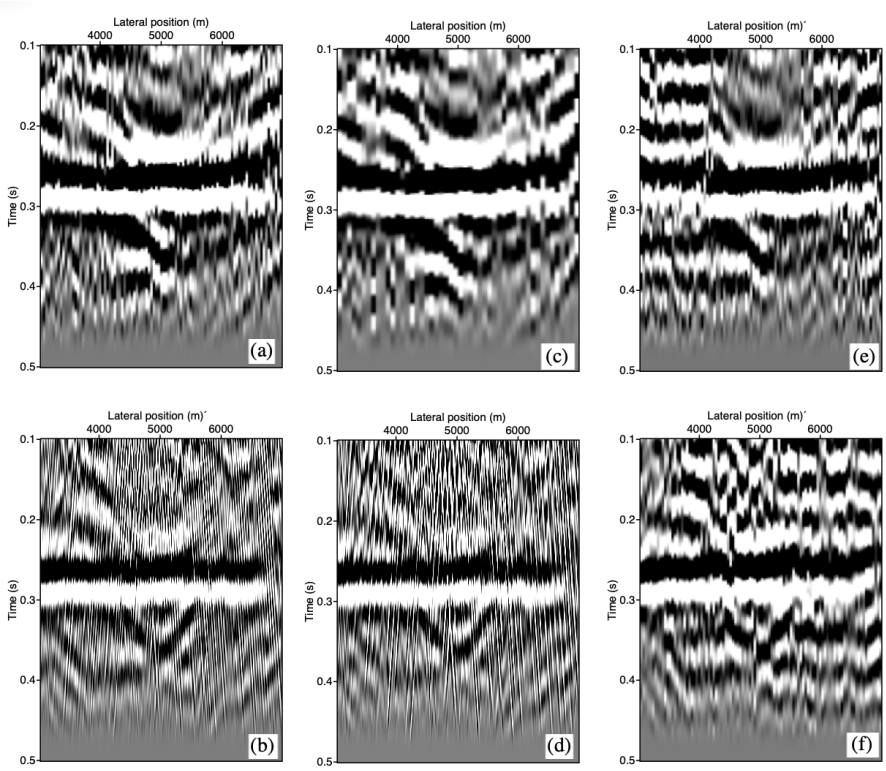

Figure 3.9: The result of SI by AC (a, c, and e) after turning sources into virtual receivers and (b, d, and f) after turning receivers into virtual sources for different spacing between the virtual sources and receivers and different spacing between traces used for summation in SI, see Table 3.1 for exact numbers.

3.4. DISCUSSION

We showed that ghost reflections are retrieved from SI by AC by using two primaries from two different depth levels from active sources and receivers at the surface. Notably, ghost reflections exhibit sensitivity exclusively to changes occurring within the target layer and remain kinematically unaffected by the overburden and underburden layers. This study provides further support for the existing studies regarding the use of ghost reflections in monitoring CO_2 reservoirs through numerical modelling and laboratory experiments (Draganov et al., 2012), as well as in monitoring and characterising the shallow subsurface using numerical modelling and a field dataset (Shirmohammadi et al., 2024).

Although the results indicate that the application of ghost reflections for monitoring subsurface changes could be very practical, specifically for monitoring pore-pressure changes within the Groningen reservoir, several points require a more in-depth discussion, especially for the future application of this technique across various subsurface models or with the utilisation of field datasets.

First, our findings indicate that the ghost reflections exhibit sensitivity exclusively to velocity changes inside the reservoir due to pore-pressure changes. We showed that even small changes occurring within the reservoir can be detected, as ghost reflections are similar to isolated reflections, propagating only within the reservoir. To quantify the time differences between the baseline survey and the monitoring surveys, we employed the correlation operator between the ghost reflections retrieved from SI by AC. We used intersampling before the correlation operator to detect small differences. Furthermore, as depicted in Figure 3.5, it is evident that the maximum amplitudes of retrieved ghost reflections vary between the baseline survey and the monitoring surveys. The amplitudes can be relatively correct in SI; however, when specific conditions are not met, amplitude errors can be significant (Wapenaar and Fokkema, 2006). Therefore, a more in-depth investigation is required to assess these amplitude variations. We elaborate more on the amplitude of ghost reflections in Chapter 4.

Second, in our numerical-modelling approach, we considered a uniform reservoir thickness to highlight the sensitivity of the ghost reflections to the velocity changes. However, in reality, the ghost reflections will also be sensitive to other types of changes within the reservoir, such as thickness change, density change or a combination of these factors. It is important to note that these changes are not limited to being constant; they can also involve gradient changes, as demonstrated in Chapter 2. In these scenarios, we should use a ghost reflection for each virtual receiver (or source) to investigate the changes, as illustrated in Figure 3.6.

Third, we used ghost reflections propagating exclusively inside the reservoir, which was our target layer. These specific ghost reflections can be retrieved more efficiently by muting undesired reflection arrivals earlier and later than the target arrivals, which requires those events to be clearly interpretable, especially in field data. However, we propose this technique for monitoring applications in which the target layers are already clearly identified from the baseline survey. It is worth mentioning that under certain cases, such as when dealing with a thin target layer, it becomes challenging to accurately separate the reflection from the top and bottom of the target layer before SI. In such cases, the retrieved ghost reflection would represent propagation inside multiple layers, including the thin target layer. Thus, the vertical resolution of our methodology for re-

trieving the ghost reflections relies on the resolution of the reflection dataset as input. Using S-wave surveys increases the vertical resolution compared to P-wave surveys due to the shorter wavelength of the S-waves for the same frequencies. Additionally, thin layers above or below the target layer, such as an anhydrite layer above the reservoir in our subsurface model, make it challenging to separate reflections from the top of the reservoir for far offsets. Nonetheless, this issue is mitigated to some extent through the stacking using the dataset from different offsets in SI (Equations 3.1 and 3.2).

To mitigate the presence of undesirable reflections that could overlap with the target ghost reflections in the result of SI, such as pseudo-physical reflections (i.e., reflections with physical kinematics), we used an absorbing boundary at the surface in our numerical modelling. The pseudo-physical reflections are the result of the correlation between primary reflections and their surface-related multiples. By using an absorbing boundary, we effectively prevented the occurrence of surface-related multiples and surface waves, thereby enhancing the quality of the SI results in numerical modelling. It is thus important to suppress surface waves as in, e.g., Balestrini et al. (2020) and surface-related multiples as in, e.g., Ghose and Goudswaard (2004) prior to applying SI when working with field datasets. These two pre-processing steps would ensure the accuracy and reliability of the SI outcomes by eliminating any potential confusion arising from retrieved pseudo-physical reflections but also interference from surface waves.

Finally, the interpretability resolution of ghost reflections relies not only on the resolution of the input data but also on the source and receiver configuration. We explored two approaches: turning sources into virtual receivers and turning receivers into virtual sources. Determining which approach is more reliable depends on a sufficient number of sources (or receivers) for stacking within the stationary-phase zone, ideally at least two per dominant wavelength. However, if achieving this requirement is not feasible, more virtual sources (or receivers) are required to aid interpretation. It is important to note that the width of the stationary-phase region depends on several factors, including the medium velocity, the dominant frequency of the source signal (Draganov et al., 2012), as well as the thickness and depth of the target layer. For a laterally homogeneous medium, only a certain number of sources positioned in line with the receivers remain stationary, meaning rays from such source positions are nearly parallel and interfere constructively in the summation (Draganov et al., 2012). In the case of other media, determining the exact stationary-phase zone region is challenging. Therefore, it is recommended to maintain optimal spacing between receivers (or sources), which is at least two samples per dominant wavelength, and utilise an inline array with a two-sided uniform distribution of the sources (or receivers) with an extended length for sources (or receivers) on both sides to ensure the retrieval of high-resolution ghost reflections, at least for the virtual receivers (or sources) located in the middle of the array. We elaborate further on this by presenting some examples of correlation gathers used for the results of SI by AC in Figure 3.9 in the supplementary material (section 3.6).

3.5. CONCLUSION

We focused on exploring the practical applicability of ghost reflections in monitoring subsurface activities, specifically in relation to pore-pressure changes, within the gas reservoir in Groningen, the Netherlands. Applying seismic interferometry (SI) to sur-

face reflection data results in the appearance of ghost reflections in the retrieved virtual-source or virtual-receiver gathers. The ghost reflections result primarily from the correlation of primary reflections from different depth levels.

We determined the time differences between the ghost reflection retrieved from a baseline survey and several monitoring surveys using a correlation operator. The monitor surveys represented data after changes in the reservoir pore pressure to 30, 20, 10, and 5 MPa from the value of 8 MPa for the base survey. To detect minor changes effectively, we highlighted the importance of employing intersampled ghost reflections and considering virtual receivers with sources at the surface illuminating from both sides of the line. We demonstrated that the retrieved time differences between the ghost reflections exhibit variations corresponding to velocity changes within the reservoir. Notably, the retrieved ghost reflections are only sensitive to changes occurring in the target layer, effectively eliminating the kinematic influence of the overburden and underburden.

We also investigated the factors that contribute to obtaining ghost-reflection images with high interpretability resolution. We found that the geometry of the sources and receivers, the number of virtual sources and receivers, as well as the spacing between traces used for stacking for SI all play significant roles in ensuring clear ghost-reflection images. Additionally, by muting undesired reflection arrivals earlier and later than the target arrivals to correlate, we were able to enhance the clarity and robustness of the retrieved ghost reflections, which is crucial when working with field datasets. The implications of our findings are notable, as ghost reflections can serve as valuable indicators for monitoring both near-surface structures and deeper formations, such as fluid reservoirs or storage sites for H_2 and CO_2.

3.6. SUPPLEMENTARY MATERIAL

3.6.1. CORRELATION PANELS

As discussed in Section 3.3.3, the interpretability resolution of the ghost reflections relies on the source and receiver configuration, including the spacing between the traces utilised for stacking, the number of virtual receivers (or sources), and the geometry. This increases our chance of ensuring the retrieval of high-resolution ghost reflections by correlating more traces in the stationary-phase region. To elaborate more on these conditions, below, we present some correlation gathers for different settings in Figure 3.9.

Figure 3.10 shows the correlation gathers for different virtual receivers used for the result of SI shown in Figure 3.9a. Because the medium in this case is laterally invariant along the surface, the width of the stationary-phase region is the same for all virtual receivers. Note that we stack all traces in each correlation gather to create a response at each virtual receiver in the result of SI by AC. As can be seen in Figure 3.10, there are more traces with a stationary-phase for virtual receivers in the middle of the array (Figures 3.10c - 3.10e). For the virtual receivers on the sides of the line, such as Figures 3.10b and 3.10f, the number of traces within the stationary-phase region decreases. Nevertheless, a high-resolution ghost reflection is retrieved, as shown in Figure 3.9a, due to the constructive contribution of a larger number of traces for stacking in the stationary-phase region. Note that for this setting, in each correlation gather, we stack all receivers from 3000 m to 7000 m with 1.25 m spacing. In contrast, when fewer traces in correla-

tion gathers are used (receivers from 3000 to 7000 m with 40 m spacing), as shown in Figure 3.11, a high-resolution ghost reflection is retrieved only for virtual receivers in the middle, as shown in Figure 3.9e.

Figure 3.12 shows the correlation gathers for all virtual sources used for the result of SI by AC in Figure 3.9b. In these correlation gathers, the spacing between traces in each correlation gather is the same as Figure 3.11, but for a different geometry: the extent of the sources, i.e., the traces over which we stack, is from 2000-8000 m with 40 m spacing. Because of this larger extent and the higher number of virtual sources, when correlation gathers are stacked in Figure 3.12 for all sources, a high-resolution ghost reflection is still obtained, as demonstrated in Figure 3.9b. Reducing the number of virtual sources (from 3000-7000 m with 40 m spacing) results, as expected, in lower interpretation resolution of ghost reflections as illustrated in Figure 3.9f.

In summary, if traces are stacked inside the stationary-phase region, the quality of ghost reflections will be increased. However, determining the exact width and place of the stationary-phase region is challenging as shown in Mehta et al. (2008). Therefore, we recommend maintaining optimal spacing between either receivers or sources with at least two samples per the dominant wavelength at their position (in our case the surface) and utilising an inline array with a two-sided uniform distribution of the sources (or receivers) with an extended length for sources (or receivers) on both sides. It is also advisable to examine the correlation gathers before stacking (Mehta et al., 2008) for possibly applying techniques such as singular value decomposition (SVD) to the correlated gathers before stacking (Melo et al., 2013) to suppress non-stationary signals.

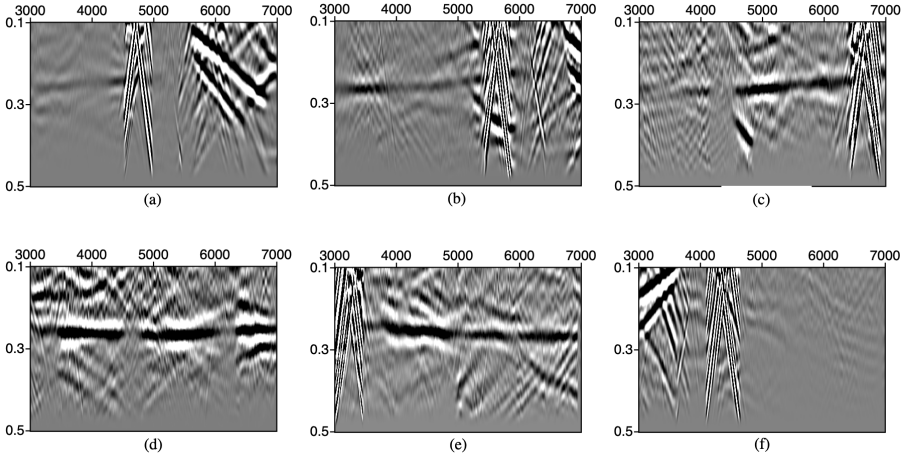

Figure 3.10: The correlation gathers for different virtual receivers used to obtain the result of SI by AC in Figure 3.9a. The lateral position of the virtual receivers is (a) 2001.25 m, (b) 3001.25 m, (c) 4001.25 m, (d) 5001.25 m, (e) 6001.25 m , and (f) 7001.25 m.

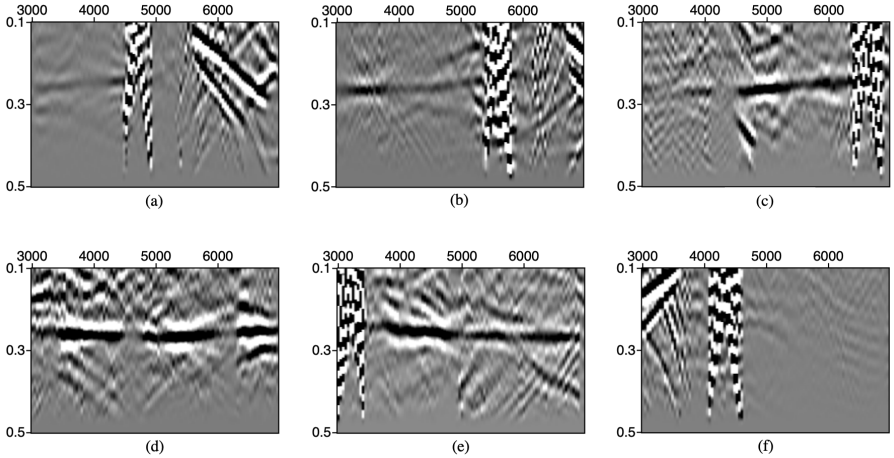

Figure 3.11: The correlation gathers for different virtual receivers used to obtain the result of SI by AC in Figure 3.9e. The lateral position of the virtual receivers is (a) 2001.25 m, (b) 3001.25 m, (c) 4001.25 m, (d) 5001.25 m, (e) 6001.25 m , and (f) 7001.25 m.

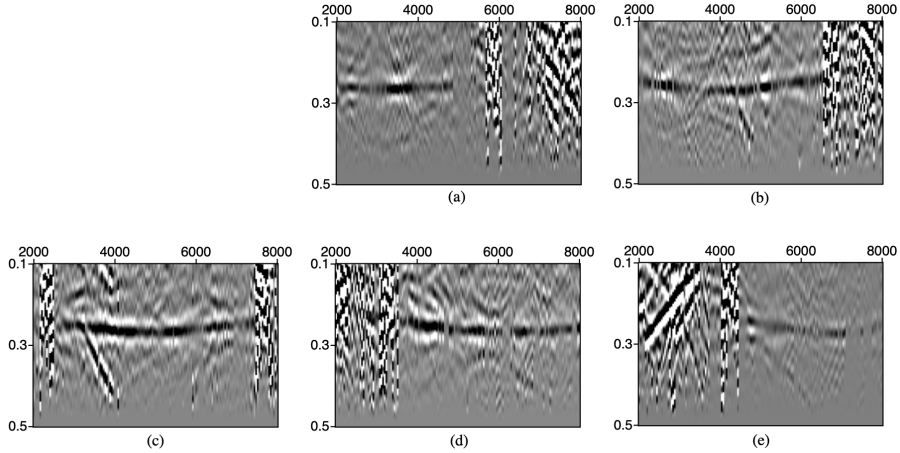

Figure 3.12: The correlation gathers for different virtual sources used to obtain the result of SI by AC in Figure 3.9b. The lateral position of the virtual sources is (a) 3000 m, (b) 4000 m, (c) 5000 m, (d) 6000 m, and (e) 7000 m.

3.7. DATA AVAILABILITY

The data and codes underlying this chapter are available in repository 4TU.ResearchData at https://doi.org/10.4121/f6a4ad46-c1aa-4c09-a0a9-3a3558763d59.

REFERENCES

Balestrini, F., Draganov, D., Malehmir, A., Marsden, P., & Ghose, R. (2020). Improved target illumination at Ludvika mines of Sweden through seismic-interferometric surface-wave suppression. *Geophysical Prospecting, 68*(1), 200–213. https://doi.org/10.1111/1365-2478.12890

Bourne, S. J., Oates, S. J., Van Elk, J., & Doornhof, D. (2014). A seismological model for earthquakes induced by fluid extraction from a subsurface reservoir. *Journal of Geophysical Research: Solid Earth, 119*(12), 8991–9015. https://doi.org/10.1002/2014JB011663

Brenguier, F., Courbis, R., Mordret, A., Campman, X., Boué, P., Chmiel, M., Takano, T., Lecocq, T., Van der Veen, W., Postif, S., & Hollis, D. (2020). Noise-based ballistic wave passive seismic monitoring. Part 1: Body waves. *Geophysical Journal International, 221*(1), 683–691. https://doi.org/10.1093/gji/ggz440

Draganov, D., Heller, K., & Ghose, R. (2012). Monitoring CO2 storage using ghost reflections retrieved from seismic interferometry. *International Journal of Greenhouse Gas Control, 11*(SUPPL), S35–S46. https://doi.org/10.1016/j.ijggc.2012.07.026

Draganov, D., Ghose, R., Ruigrok, E., Thorbecke, J., & Wapenaar, K. (2010). Seismic interferometry, intrinsic losses and Q-estimation. *Geophysical Prospecting, 58*(3), 361–373. https://doi.org/10.1111/j.1365-2478.2009.00828.x

Ghose, R., & Goudswaard, J. (2004). Integrating S-wave seismic-reflection data and cone-penetration-test data using a multiangle multiscale approach. *Geophysics, 69*(2), 440–459. https://doi.org/10.1190/1.1707064

Halliday, D., Curtis, A., Robertsson, J. O., & van Manen, D. J. (2007). Interferometric surface-wave isolation and removal. *Geophysics, 72*(5), A69–A73. https://doi.org/10.1190/1.2761967

Hatchell, P. J., & Bourne, S. J. (2005). Measuring reservoir compaction using time-lapse timeshifts. *Society of Exploration Geophysicists - 75th SEG International Exposition and Annual Meeting, SEG 2005*. https://doi.org/10.1190/1.2148230

King, S., & Curtis, A. (2012). Suppressing nonphysical reflections in Green's function estimates using source-receiver interferometry. *Geophysics, 77*(1), Q15–Q25. https://doi.org/10.1190/geo2011-0300.1

Landrø, M. (2001). Discrimination between pressure and fluid saturation changes from time-lapse seismic data. *Geophysics, 66*(3), 836–844. https://doi.org/10.1190/1.1444973

Löer, K., Meles, G. A., Curtis, A., & Vasconcelos, I. (2013). Diffracted and pseudo-physical waves from spatially limited arrays using source-receiver interferometry (SRI). *Geophysical Journal International, 196*(2), 1043–1059. https://doi.org/10.1093/gji/ggt435

Lumley, D. E. (2001). Time-lapse seismic reservoir monitoring. *Geophysics, 66*(1), 50–53. https://doi.org/10.1190/1.1444921

Ma, X., Kirichek, A., Heller, K., & Draganov, D. (2022). Estimating P- and S-Wave velocities in fluid mud using seismic interferometry. *Frontiers in Earth Science, 10*, 1–11. https://doi.org/10.3389/feart.2022.806721

MacBeth, C., Amini, H., & Izadian, S. (2020). Review Paper: Methods of measurement for 4D seismic post-stack time shifts. *Geophysical Prospecting, 68*(9), 2637–2664. https://doi.org/10.1111/1365-2478.13022

Mehta, K., Snieder, R., Calvert, R., & Sheiman, J. (2008). Acquisition geometry requirements for generating virtual-source data. *The Leading Edge, 27*(5), 620–629. https://doi.org/10.1190/1.2919580

Melo, G., Malcolm, A., Mikesell, D., & van Wijk, K. (2013). Using SVD for improved interferometric Green's function retrieval. *Geophysical Journal International, 194*(3), 1596–1612. https://doi.org/10.1093/gji/ggt172

Mikesell, T. D., Malcolm, A. E., Yang, D., & Haney, M. M. (2015). A comparison of methods to estimate seismic phase delays: Numerical examples for coda wave interferometry. *Geophysical Journal International, 202*(1), 347–360. https://doi.org/10.1093/gji/ggv138

Muntendam-Bos, A. G., Hoedeman, G., Polychronopoulou, K., Draganov, D., Weemstra, C., van der Zee, W., Bakker, R. R., & Roest, H. (2022). An overview of induced seismicity in the Netherlands. *Geologie en Mijnbouw/Netherlands Journal of Geosciences, 101*(2), 1–20. https://doi.org/10.1017/njg.2021.14

Naderloo, M., Ramesh Kumar, K., Hernandez, E., Hajibeygi, H., & Barnhoorn, A. (2023). Experimental and numerical investigation of sandstone deformation under cycling loading relevant for underground energy storage. *Journal of Energy Storage, 64*, 107–198. https://doi.org/10.1016/j.est.2023.107198

NAM. (2017). *Groningen velocity model 2017- groningen full elastic velocity model* (tech. rep.). Nederlandse Aardolie Maatschappij BV. https://doi.org/https://www.nam.nl/over-nam/onderzoeksrapporten

NAM. (2021). *Reservoir pressure and subsidence groningen field update for production profile gts -raming 2021* (tech. rep.). Nederlandse Aardolie Maatschappij BV. https://doi.org/https://www.nam.nl/over-nam/onderzoeksrapporten

Roach, L. A., White, D. J., & Roberts, B. (2015). Assessment of 4D seismic repeatability and CO2 detection limits using a sparse permanent land array at the Aquistore CO2 storage site. *Geophysics, 80*(2), WA1–WA13. https://doi.org/10.1190/GEO2014-0201.1

Schuster, G. T. (2009). *Seismic Interferometry*. Cambridge University Press. https://doi.org/10.1017/CBO9780511581557

Shirmohammadi, F., Draganov, D., & Ghose, R. (2024). The utilization of ghost reflections retrieved by seismic interferometry for layer-specific characterization of the shallow subsurface. *Near Surface Geophysics, 22*, 92–105. https://doi.org/https://doi.org/10.1002/nsg.12275

Snieder, R., Wapenaar, K., & Larner, K. (2006). Spurious multiples in seismic interferometry of primaries. *Geophysics, 71*(4), SI111–SI124. https://doi.org/10.1190/1.2211507

Spiers, C. J., Hangx, S. J., & Niemeijer, A. R. (2017). New approaches in experimental research on rock and fault behaviour in the Groningen gas field. *Geologie en Mijn-*

bouw/Netherlands Journal of Geosciences, *96*(5), S55–S69. https://doi.org/10.1017/njg.2017.32

Thorbecke, J. W., & Draganov, D. (2011). Finite-difference modeling experiments for seismic interferometry. *Geophysics*, *76*(6), H1–H18. https://doi.org/10.1190/geo2010-0039.1

Trani, M., Arts, R., Leeuwenburgh, O., & Brouwer, J. (2011). Estimation of changes in saturation and pressure from 4D seismic AVO and time-shift analysis. *Geophysics*, *76*(2), C1–C17. https://doi.org/10.1190/1.3549756

van Eijs, R. M., Mulders, F. M., Nepveu, M., Kenter, C. J., & Scheffers, B. C. (2006). Correlation between hydrocarbon reservoir properties and induced seismicity in the Netherlands. *Engineering Geology*, *84*(3-4), 99–111. https://doi.org/10.1016/j.enggeo.2006.01.002

van IJsseldijk, J., van der Neut, J., Thorbecke, J., & Wapenaar, K. (2023). Extracting small time-lapse traveltime changes in a reservoir using primaries and internal multiples after Marchenko-based target zone isolation. *Geophysics*, *88*(2), R135–R143. https://doi.org/10.1190/geo2022-0227.1

Veltmeijer, A., Naderloo, M., Pluymakers, A., & Barnhoorn, A. (2022). Acoustic monitoring of laboratory induced fault reactivation. *83rd EAGE Conference and Exhibition 2022*, *2*, 1–5. https://doi.org/10.3997/2214-4609.202210269

Wapenaar, K. (2006). Green's function retrieval by cross-correlation in case of one-sided illumination. *Geophysical Research Letters*, *33*(19), L19304. https://doi.org/10.1029/2006GL027747

Wapenaar, K., Draganov, D., Snieder, R., Campman, X., & Verdel, A. (2010). Tutorial on seismic interferometry: Part 1 - Basic principles and applications. *Geophysics*, *75*(5), 75A195–75A209. https://doi.org/10.1190/1.3457445

Wapenaar, K., & Fokkema, J. (2006). Green's function representations for seismic interferometry. *Geophysics*, *71*(4), SI33–SI46. https://doi.org/10.1190/1.2213955

Zhou, W., & Paulssen, H. (2020). Compaction of the Groningen gas reservoir investigated with train noise. *Geophysical Journal International*, *223*(2), 1327–1337. https://doi.org/10.1093/gji/ggaa364

Zhou, W., & Paulssen, H. (2022). Seismic velocity changes in the Groningen reservoir associated with distant drilling. *Scientific Reports*, *12*(1), 17523. https://doi.org/10.1038/s41598-022-22351-5

4

INVESTIGATING THE AMPLITUDE OF GHOST REFLECTIONS FOR RESERVOIR MONITORING

Ghost reflections retrieved from SI propagate within a subsurface layer, containing valuable information about the seismic properties of that specific layer. Our objective in this chapter is to show the feasibility of using the amplitude of ghost reflections to monitor small changes inside the reservoir. We showcase the potential of this technique using numerically modelled data for the Groningen subsurface.

We employ different approaches to retrieve ghost reflections, including SI by AC using muted common-source gathers, SI by AC using separated reflections, seismic interferometry (SI) by auto-correlation (AC) using normalised separated reflections and trace deconvolution. Our investigation shows that the relative amplitude differences between the ghost reflections exhibit changes corresponding to velocity changes within the reservoir. This emphasises the potential of ghost reflections as valuable indicators for monitoring even small changes inside the reservoir.

This Chapter is under preparation for publication.

4.1. INTRODUCTION

Time-lapse analysis involves acquiring and analysing repeated geophysical surveys at a specific site over time. This process helps identify differences in data sets from different periods, which is particularly beneficial for detecting fluid-flow/injection effects and geomechanical changes in subsurface reservoirs. For instance, when oil is produced under water-flooding conditions, oil and water saturation in the reservoir change, resulting in a change in the seismic response of the reservoir. Additionally, pressure changes in the reservoir will lead to changes in seismic velocities (Dimri et al., 2012).

Two approaches are used in the analysis of time-lapse seismic data. The first is amplitude analysis, which studies variations in the amplitudes between different surveys. The second is time-shift analysis, which examines changes in seismic travel times across surveys (Bjørlykke, 2010). In many cases, changes in fluid saturation and pore pressure lead to changes in the acoustic impedance. The combined effect of saturation and pressure results in amplitude changes. Amplitude analysis is more sensitive to repeatability than seismic travel time, as travel time is less affected by variations in positioning, acquisition, or processing (Brown, 1991).

Generally, the expected time-lapse variation in the reservoir is small depending on the reservoir rock, depth of burial, and changes in fluid saturation, pressure, and temperature. Additionally, responses from a complex overburden can interfere with the reservoir responses, creating challenges in accurately identifying small changes within the reservoir. We propose using SI based on ghost reflections to address these challenges. In Chapter 3, we demonstrated how time shifts in ghost reflections can be utilised for reservoir monitoring. In this chapter, we illustrate the possibility of using amplitude changes of the ghost reflections for reservoir monitoring.

We illustrate the potential of SI with data from numerical acoustic modelling using the Groningen subsurface model. The reservoir of the Groningen gas field is located at depths between 2600 m and 3200 m; the total thickness of the Rotliegend in the Groningen field ranges from approximately 100 m to 300 m. The Groningen field is cut by several fault systems, subdividing the field into many fault blocks, and it presents a clear example of induced seismicity by gas production.

We investigate the amplitude of the ghost reflections obtained from surface active-source data using SI by AC. By analysing zero-offset gathers derived from SI by AC, we demonstrate that changes in the velocity of the Groningen reservoir result in clear amplitude variations in the ghost reflections. This offers an additional approach for monitoring the reservoir in addition to observing time shifts. We provide a brief overview of our methodology and then discuss the process of retrieving the amplitude of the ghost reflections. We compare the retrieved amplitude with directly modelled ghost reflections to validate our findings. The results are presented, followed by a discussion and conclusions.

4.2. METHOD

In the context of an active-source reflection seismic survey, where both the sources and receivers are positioned at the surface, one can derive the frequency-domain response $\hat{G}(x_B, x_A, \omega)$ and its complex conjugate at x_B from a virtual source at x_A from the relation

(Halliday et al., 2007):

$$\hat{G}^*(x_B, x_A, \omega) + \hat{G}(x_B, x_A, \omega) \propto \sum_{n=1}^{N} \hat{G}^*(x_A, x_n, \omega)\hat{G}(x_B, x_n, \omega), \tag{4.1}$$

where the right-hand side of the relation is a multiplication of the frequency spectra of two observations at x_A and x_B from surface sources at x_n, the asterisk $(*)$ denotes complex conjugate in the frequency domain, and N represents the number of active sources. If we substitute the response x_A instead of x_B in relation 4.1, the retrieved Green's function is the result of AC of the arrivals at the receiver x_A. In this scenario, x_A acts as a collocated virtual source and receiver, leading to a retrieved trace that represents a zero-offset reflection trace (after an inverse Fourier transformation).

In exploration seismology, many of the theoretical requirements in SI are not met. Firstly, the dipolar sources, which are typically unavailable. Wapenaar (2006) demonstrated that the Green's function can be obtained by a single cross-correlation of monopolar Green's functions under certain approximations. These approximations include assuming that sources are positioned on a circle with a very large radius, allowing energy from a source to leave the boundary almost perpendicularly, and that no energy is reflected back into the medium by scatterers outside of the boundary. Secondly, the medium is often assumed to be lossless despite the attenuation present in the Earth. Thirdly, the theory requires a complete boundary of sources surrounding the two receivers, but practical limitations confine the illuminating sources to locations near or on the Earth's surface. This leads to the retrieval of ghost reflections in the estimates of the Green's function and also amplitude errors.

Ghost reflections are obtained through the correlation of two primary reflections from different depth levels. For instance, the ghost reflection inside the reservoir (indicated by the red arrow in Figure 4.1a) can be retrieved by correlation of the primary reflections from the top and bottom of the reservoir (represented by the green and purple arrows, respectively, in Figure 4.1a). A detailed explanation of the methodology is provided in Chapters 2 and 3.

4.3. RESULTS

We illustrate the potential of using the amplitude of ghost reflections retrieved from SI by AC with data from numerical modelling using the Groningen subsurface model. Table 4.1 lists details of the velocity model utilised in this chapter for the base survey as provided in Kraaijpoel and Dost (2013). To illustrate the potential of ghost reflections for monitoring, we apply a small velocity change in the Rotliegend reservoir by increasing the velocity from 2734 to 3007 m/s. Figure 4.1a shows the subsurface model for the base survey, while Figure 4.1b shows the velocity model for the monitoring survey.

The fixed receiver positions range from 3000 m to 6000 m (the blue triangles in Figure 4.1a), and the sources are placed from 2990 m to 6010 m (the red stars in Figure 4.1a). The receivers and sources are regularly sampled with 10 m and 20 m spacing, respectively. As a source signature, we use a Ricker wavelet with a peak frequency of 20 Hz. We use a finite-difference modelling code (Thorbecke and Draganov, 2011) in an acoustic mode to generate a seismic reflection dataset. We showed in Chapters 2 and 3 that

to enhance the resolution of ghost reflections, it is necessary to apply preprocessing steps, including surface-wave suppression and elimination of surface-related multiples, achieved in our example by using an absorbing boundary at the surface. More details about using numerical modelling for retrieving ghost reflections are provided in Chapters 2 and 3.

Figure 4.2a shows the modelled common-source gather for a source located at 4500 m, including reflections from all layers within our subsurface model. As discussed in detail in Chapter 2 and Chapter 3, we employ manual picking (as depicted by the dotted red curve in Figure 4.2a) to isolate the reflections from the top and bottom of the reservoir, thereby enhancing the resolution of ghost reflections in the result of SI. Figure 4.2b shows the muted common-source gather, highlighting the reflections from the top and bottom of the reservoir, as indicated by the green and purple arrows, respectively.

Table 4.1: Model parameters per lithostratigraphic unit (Kraaijpoel and Dost, 2013)

Unit	Code	Velocity (m/s)
North Sea group	N	1792
Chalk group	CK	2237
Rijnland group	KN	2129
Upper and lower Germanic trias groups	R	3016
Zechstein group	ZE	4521
Upper Rotliegend group	RO	2734
Limburg group	DC	3327

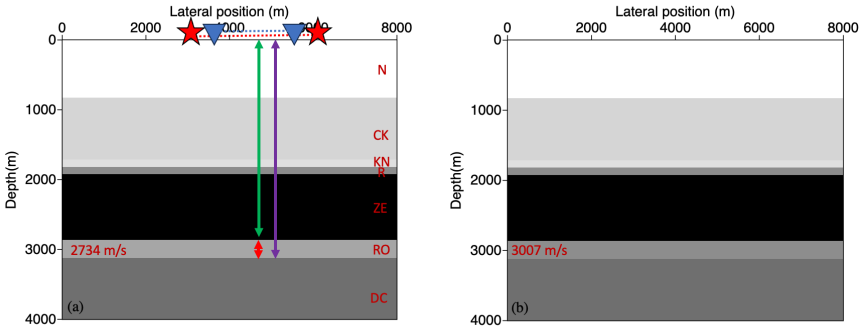

Figure 4.1: The subsurface model of Groningen used for (a) the base survey and (b) for the monitoring survey. Red stars and blue triangles depict the geometry of the active sources and the receivers, respectively, at the surface used for modelling in this study. The red letters represent the subsurface layers described in Table 4.1. The green and the purple arrows represent the reflections from the top and the bottom of the reservoir, respectively, while the red arrow shows the ghost reflection form inside the reservoir.

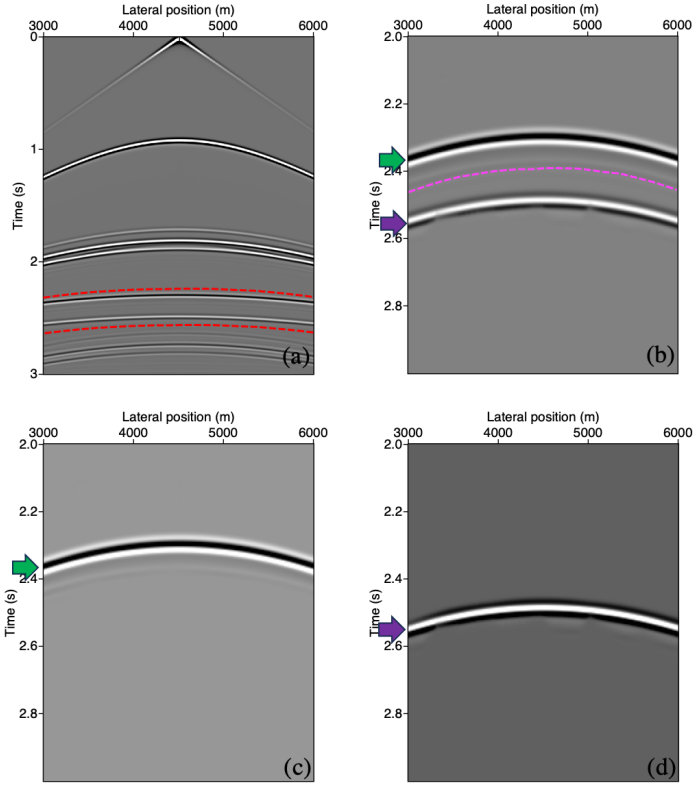

Figure 4.2: (a) Common-source gather for an active shot at 4500 m, (b) the muted common-source gather zoomed in between 2.0 and 3.0 s. (c) The common-source gather containing only the reflection from the top of the reservoir. (d) Same as (c) but with only the reflection from the bottom of the reservoir. The red and magenta dotted curves show the boundary for manually picking for muting undesired events. The green and purple arrows represent the reflection from the top and bottom of the reservoir, respectively.

Subsequently, we apply SI by AC to the muted common-source gathers to retrieve ghost reflections by correlating each trace in all common-source gathers with itself and then stacking over all active sources. Figure 4.3a shows the virtual zero-offset section resulting from applying SI by AC to the muted common-source gathers from the base survey. In Figure 4.3b, a comparable zero-offset section is presented, obtained from the monitoring survey. For a more detailed comparison, we isolated a trace in the middle of the two sections for a virtual source at 4500 m, as depicted in Figure 4.3c. Notably, clear differences in both time and amplitude are evident between the ghost reflections of the base survey and those from the monitoring survey. Chapter 3 delved into further details about the time differences, while this chapter concentrates on investigating the amplitude differences of ghost reflections.

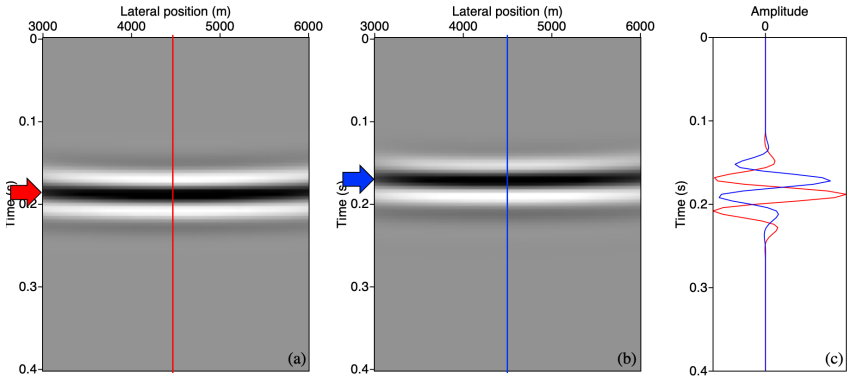

Figure 4.3: (a) The result of SI by AC when muted common-source gathers are used for the base survey and (b) for the monitoring survey. (c) The extracted ghost reflection at 4500 m. The red and blue colours indicate the ghost reflection for the base survey and the monitoring survey, respectively.

As discussed earlier, absolute ghost reflection amplitudes are unreliable, prompting a focus on relative amplitudes. So, we normalise the extracted amplitude of each trace to the maximum extracted amplitude among the traces. For a comprehensive investigation into the amplitude of ghost reflections, we extract the relative amplitude of the ghost reflections in the virtual zero-offset section for all virtual sources using four different approaches. Figure 4.4a shows the relative amplitude of ghost reflections for the directly modelled ghost reflections and four approaches for the base survey as described below.

First, we extract the relative amplitude of the ghost reflection while using muted common-source gathers as input. Note that “amplitude” in this chapter refers to the maximum amplitude. These amplitudes are labeled in Figure 4.4 as "SI-muted" shots. An example of such muted common-source gather is shown in Figure 4.2b. As seen in Figure 4.4a, a small variation in amplitude across different locations is observed. We extensively discussed in Chapter 3 that this phenomenon can occur due to the geometry of the sources and receivers. We showed in Chapter 3 that the ghost reflections are more reliable when the virtual sources are positioned in the middle of the linear array, benefiting from isotropic illumination of surface sources from both sides. Consequently, in Figure 4.4b, we only show the relative amplitude for virtual sources in the middle of the seismic array (4000-5000 m).

Secondly, to further enhance the resolution of ghost reflections, we performed a second manual picking, depicted by the magenta dotted curve in Figure 4.2b, effectively isolating the reflection from the top from the reflection from the bottom of the reservoir. The separated reflection from the top of the reservoir is shown in Figure 4.2c, while that from the bottom is displayed in Figure 4.2d. We apply SI by AC to these two muted common-source gathers. The relative amplitude of the retrieved ghost reflections is demonstrated in Figure 4.4, labeled "SI-Sep".

Thirdly, based on the separated reflections from the top and bottom of the reservoir in the second approach, we normalise the amplitude of the reflection from the bottom of the reservoir (as depicted in Figure 4.2d) to the amplitude of the reflection from the

top of the reservoir (as shown in Figure 4.2c) for each individual receiver. Because the absolute amplitude of the ghost reflections may not be reliable, our aim in applying this normalisation is to mitigate the effects of the overburden on the amplitude (e.g., damping). Figure 4.4 illustrates the amplitude of ghost reflections for the base survey following this normalisation process, labeled "SI-Sepnorm".

Finally, for the fourth step of our investigation, we apply SI by trace deconvolution (Vasconcelos and Snieder, 2008). In this retrieval process, we initially separated the reflections from the bottom of the first and second layers as for the second approach. Then, the first reflection arrival was deconvolved from the second reflection arrival. We expect to obtain similar results as in the third step because we divide the amplitude spectrum of the reflection from the bottom by the amplitude spectrum of the reflection from the top in the frequency domain, which is similar to the third step where we first apply normalisation and then correlation. Figure 4.4 shows the amplitude of the ghost reflection for the base survey retrieved from SI by trace deconvolution, labeled "dcnv".

We also show in Figure 4.4 the relative amplitude of the directly modelled ghost reflections for comparison, labeled "DM" It is important to note that we position the sources directly at the top of the reservoir to obtain the directly modelled ghost reflections. Since there are no lateral velocity or thickness changes inside the reservoir, we have the same amplitude for all sources. Notably, the differences between all four approaches and the directly modelled ghost reflection are less than 5% for the receivers between 4000 m and 5000 m (Figure 4.4b), which is considered acceptable.

We apply the same approaches for retrieving ghost reflections for the monitoring survey. Figure 4.5 shows the relative amplitude using the muted common-source gathers, using the separated reflections, using the normalised separated reflections, using SI by trace deconvolution, and the directly modelled ghost reflection for the monitoring survey where we only have a small velocity change inside the reservoir. Similar to the base survey, we apply normalisation to the maximum amplitude in each approach to retrieve relative amplitudes. As evident from this figure, the patterns remain consistent with those in Figures 4.4, but with different amplitudes.

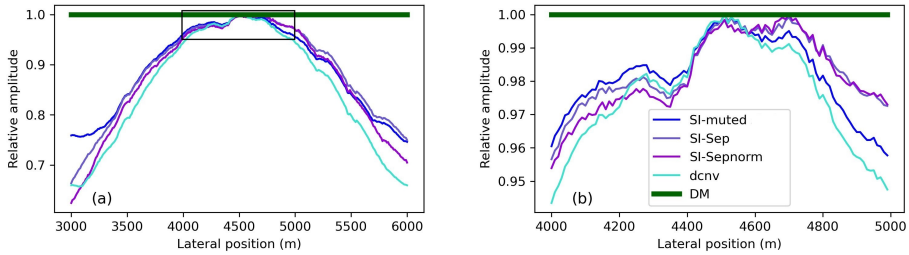

Figure 4.4: (a) The relative amplitudes of the ghost reflections retrieved from the four approaches for the base survey: SI by AC using muted common-source gathers (SI-muted), SI by AC using separated reflections (SI-Sep), SI by AC using normalised separated reflections (SI-Sepnorm), and SI by trace deconvolution (dcnv). The amplitude of the directly modelled ghost reflection is shown as "DM". The amplitude from each trace is normalised to the maximum extracted amplitude among the traces. (b) Same as (a) but for the selected virtual sources at the middle of the receivers line (4000-5000 m). The black highlighted area in (a) indicates the selected virtual source as shown in (b).

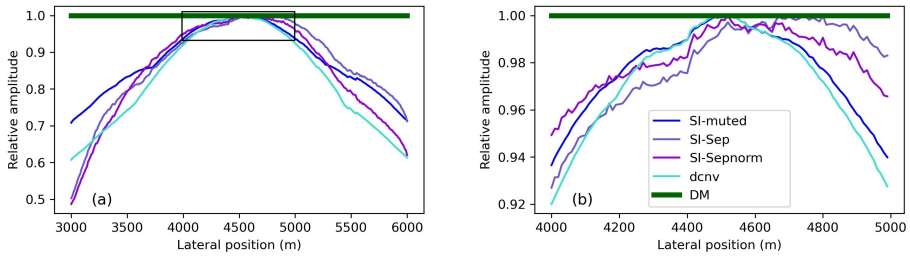

Figure 4.5: Same as Figure 4.4 but for the monitoring survey.

As a final step in our investigation, we employ another step to compare amplitude differences between the ghost reflections of the base survey and the monitoring survey. In this step, we exclusively focus on the retrieved ghost reflection from the third procedure, where we normalise the reflection from the bottom to the reflection from the top and then apply SI by AC. Then, we normalise the ghost reflections from the monitoring survey to those from the base survey for individual virtual sources. We also apply the same normalisation to the directly modelled ghost reflections.

Figure 4.6a shows the relative amplitude for the directly modelled ghost reflections, and Figure 4.6b shows the relative amplitude of the retrieved ghost reflections. As can be observed, there is a noticeable difference between the retrieved ghost reflections of the base survey and the monitoring survey, which is comparable to the directly modelled ghost reflections with the same trend.

When comparing Figure 4.6(a) with Figure 4.6(b), we observe a difference of 0.2 in the relative amplitude of the directly modelled ghost reflections and the ghost reflection retrieved from SI by AC. This difference arises because for the directly modelled ghost reflections we position the sources and receivers exactly at the top of the target layer, and the amplitude of the modelled ghost reflections depends only on the reflection coefficient of the bottom layer. Therefore, the value of 0.6 observed in Figure 4.6(a) is actually the ratio of the reflection coefficient of the target layer from the monitoring survey to that from the base survey.

When applying SI by AC, we effectively multiply the amplitudes of two reflections from the top and bottom of the target layer. Then, through normalisation, the relative amplitude of the ghost reflection not only includes the reflection coefficient for the bottom layer but also the ratio of the reflection and transmission coefficients from the top layer, which is expected to be 0.87. However, what we observe in Figure 4.6(b) is slightly different, which is related to the contribution of sources from non-stationary phase region as we discussed in Chapter 3.

To investigate the effects of the stationary-phase region on the amplitude of ghost reflections, we evaluate the correlation panels. Figures 4.7a, c, and e show the correlation panels for virtual sources at 4000, 4500, and 5000 m, respectively. As we can see in these figures, the number of sources in the stationary-phase region is limited to the sources close to the virtual sources. By stacking all active sources, the relative amplitude of the ghost reflections normalised to the base survey for the monitoring survey is slightly different from the expected value as shown at the bottom of the figure and Figure 4.6b.

However, by tapering the sources in the non-stationary phase region and then stacking (Figures 4.7b, d, and f), the relative amplitude is exactly the same as the expected value, which is 0.87. This highlights that stacking only sources in the stationary-phase region yields more reliable results, as discussed in Chapter 3.

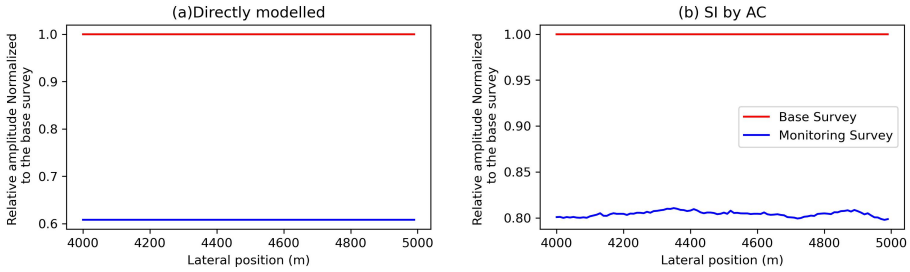

Figure 4.6: The relative amplitude of the ghost reflections normalised to the base survey (a) for the directly modelled ghost reflections and (b) for the result of SI by AC with normalization.

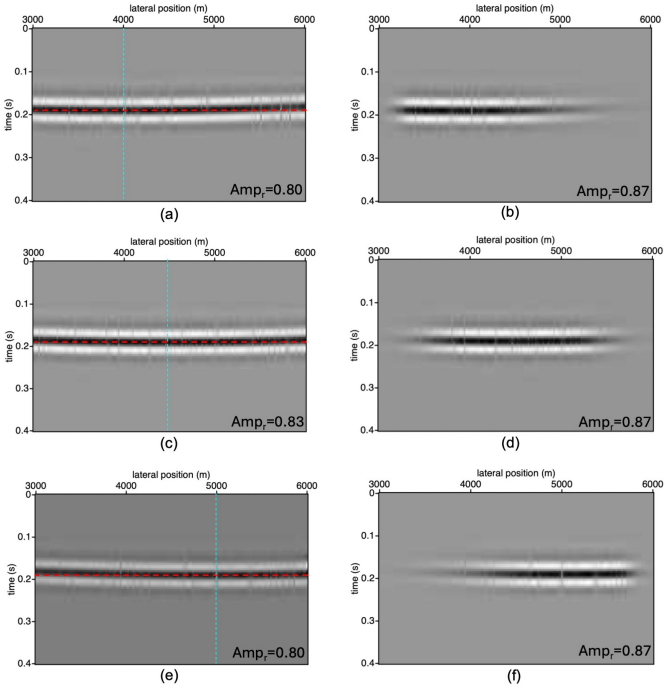

Figure 4.7: (a) The correlation gathers for a virtual source at 4000 m, (b) The tapered correlation gathers for a virtual source at 4000 m, (c), and (d) same as (a) and (b), respectively but for a virtual source at 4500 m, (e), and (f) same as (a) and (b), respectively but for a virtual source at 5000 m. The values in each figure show the relative amplitude of the ghost reflections normalised to the base survey for the monitoring survey. The sources deviating from the red line are outside the stationary phase region.

4.4. DISCUSSION

We demonstrated that the relative amplitude of the ghost reflection can serve as a monitoring tool for detecting small velocity changes within the reservoir, in addition to time shifts. These differences are specifically linked to changes within the target layers (in this case, the reservoir) without any kinematic effects of the overburden and underburden.

We extracted the amplitude of the ghost reflections using four approaches: SI by AC using muted common-source gathers, SI by AC using separated reflections, SI by AC using normalised separated reflections, and SI by trace deconvolution. We observed that the relative amplitude from the base survey (Figure 4.4) and the monitoring survey (Figure 4.5) showed the same trend for these four approaches. It is more acceptable to consider the amplitude of the third approach when using normalisation to the reflection from the top layer and the fourth approach, which is trace deconvolution. Both approaches are similar in the frequency domain. We presented SI by trace deconvolution because it is challenging for some subsurface models to separate the reflection from the top and bottom of the target and then apply normalisation. Instead, we can apply SI by trace deconvolution.

We demonstrated that the relative amplitude of the ghost reflection is influenced by both the reflection coefficient of the bottom of the target layer and the ratio of the reflection and transmission coefficients from the top of the target layer. In our numerical modelling, we assume that changes occur only within the target layer. Under this assumption, the calculated relative amplitude represents changes exclusively within the target layer. However, if changes occur in not only the target layer, but also in the layer above it or in the layer below it, the relative amplitude must be interpreted as representing changes within these layers. Since significant changes typically occur within the target layer, contributions from other layers can often be ignored. Alternatively, investigating the combined amplitude changes and time shift of the ghost reflection from the target layer and the ghost reflections from multiple layers (as discussed in Chapter 2) can be beneficial.

We demonstrated that the contribution of sources from the stationary-phase region results in more reliable relative amplitude of the ghost reflections. Therefore, it is recommended to evaluate the correlation panels before stacking. However, if investigation of the stationary phase is not feasible due to a more complex subsurface, as discussed in Chapter 3, it is still advisable to maintain optimal spacing between receivers (or sources). This spacing should be at least two samples per dominant wavelength. Additionally, an inline array with a two-sided uniform distribution of the sources (or receivers) should be utilised, with an extended length for sources (or receivers) on both sides. This ensures the retrieval of high-resolution ghost reflections, at least for the virtual sources located in the middle of the array. This approach may still yield desirable results because the differences between the relative amplitudes for the ghost reflection retrieved from stacking all sources and stacking only sources from the stationary-phase region are small, as shown in Figure 4.7.

Besides the effects on the amplitude of ghost reflections, the stationary-phase region, also affects the time of ghost reflections, as discussed in Chapter 3. Given that our subsurface model consists of horizontally layered structure and the retrieved ghost reflections propagate only within the target layer, we expect to see horizontal ghost re-

flections in the virtual zero-offset sections in Figure 4.3. However, upon examining the results, we observe a curvature. This curvature is related to the stationary-phase region, where there are not enough sources in this region for the receivers located at the ends of the receiver line.

We applied SI by AC and by trace deconvolution to retrieve ghost reflections, resulting in zero-offset sections. However, applying SI by cross-correlation (CC) is also possible. The output of SI by CC is a multi-offset gather, enabling the investigation of amplitude changes versus offset. We also investigated the amplitude of ghost reflections retrieved from SI by CC using a simpler subsurface model. An example illustrating the retrieval of ghost reflection amplitudes from SI by CC is provided in section 4.6.

4.5. CONCLUSION

We investigated the feasibility of using the amplitudes of retrieved ghost reflections for reservoir monitoring, employing numerical datasets based on the Groningen subsurface model. Ghost reflections are obtained through seismic interferometry (SI) by autocorrelation and by trace deconvolution of two primary reflections from different depth levels in an active-source seismic survey, where sources and receivers are at the surface.

We demonstrated that changes in velocity within the Groningen reservoir lead to amplitude changes in the retrieved ghost reflections. Comparing the amplitudes from the ghost reflections with amplitudes from directly modelled results, we showed that the ghost-reflection relative amplitudes are reliable enough to detect changes for monitoring purposes. This seismic attribute has the potential for monitoring changes within the reservoir, given careful consideration to normalising the reflection from the bottom of the reservoir to the reflection from the top of the reservoir before applying SI or using trace deconvolution and retrieving relative amplitude instead of absolute amplitude. The relative-amplitude changes, along with the time shift of the ghost reflections, can serve as tools for monitoring specific small changes inside the reservoir without the influence of the overburden.

4.6. SUPPLEMENTARY MATERIAL

4.6.1. THE AMPLITUDES OF GHOST REFLECTIONS RETRIEVED FROM SI BY CC

To investigate the amplitudes of ghost reflections retrieved from SI by CC, we employ a simple horizontal subsurface model to simulate recordings from sources at the surface to receivers at the surface (Figure 4.8). For this modelling, we used receivers positioned between 3000 and 5000 m with 20 m intervals, and sources between 2010-5010 with 40 m intervals. We considered the receiver at 3000 m as a virtual source.

Our aim is to investigate the amplitudes of the ghost reflection retrieved from SI by CC, which propagated inside the second layer, using muted common-source gathers. After applying SI, we extract the absolute amplitudes of the ghost reflection. As discussed in section 4.2, these amplitudes are then normalised to their maximum value. For a comparative analysis, we additionally obtained a common-source gather directly modelled for a source located at the position of the virtual source but at the top of the second layer, representing directly modelled ghost reflections.

Figure 4.9a shows the retrieved ghost reflection from SI by CC and Figure 4.9b shows the directly modelled ghost reflections. Figure 4.9c shows the relative amplitude of these ghost reflections. The differences in the relative amplitude of ghost reflections retrieved from SI by CC and separated common source gathers are similar to the directly modelled ghost reflections. However, beyond a distance of 3900 m, we can see some artefacts, which is the critical distance for this subsurface model and a virtual source at 3000 m where the refractions appear in common-source gathers. Therefore, we successfully retrieve the amplitude of ghost reflections with an acceptable difference before reaching the critical distance.

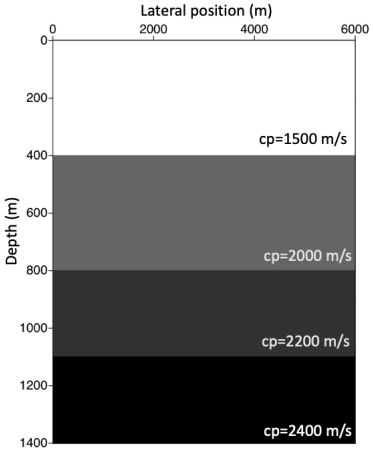

Figure 4.8: The subsurface model used for applying SI by CC.

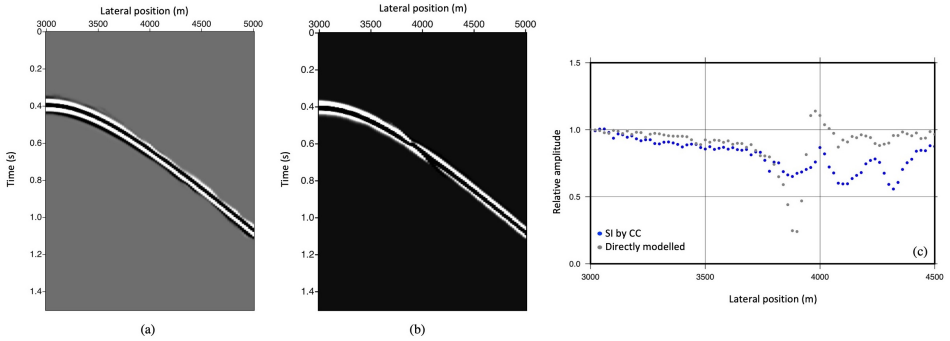

Figure 4.9: (a) The ghost reflection retrieved from SI by CC for a virtual source at 3000 m, (b) directly modelled ghost reflection, and (c) the relative amplitude of ghost reflection from inside the second layer as a function of the receivers' location using the ghost reflection retrieved from SI by CC (blue circles) and directly modelled ghost reflection (gray circles).

4.7. DATA AVAILABILITY

The data and codes underlying this chapter are available in repository 4TU.ResearchData at https://doi.org/10.4121/6b9507f5-12ca-41b7-8926-497f2048fa00. The dataset is under embargo and becomes available in the repository after August 2025.

REFERENCES

Bjørlykke, K. (2010). *Petroleum geoscience: From sedimentary environments to rock physics*. https://doi.org/10.1007/978-3-642-02332-3

Brown, A. (1991). Interpretation of three-dimensional seismic data. Third edition. *SEG Investigations in Geophysics*.

Dimri, V. P., Srivastava, R. P., & Vedanti, N. (2012). Seismic Reservoir Monitoring. *Handbook of Geophysical Exploration: Seismic Exploration*, *41*, 65–88. https://doi.org/10.1016/B978-0-08-045158-9.00004-X

Halliday, D., Curtis, A., Robertsson, J. O., & van Manen, D. J. (2007). Interferometric surface-wave isolation and removal. *Geophysics*, *72*(5), A69–A73. https://doi.org/10.1190/1.2761967

Kraaijpoel, D., & Dost, B. (2013). Implications of salt-related propagation and mode conversion effects on the analysis of induced seismicity. *Journal of Seismology*, *17*, 95–107. https://doi.org/10.1007/s10950-012-9309-4

Thorbecke, J. W., & Draganov, D. (2011). Finite-difference modeling experiments for seismic interferometry. *Geophysics*, *76*(6), H1–H18. https://doi.org/10.1190/geo2010-0039.1

Vasconcelos, I., & Snieder, R. (2008). Interferometry by deconvolution, Part 1 - Theory for acoustic waves and numerical examples. *Geophysics*, *73*, S115–S128. https://doi.org/10.1190/1.2904554

Wapenaar, K. (2006). Green's function retrieval by cross-correlation in case of one-sided illumination. *Geophysical Research Letters*, *33*(19), L19304. https://doi.org/10.1029/2006GL027747

5

RECURSIVE INTERFEROMETRIC SURFACE-WAVE SUPPRESSION

High-resolution seismic reflections are essential for imaging and monitoring applications using data-driven methods such as SI and the Marchenko method. In seismic land surveys using sources and receivers at the surface, surface waves often dominate, masking the reflections. We apply seismic interferometry (SI) by cross-correlation by turning receivers into virtual sources to estimate the dominant surface waves. Afterwards, we perform adaptive subtraction to minimise the difference between the surface waves in the original data and the result of SI.

We use a 2D seismic reflection dataset from Scheemda, situated in the Groningen province of the Netherlands, to illustrate the technique's efficiency. A comparison between the data after the recursive interferometric surface-wave suppression (RISS) and the original data across time and frequency-wavenumber domains shows significant suppression of surface waves, enhancing visualisation of reflections for future subsurface imaging and monitoring studies.

This Chapter is under preparation for publication. The preprint available as Shirmohammadi, F., Draganov, D., Ghose, R., Verschuur, E., & Wapenaar, K., (2024) Recursive interferometric surface-wave suppression for improved reflection imaging, 1-24. https://doi.org/10.48550/arXiv.2411.02620.

5.1. INTRODUCTION

Seismic data acquired on land often is contaminated by surface waves, which act as a significant source of noise in reflection seismic studies. These surface waves often have similar velocity and frequency content to those of the investigated reflections. They obscure the clarity and quality of the reflected waves, which are the waves of interest for various applications such as imaging and monitoring. For instance, in Chapters 2 and 3, we discussed the importance of high-resolution reflection datasets for retrieving ghost reflections using SI. We suggested suppressing surface waves as a preprocessing step before retrieving ghost reflections.

Conventionally, surface waves are suppressed during data processing using methods such as frequency-offset (f-x) (Yilmaz, 2001), frequency-wavenumber (f-k) filters, or bandpass filters. However, these approaches can prove ineffective when surface waves are scattered and overlap with the frequency regions of the reflected body waves that we intend to preserve. The f-k filter may result in artefacts due to signal distortion and spatial correlation of the background noise because the energy of surface-waves is distributed over a wide portion of the f-k spectrum (Konstantaki et al., 2015), thus further lowering the quality of reflections.

Recently, the prediction of surface waves with SI and their subsequent adaptive subtraction from seismic reflection data has emerged as a technique for suppressing surface waves. In SI, seismic observations from various receiver locations are cross-correlated to retrieve new seismic responses from virtual sources positioned at the receivers' locations. This process enables the retrieval of seismic responses between pairs of receivers. The obtained responses are then subtracted from the original field recordings, resulting in data with suppressed surface waves achieved through the utilisation of least-squares matching filters (Halliday et al., 2010). This suppression technique is usually called interferometric surface-wave suppression. In previous studies, the interferometric surface-wave suppression was only done once on the data. Halliday et al. (2010) demonstrated its effectiveness in the context of hydrocarbon exploration, while Konstantaki et al. (2015) and Liu et al. (2018) showcased its utility for near-surface applications. Additionally, Balestrini et al. (2020) demonstrated its application for deep mineral explorations. We suggest a new approach where the initial suppression results are used for further iterations, followed by adaptive subtraction. We term this technique Recursive Interferometric Surface-wave Suppression (RISS). This technique aims to enhance the efficacy of the surface-wave suppression through an iterative process.

In this study, we apply RISS using a 2D reflection dataset acquired in Scheemda, Groningen province, the Netherlands. By employing this technique, we aim to enhance and improve the visualisation of reflections, thereby providing clearer insights into subsurface structures and enhancing the overall interpretation of the seismic data. Additionally, we prepare the data for future data-driven applications such as the Marchenko method (Chapter 6) or ghost reflection retrieval (as in Chapters 2 and 3). Additionally, we compare the RISS results with other techniques such as time muting and fk filtering.

In the following sections, we introduce the method in Section 5.2, followed by the description of the seismic data acquisition in Section 5.3, elaborate the results in Section 5.4, and finally discuss some points and then conclusions.

5.2. RECURSIVE INTERFEROMETRIC SURFACE-WAVE SUPPRESSION (RISS)

In our proposed approach, SI is employed to retrieve the dominant surface waves. The retrieved surface-wave energy is subsequently adaptively subtracted from the dataset. Following this, the obtained data is utilised to iterate through these two steps, contributing to the improvement of reflection resolution. This section outlines the implementation of RISS.

5.2.1. SURFACE-WAVE RETRIEVAL BY SEISMIC INTERFEROMETRY

SI refers to the method of retrieving new seismic responses, for example between two receivers using cross-correlation as if there were a source at one of the receiver locations. This process is most commonly achieved in an active seismic survey by cross-correlating the recordings at the two receivers and stacking the correlated traces over all available active sources. So, the retrieved response between two receivers at positions x_A and x_B can be expressed in the frequency domain, as described by Halliday et al. (2007):

$$\hat{G}^*(x_B, x_A, \omega) + \hat{G}(x_B, x_A, \omega) \propto \sum_{n=1}^{N} \hat{G}^*(x_A, x_n, \omega)\hat{G}(x_B, x_n, \omega), \tag{5.1}$$

where $\hat{G}(x_B, x_n, \omega)$ is the frequency-domain response of a recording at receiver x_B from a source at x_n and $\hat{G}(x_A, x_n, \omega)$ is the frequency-domain response of a recording at receiver x_A from a source at x_n at the Earth's surface. The left-hand side of the equation represents the response between two receivers at x_A and x_B, implying that we turn the receiver at x_A into a virtual source. The symbol $(*)$ denotes the complex conjugate in the frequency domain, while N represents the total number of active sources at the surface.

As shown in Chapters 2 and 3, when using sources and receivers at the surface, the direct arrival, pseudo-physical reflections, surface waves, and ghost reflections are retrieved. In a laterally homogeneous medium, sources at points in line with the receivers contribute to the retrieval of direct surface arrivals since they are all in the stationary-phase region, but only a few points are stationary to retrieve pseudo-physical or ghost reflections and scattered surface waves. This way, the results retrieved by SI will be dominated by surface waves (Balestrini et al., 2020).

Figure 5.1 shows a schematic representation of SI for retrieving direct arrivals or surface waves. By correlating the recording at x_B from the active source at x in Figure 5.1a with a recording at x_A in Figure 5.1c, the correlated response between x_B and x_A is retrieved, as illustrated by the purple arrow in Figure 5.1d at causal times (The causal part refers to times later than the zero time). Similarly, the correlated response between another receiver at $x_{B'}$ and a receiver at x_A is retrieved by correlating the response at $x_{B'}$ in Figure 5.1b with x_A in Figure 5.1c, as depicted by the orange arrow in Figure 5.1d at acausal times (The acausal part refers to times earlier than the zero time). In this case, the receiver at x_A acts as a virtual source as shown by the blue star in Figure 5.1d. We repeat this procedure for all active sources as shown in Figure 5.1e for another active source at x'. Finally, the Green's function between the virtual source at x_A and other receivers at x_B, $x_{B'}$, and $x_{B''}$ are retrieved by stacking all correlated responses as shown in Figures 5.1d and 5.1e.

Since we apply this technique to a field dataset, there are certain points that need to be addressed in order to improve the resolution of our retrieved responses.

First, we aim to retrieve surface waves with SI, which are direct arrivals. So, it is required that all receivers be considered on the same side of the active source, e.g. for an active source at x, we correlate the response for receivers x_B and $x_{B'}$ located on the same side as the virtual source at x_A. In the same way, for an active source at $x^{'}$, we consider all receivers because they are on the same side as the virtual source at x_A as shown in Figure 5.1e.

Second, in the case of isotropic illumination of the receivers, a time-symmetric response between the receivers is obtained (Wapenaar et al., 2010). Consequently, one can sum the causal and the time-reversed acausal parts of the correlated panels to improve the signal-to-noise ratio. The causal part refers to times later than the zero time (positive time), and the acausal part refers to times earlier than the zero time (negative time). However, in our case, when the illumination is not homogeneous from all sides for each pair of receivers, then parts of the response can be retrieved at acausal times and other parts at causal times. Therefore, to enhance the quality of our retrieved responses, we meticulously assess the positions of virtual source-receiver pairs and active sources. Subsequently, we opt to stack either the causal or time-reversed acausal part of the correlation panel.

Considering the conditions of one-sided distribution of receivers and causality, we limit ourselves to a lower number of traces for stacking. To maintain a high signal-to-noise ratio, we stack traces only when we have at least half the number of all active sources. We can summarise this as follows:

$$trace\begin{cases} \text{causal part, if } n > N/2 \text{ with } x < x_A < x_B, \text{ or } x > x_A > x_B, \text{or } x_A = x_B \\ \text{acausal part, if } n > N/2 \text{ with } x < x_B < x_A, \text{ or } x > x_B > x_A \end{cases}$$

Here, x is the position of the active sources, x_A is the position of the virtual source, x_B is the position of the receiver, and n is a number of active sources for stacking which should be higher than half the total number of active sources N. For instance, as illustrated in Figure 5.1d, for the receiver at $x_{B'}$ on the left side of the virtual source at x_A, we consider the acausal part, as indicated by the orange arrow. Similarly, for a receiver at x_B, we consider the causal part, denoted by the purple arrow. Furthermore, as depicted in Figure 5.1e, for the receiver at x_B on the right side of the virtual source at x_A, we consider the acausal part, and for other receivers at $x_{B'}$ and $x_{B"}$, we consider the causal part, as shown by the purple arrows.

Subsequently, considering the above factors, we successfully retrieve the virtual common-source gather for all receivers.

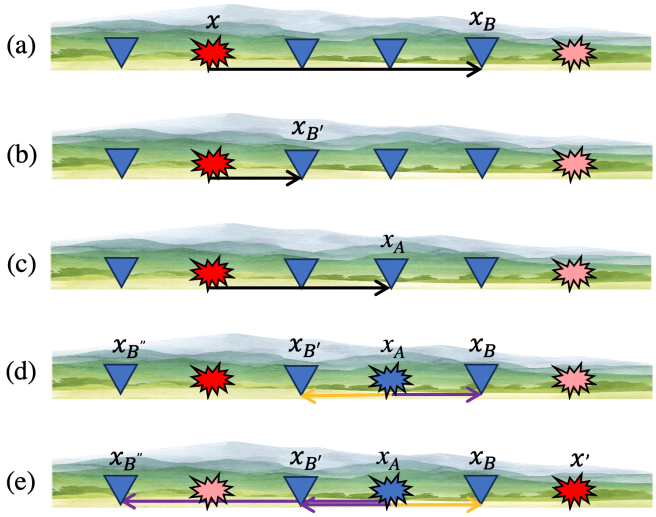

Figure 5.1: Schematic representation of seismic interferometry for retrieving surface waves. (a), (b), and (c) The surface wave recorded at x_B, $x_{B'}$, and x_A from the active source at x, respectively. (d) The result of correlating the response at x_A with other receivers, and thus turning x_A into a virtual source. (e) Same as (d) but for the active source at x'. The black arrows indicate the surface waves, while the orange and purple arrows represent the outcomes of correlation, considering the causal and acausal parts, respectively.

5.2.2. ADAPTIVE SUBTRACTION

When each source position in an active-source survey is in close proximity to a receiver position, we will be able to identify a corresponding retrieved virtual common-source gather with the estimated dominant surface waves for each active source–virtual source pair. These estimates can then be adaptively subtracted from the complete responses of the active source–virtual source pair (Halliday and Curtis, 2008, Halliday et al., 2010, Konstantaki et al., 2015).

Figure 5.2 shows the basic principle of adaptive subtraction. Figure 5.2a illustrates schematically a simple seismic trace that consists of a primary reflection at 100 ms, shown in black, and surface waves at 300 ms, 350 ms, and 400 ms in blue. Figure 5.2b shows the result of SI, which contains surface waves. By minimising the difference between Figure 5.2b and Figure 5.2a, the surface waves in Figure 5.2a can be suppressed partly, as shown in Figure 5.2c. The minimisation is done by estimating a shaping filter $\mathbf{f}$ that can minimise the following objective function (Liu et al., 2018; Balestrini et al., 2020):

$$\min_{\boldsymbol{f}} \| D - \boldsymbol{f} D_{\mathrm{SW}} \|^2, \tag{5.2}$$

where D is the field dataset with surface waves and D_{SW} are the surface waves retrieved by SI using the field dataset. The vertical double bars $||.||^2$ represent the L2 norm. Equation 5.2 is solved using an iterative least-squares fit (Verschuur et al., 1992). More details can be found in Alá'i and Verschuur (2003) and Verschuur (2013). The multiplication between the $\mathbf{f}$ and D_{SW} is directly subtracted from D, giving D_{ref} which represents the

data after surface-wave suppression as

$$D_{\text{ref}} = D - \boldsymbol{f} D_{\text{SW}}. \tag{5.3}$$

As shown in Figure 5.2c, the data after adaptive subtraction may still contain surface waves due to, for example, errors in estimating higher modes of surface waves. Therefore, we suggest repeating the same step of SI and adaptive subtraction but now using the output of the first adaptive subtraction, represented here as Figure 5.2c, as input for SI. We estimate surface waves from SI, as shown in Figure 5.2d, and then adaptively subtract them from Figure 5.2c. Figure 5.2e shows the final result, whereby repeating these steps, we increase our chances of suppressing all the surface-wave energy and preserving weak reflections (the black event). We call this technique the RISS. Note, that RISS can be applied for one iteration or multiple iterations.

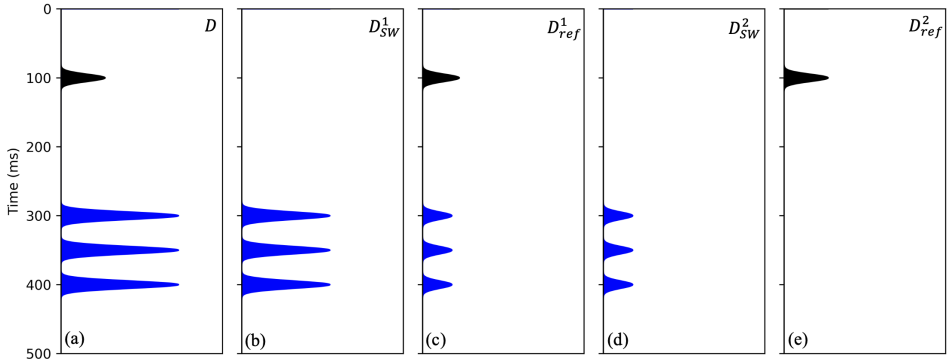

Figure 5.2: Schematic representation of RISS. (a) A seismic trace D with a primary reflection in black and surface waves in blue, (b) D^1_{SW} is a result of SI, (c) D^1_{ref} is the trace after the first iteration of RISS, (d) D^2_{SW} is a result of SI when using D^1_{ref} in (c) as input, (e) D^2_{ref} after a second iteration of RISS.

5.3. SEISMIC DATA ACQUISITION

In the summer of 2022, we acquired seismic reflection data along a line close to the town of Scheemda in the Groningen province of the Netherlands. Figures 5.3a and 5.3b show the location of the site and the geometry of the reflection line, respectively. We employed an electric seismic vibrator (Noorlandt et al., 2015) as a source, with a spacing of 2 m (red stars in Figure 5.3b), and 601 three-component geophones as receivers (the circles in Figure 5.3b), with a spacing of 1 m. The acquisition parameters are summarised in Table 5.1.

We made use of the Lightning electrical vibrator from Seismic Mechatronics (https://seismic-mechatronics.com/) in S-wave mode and oriented in the crossline direction. We then used the data recorded by the crossline horizontal component of the geophones. Because of the orientation of the sources and the receivers, and assuming no scattering from the crossline direction, the horizontally polarised S-waves (SH-waves)

we record are generally decoupled from the compressional and vertically polarised S-waves.

Table 5.1: Acquisition parameters

Parameter	Value
Number of source positions	151
Source spacing	2 m
First source position	150.5
Last source position	450.5
Number of receiver positions per source	601
Receiver spacing	1 m
First receiver position	0 m
Frequency range of the sweep	8-250 Hz

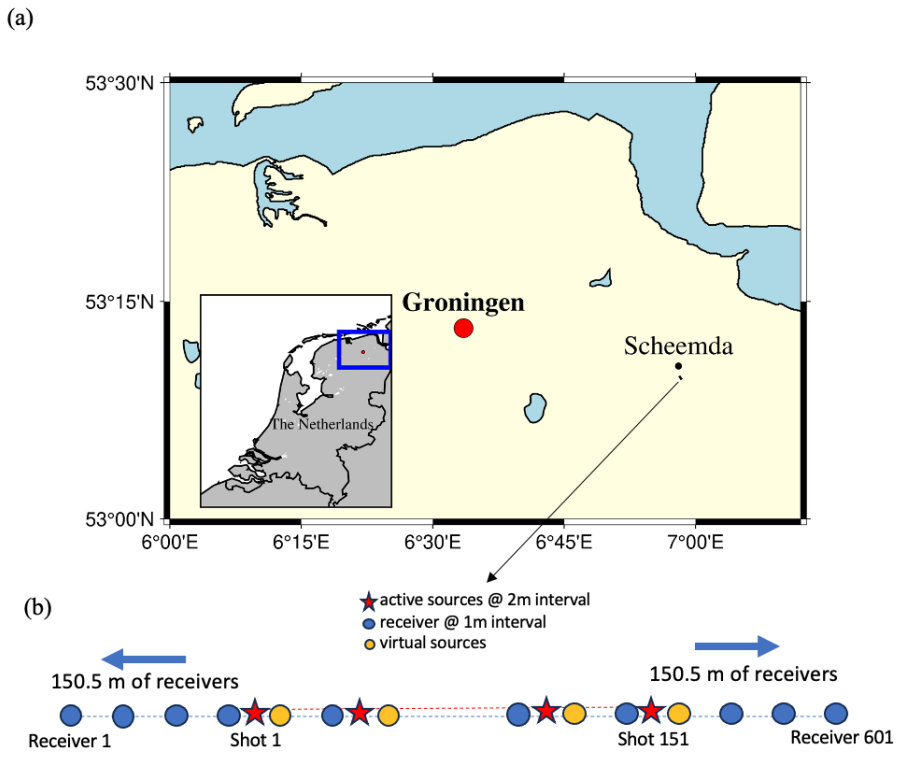

Figure 5.3: (a) Location of the site, and (b) the geometry of the reflection line. The red stars represent active sources, the blue circles represent receivers, and the orange circles represent receivers which act as virtual sources for applying the RISS.

5.4. RESULTS

The primary aim of this study is to illustrate the effectiveness of the RISS method applied to common-source gathers of field data, as introduced in Section 5.2 . The data processing involved several steps. Figure 5.4 shows a flowchart of these steps for the RISS, but also other techniques such as fk filtering and surgical muting for surface-wave suppression.

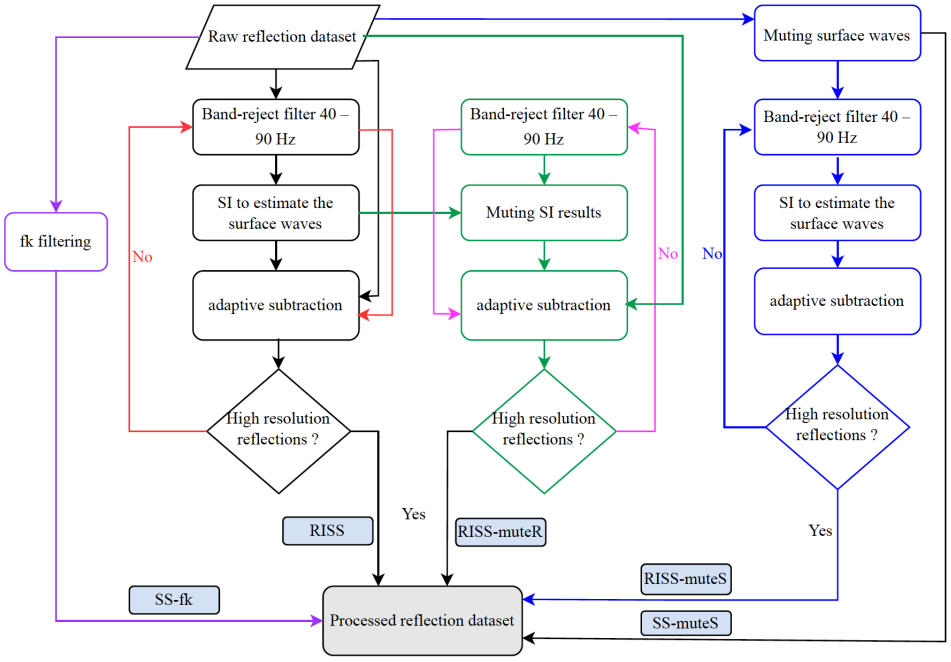

Figure 5.4: Flowchart for applying surface-wave suppression. RISS represents steps for the Recursive Interferometric Surface-wave Suppression, the RISS-muteR is the same as RISS but using muted SI results, the RISS-muteS is the same as RISS but using time-muted reflection dataset as input for SI, SS-fk represents surface-wave suppression using fk filtering, SS-muteS represents surface-wave suppression using time-muted reflection dataset.

As shown in Figure 5.4, first we apply a band-reject filter between 40 Hz and 90 Hz to all active common-source gathers. The main idea is to reject frequencies that might contain reflections but not surface waves so that the SI result would predominantly contain retrieved surface waves. We select these frequencies based on the power spectrum of the common-source gathers. We then apply SI as described in section 5.2.1 by selecting each receiver close to active sources to turn it into a virtual source, as shown by the orange circles in Figure 5.3b.

Next, we adaptively subtract the result retrieved from SI for each virtual source from the original active-source data which is closest to the virtual source to suppress the surface waves using an estimated matching filter as described in section 5.2.2. It is essen-

tial to determine some parameters for the matching filter, including time window, space window, and filter length. We chose a window with the 20 traces for the space window and 0.2 s in time, with a filter length of 0.05 s. We apply the same steps for all virtual sources. Figure 5.5a shows an example original common-source gather in the time domain, while Figure 5.5b shows the same gather after the RISS with one iteration for an active shot at lateral position 320.5 m.

As illustrated in Section 5.2.2, we proposed to apply the RISS for more than one iteration which means we use the data after the first iteration of the RISS as input for applying SI. Then, we repeat all steps from band-reject filtering, SI, and adaptive subtraction. Note that these steps are shown as "RISS" in the flowchart in Figure 5.4.

Figure 5.5c shows the same gather as in Figures 5.5a and 5.5b but after the second iteration of the RISS. Comparing these three results, we observe that a large part of the surface-wave energy is suppressed in Figure 5.5c, as shown by the red arrows. Figures 5.5d-5.5f show the frequency-wavenumber spectra of the common-source gathers in Figures 5.5a-5.5c, respectively. The surface waves appear as linear events in the frequency-wavenumber domain, as indicated by the blue arrows; they are largely suppressed from the data after the RISS with two iterations, as can be observed in Figure 5.5f.

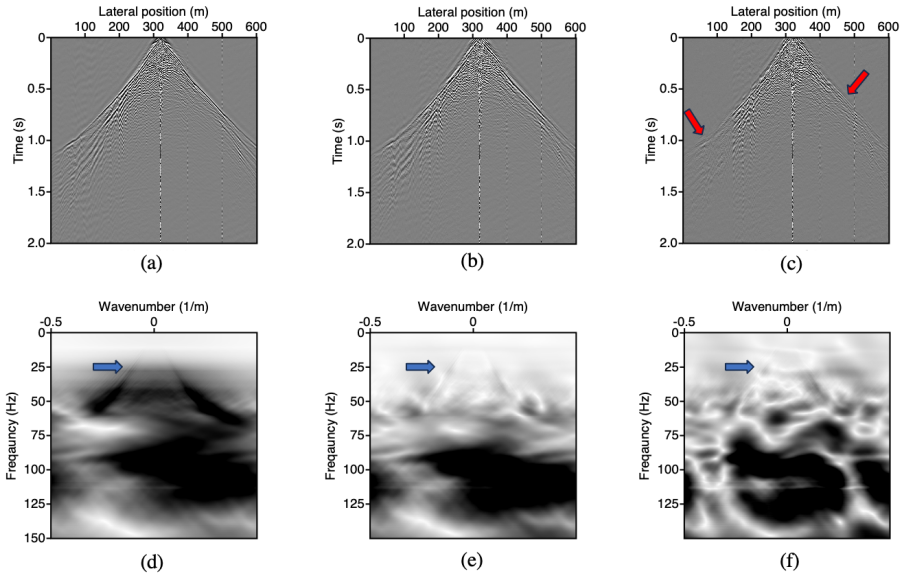

Figure 5.5: (a) A common-source gather for a source located at lateral position 320.5 m, (b) same common-source gather after the first iteration RISS, (c) same common-source gather after the second RISS, and (d), (e) and (f) same as (a), (b), and (c), respectively, but in the frequency-wavenumber domain. Red arrows point to suppressed surface waves in the space-time domain and blue arrows point to surface-wave energy in the frequency-wavenumber domain.

Figure 5.6 shows another example for an active source at a lateral position of 430.5 m, where we also observe significant suppression of the surface waves in both the space-time and frequency-wavenumber domain.

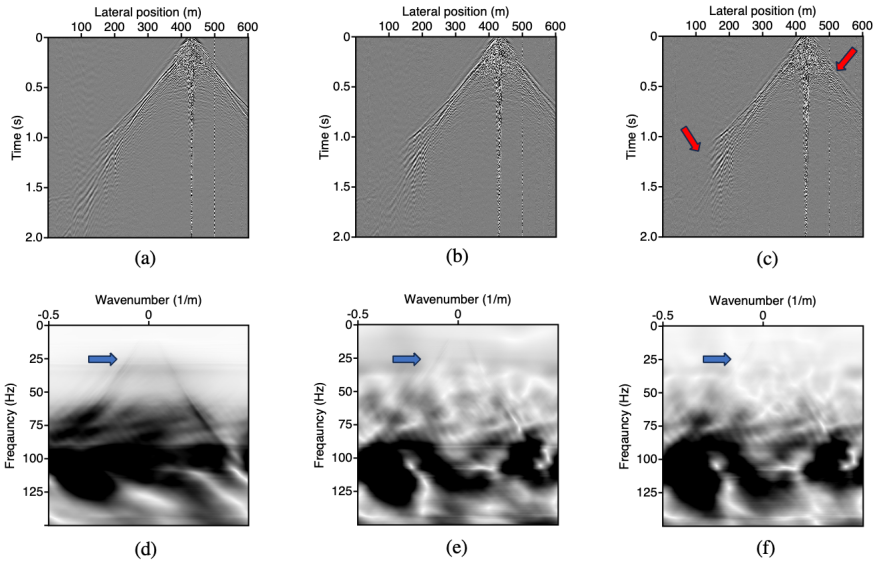

Figure 5.6: Same as Figure 5.5 but for a source at a lateral position at 430.5 m.

As depicted in Figures 5.5c and 5.6c, we successfully suppress surface waves. However, it appears that some deeper reflections are also suppressed in the process. To preserve these reflections, we apply a bottom muting to the virtual-common-source gathers retrieved from SI before adaptive subtraction, which we label as "RISS-muteR" in the flowchart in Figure 5.4. Figures 5.7b and 5.7e show the common-source gather after applying the RISS using the muted SI results for two active sources at 320.5 m and 430.5 m, respectively. In comparison with Figures 5.7a and 5.7d, which show the same common-source gather after RISS, we observe clearer deeper reflections as shown by the red arrows.

By examining the common-source gathers, we observe that it is also feasible to suppress some parts of the surface waves through surgical muting. Therefore, prior to applying the RISS, we also surgically mute prominent surface waves. We label this procedure as "RISS-muteS" in the flowchart in Figure 5.4. Figures 5.7c and 5.7f show the common-source gather after the RISS-muteS. Although we enhance the resolution of some reflections, it seems we still have some strong surface waves in comparison with the results in Figures 5.7a and 5.7d as highlighted by the blue ellipses. This observation underscores the fact that by suppressing surface waves in common-source gathers before the RISS, it becomes challenging to retrieve surface waves from SI.

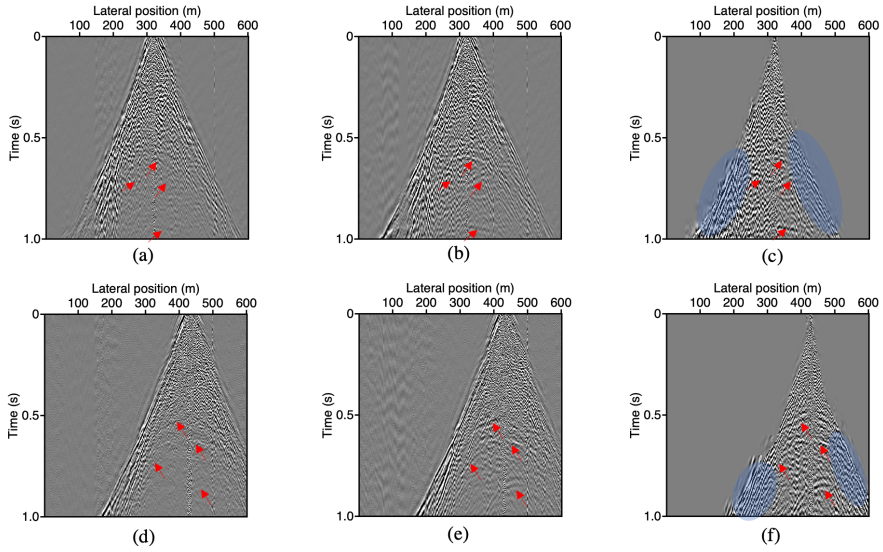

Figure 5.7: (a) A common-source gather for a source located at lateral position 320.5 m after the RISS, (b) same common-source gather after the RISS-muteR, (c) same common-source gather after the RISS-muteS, (d), (e) and (f) same as (a), (b), and (c), respectively, but for a source at lateral position at 430.5 m. Red arrows point to enhanced reflections, while the blue ellipses highlight surface waves.

After the suppression of the surface waves, we apply conventional seismic processing to obtain preliminary unmigrated stacked sections for better comparison between the result of the RISS and conventional suppression techniques. A summary of these steps is shown in the Table 5.2. We first apply bandpass filtering, amplitude correction for absorption effects and geometrical spreading, and then Automatic Gain Control (AGC) for amplitude balancing. We also apply time muting to mute prominent surface waves in the time domain.

Next, we sort the data into CMP gathers (CMP spacing 0.5 m). As expected, the CMP fold increases at the center of the line where better illumination is achieved. We then apply Normal MoveOut (NMO) correction using a constant velocity of 350 m/s, and finally, we stack the CMP gathers. To ensure the reliability of the stacked section, we first apply these steps to the muted common-source gathers without applying the RISS. Figure 5.8 shows the preliminary unmigrated stacked section between CMP 151.25 and 450.25 m. This result is comparable with results from other studies, e.g., as in Kruiver et al. (2017). Strong reflectors are marked by orange arrows.

Since we know that the most significant influence of the surface waves is related to the shallowest part of the subsurface, we focus our attention on those parts, specifically 400-800 ms (Figure 5.9). Figure 5.9a shows the time section obtained after suppressing the surface waves using surgical muting, as indicated by SS-muteS in the flowchart. We use this figure as a reference. Figure 5.9b shows the time section using the result after the second iteration of the RISS. In comparison with the reference time section, it is obvious that some of the expected reflectors are suppressed as shown by the light blue, red, and

green arrows.

To address this issue, we use the RISS-muteR. Figure 5.9c illustrates the time section obtained after the application of this technique. In comparison with the reference in Figure 5.9a, we retrieve all reflectors, which are clearer and more continuous as indicated by the light blue, red, and green arrows. Moreover, some dome-like structures are now interpretable as highlighted by the red curves.

Figure 5.9d shows the time section after applying RISS-muteS. Comparing this image to the images in Figures 5.9a, 5.9c, we see that the lateral continuity of the reflectors is worse, e.g., inside the blue ellipse, while the general character of the left part of the image has become lower in frequency, which might point to left-over dominant surface-wave energy. Figure 5.9e shows the time section obtained after suppression of the surface waves by fk-filtering (SS-fk), which is also a very common suppression technique. Comparing this image to the images in Figures 5.9a, 5.9c, we see that the result is generally of good quality. The reflector indicated by the green arrow even appears laterally more continuous than in Figures 5.9a, 5.9c. However, other reflectors are less clear, e.g., the one indicated by the blue arrow or in the left part of the image earlier than 600 ms (see specifically inside the blue ellipse).

As a result of the comparisons, we deem as the best image the one in Figure 5.9c, i.e., after application of RISS-muteR, because of its clarity but also because the surface-wave suppression is data-driven.

Table 5.2: Summary of seismic processing steps.

Step	Instruction
1	Band-pass filter between 30-100 Hz
2	Amplitude corrections
3	Automatic gain control (AGC)
4	Time muting
5	Normal Move Out (NMO) correction
6	Common midpoint/ensemble stack

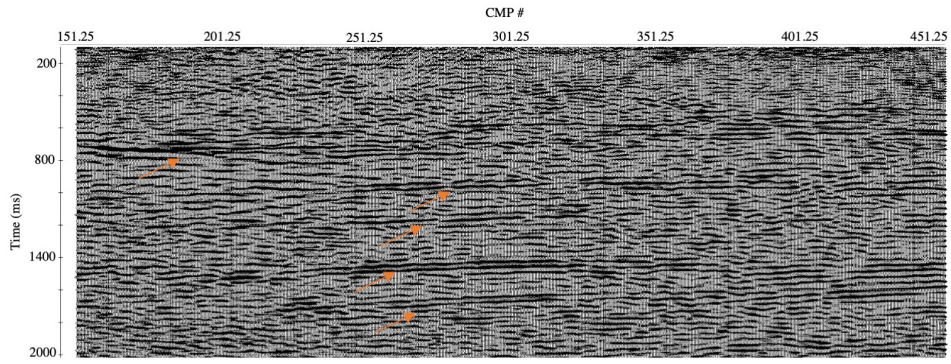

Figure 5.8: Preliminary unmigrated stacked section using a constant velocity of 350 m/s using raw reflection dataset after surgical muting of the surface waves. The orange arrows point to strong reflectors.

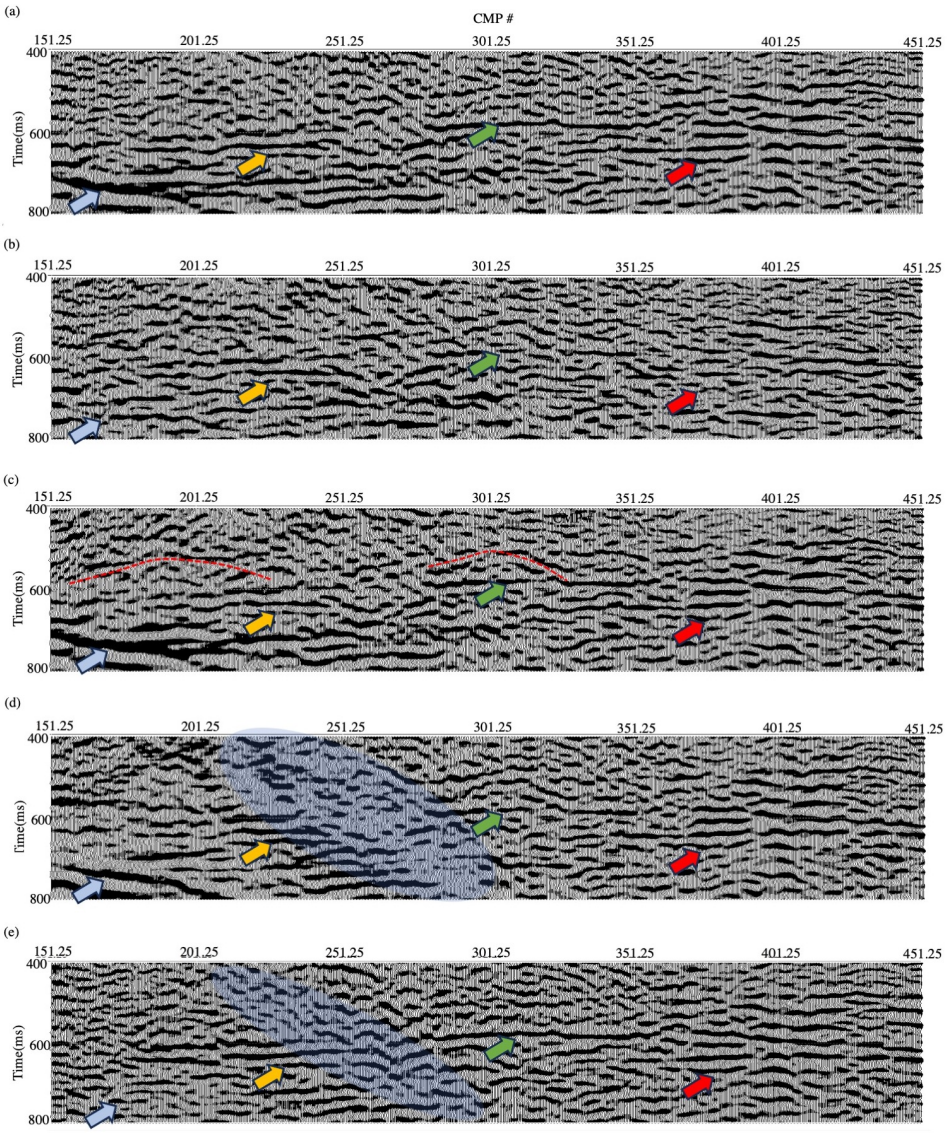

Figure 5.9: Preliminary unmigrated stacked section using a constant velocity of 350 m/s zoomed in 400-800 ms, (a) using raw reflection dataset after surgical muting of surface waves ("SS-muteS"), (b) after the RISS, (c) after the RISS using the muted SI results (RISS-muteR), (d) using the data as (a) but after the RISS ("RISS-muteS"), (e) after fk filtering ("SS-fk"). The colored arrows point to strong reflectors and the blue ellipses highlight artefacts.

5.5. DISCUSSION

We presented a comparison of different approaches for surface-wave suppression applied to the land seismic dataset from Scheemda, Groningen province: surgical muting, fk filtering, the RISS, the RISS-muteR, and the RISS-muteS.

By comparing unmigrated time sections, we showed that for our dataset, surgically muting seems like a convenient way to remove surface waves, but this method does not adequately remove the surface-wave energy, as it overlaps with useful reflections and scattered arrivals. Additionally, weak reflections and scattered arrivals covered by surface waves might also be muted, as demonstrated by Konstantaki et al. (2015).

The other usually applied suppression technique -fk filtering- could cause the rise of artefacts, as it is challenging to define correct parameters for frequency and wave number for all common-source gathers. In contrast, the RISS technique can effectively suppress surface waves without any prior information as it is data-driven.

By comparing three approaches for the RISS, we showed that the RISS using muted deeper reflections after the retrieval of the surface waves with SI yields better results. For our dataset, RISS with two iterations were sufficient to achieve the desired results. However, for different datasets, repeating the procedure for more than two iterations and preserving deeper reflections in SI results can be beneficial.

Through a comparison of dispersion curves obtained from the results of SI with common-source gathers as depicted in Figure 5.10, it is apparent that higher modes of surface waves cannot be accurately kinematically retrieved using SI. Consequently, effectively suppressing these higher modes from the dataset poses a significant challenge. As highlighted by Halliday and Curtis (2008), modal separation emerges as a crucial step before applying SI to ensure the correct kinematic retrieval and consecutive suppression of higher modes with minimal error. On the other hand, the RISS can help suppress higher modes, as we showed. This happens as during each iteration the strongest present surface-wave mode is retrieved and adaptively suppressed, which could effectively be seen as step-wise modal separation.

For the adaptive subtraction of the RISS, we have to determine the time and spacing window and filter length. We determined these values carefully by examining different parameters. However, Balestrini et al. (2020) demonstrated that changing the time and space window sizes does not generate appreciable differences. They observed that increasing the filter length produces undesired artefacts at earlier times. Therefore, for different datasets, defining a proper filter length can be crucial.

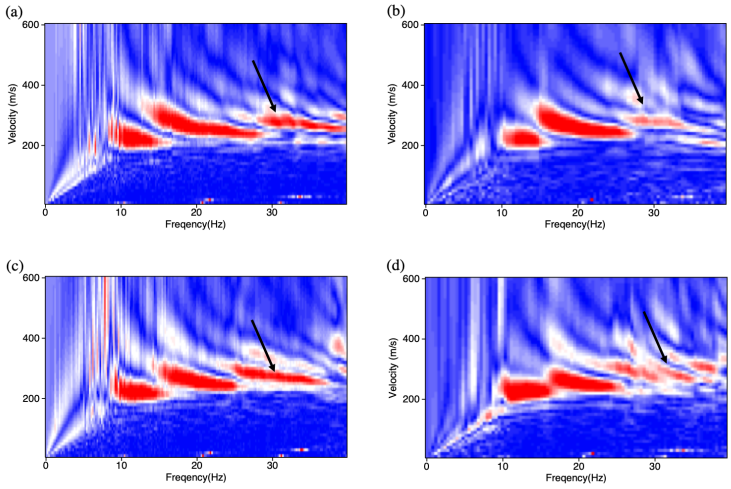

Figure 5.10: Dispersion curves, (a) for an active source at 320.5 m, (b) the virtual source at 320 m, (c) same as (a) but for the active source at 430.5 m, and (d) same as (b) but for the virtual source at 430 m. The black arrows point to the higher modes of surface waves.

5.6. CONCLUSION

We studied the application of seismic interferometry (SI) for surface-wave suppression using a 2D reflection dataset acquired in Scheemda, Groningen province, the Netherlands. We applied SI to retrieve dominant surface waves between receivers while minimising the retrieved reflection energy. The retrieved dominant surface waves were then adaptively subtracted from the original data. We showed that applying these two steps two times, i.e., recursively, resulted in a fully data-driven effective suppression of surface waves.

We compared stacked sections obtained through the recursive interferometric surface wave suppression with stacked sections where the surface waves were suppressed using frequency-wavenumber filtering and surgical muting. We showed that the obtained time section after the second iteration of recursive interferometric surface wave suppression yielded better results in terms of clearer and more continuous reflections especially when the bottom-muted SI result was used. This technique can be effective for enhancing the resolution of reflections for subsurface investigations.

5.7. DATA AVAILABILITY

The field reflection dataset used in this chapter is available in the 4TU.ResearchData repository at https://doi.org/10.4121/a8553b7e-82ae-4e9b-bc54-2a6b9ca6063c. The dataset is under embargo and becomes available in the repository after September 2026. The codes underlying this chapter are also accessible in the 4TU.ResearchData repository at https://doi.org/10.4121/6271c7d3-f931-49e9-b2b0-2d05eef7d3ae. The codes are under embargo and becomes available in the repository after August 2025.

REFERENCES

Alá'i, R., & Verschuur, D. (2003). Simultaneous adaptive least-squares subtraction of multiples. *European Association of Geoscientists & Engineers*, Article cp-6-00176, 1–4. https://doi.org/10.3997/2214-4609-pdb.6.P193

Balestrini, F., Draganov, D., Malehmir, A., Marsden, P., & Ghose, R. (2020). Improved target illumination at Ludvika mines of Sweden through seismic-interferometric surface-wave suppression. *Geophysical Prospecting*, *68*(1), 200–213. https://doi.org/10.1111/1365-2478.12890

Halliday, D., & Curtis, A. (2008). Seismic interferometry, surface waves and source distribution. *Geophysical Journal International*, *175*, 1067–1087. https://doi.org/10.1111/j.1365-246X.2008.03918.x

Halliday, D., Curtis, A., Robertsson, J. O., & van Manen, D. J. (2007). Interferometric surface-wave isolation and removal. *Geophysics*, *72*(5), A69–A73. https://doi.org/10.1190/1.2761967

Halliday, D., Curtis, A., Vermeer, P., Strobbia, C., Glushchenko, A., van Manen, D.-J., & Robertsson, J. O. (2010). Interferometric ground-roll removal: Attenuation of scattered surface waves in single-sensor data. *Geophysics*, *75*(2), SA15–SA25. https://doi.org/10.1190/1.3360948

Konstantaki, L., Draganov, D., Ghose, R., & Heimovaara, T. (2015). Seismic interferometry as a tool for improved imaging of the heterogeneities in the body of a landfill. *Journal of Applied Geophysics*, *122*, 28–39. https://doi.org/https://doi.org/10.1016/j.jappgeo.2015.08.008

Kruiver, P. P., van Dedem, E., Romijn, R., de Lange, G., Korff, M., Stafleu, J., Gunnink, J. L., Rodriguez-Marek, A., Bommer, J. J., van Elk, J., & Doornhof, D. (2017). An integrated shear-wave velocity model for the Groningen gas field, the Netherlands. *Bulletin of Earthquake Engineering*, *15*, 3555–3580. http://link.springer.com/10.1007/s10518-017-0105-y

Liu, J., Draganov, D., & Ghose, R. (2018). Seismic interferometry facilitating the imaging of shallow shear-wave reflections hidden beneath surface waves. *Near Surface Geophysics*, *16*(3), 372–382. https://doi.org/10.3997/1873-0604.2018013

Noorlandt, R., Drijkoningen, G., Dams, J., & Jenneskens, R. (2015). A seismic vertical vibrator driven by linear synchronous motors. *Geophysics*, *80*(2), EN57–EN67. https://doi.org/10.1190/GEO2014-0295.1

Verschuur, D. J., Berkhout, A. J., & Wapenaar, C. P. A. (1992). Adaptive surface-related multiple elimination. *Geophysics*, *57*(9), 1166–1177. https://doi.org/10.1190/1.1443330

Verschuur, D. (2013). *Seismic multiple removal techniques - past, present and future*. European Association of Geoscientists & Engineers (EAGE). https://app.knovel.com/hotlink/toc/id:kpSMRTPPF2/seismic-multiple-removal/seismic-multiple-removal

Wapenaar, K., Draganov, D., Snieder, R., Campman, X., & Verdel, A. (2010). Tutorial on seismic interferometry: Part 1 — basic principles and applications. *Geophysics*, *75*, 75A195–75A209. https://doi.org/10.1190/1.3457445

Yilmaz, Ö. (2001). *Seismic data analysis*. Society of Exploration Geophysicists. https://doi.org/10.1190/1.9781560801580

6

APPLICATION OF MARCHENKO-BASED ISOLATION TO A LAND S-WAVE SEISMIC DATASET

The Marchenko method is capable of estimating Green's functions between the surface of the Earth and arbitrary locations in the subsurface. These Green's functions can then be used to redatum wavefields to a deeper level in the subsurface. As a result, the Marchenko method enables the isolation of the response of a specific layer or package of layers, free from the influence of the overburden and underburden.

In this study, we apply the Marchenko-based isolation technique to land S-wave seismic data acquired in the Groningen province, the Netherlands. We apply the technique for combined removal of the overburden and underburden. Our results indicate that this approach enhances the resolution of reflection data. These enhanced reflections can be utilised for imaging and monitoring applications.

A summary of this chapter is published as Shirmohammadi, F., Draganov, D., van IJsseldijk, J., Ghose, R., Thorbecke, J., Verschuur, E., & Wapenaar, K. (2024). Application of Marchenko-based isolation to a land seismic dataset. *85th EAGE Annual Conference & Exhibition 2024*, 1-5, https://doi.org/10.3997/2214-4609.202410742, and also the preprint is available as Shirmohammadi, F., Draganov, D., van IJsseldijk, J., Ghose, R., Thorbecke, J., Verschuur, E., & Wapenaar, K. (2023). Application of the Marchenko method to a land seismic dataset. *arXiv preprint arXiv:2304.09956*, 1-26, https://doi.org/10.48550/arXiv.2304.09956.

6.1. INTRODUCTION

The Marchenko method – a data-driven method – provides a tool for extracting information about the subsurface properties of the Earth. The Marchenko method retrieves Green's functions in the subsurface from seismic reflection data at the surface, and then these Green's functions can be used to redatum wavefields from the surface to arbitrary locations in the subsurface; a virtual source or receiver can be created at any point inside the medium of interest. This method employs reflection data from sources and receivers at the surface and an estimation of the first arrival, from a point in the subsurface from which we want to redatum to the surface, which can be modelled in a macro-velocity model (Slob et al., 2014; Wapenaar et al., 2014).

In recent years, there has been a significant progress in developing the Marchenko method and extending its applicability, for instance, for isolating the response of a specific subsurface layer without interference from the overburden and/or underburden. For an easier comparison with the original reflection data, the result of the Marchenko method can be extrapolated back to the surface (van der Neut and Wapenaar, 2016). This application results in a reflection response with sources and receivers at the surface and with fewer internal multiples. This allows for more accurate characterisation of the properties of the target layer and can be particularly useful in target-oriented imaging and monitoring. Wapenaar and van IJsseldijk (2021) introduced the Marchenko-based isolation to identify the reservoir response from a seismic reflection survey by applying a two-step approach for removing the overburden and underburden interferences. Van IJsseldijk et al. (2023) showed that using this application effectively isolates the target response, which can then be used to extract more precisely the local time-lapse changes in a reservoir. The Marchenko application for isolating a target response has been successfully applied to marine time-lapse datasets of the Troll Field for monitoring reservoir changes (van IJsseldijk et al., 2024).

As with any other method, the Marchenko method has some limitations. For its standard application, evanescent waves are ignored, the medium of interest is assumed to be lossless, and it is sensitive to inaccuracies in the reflection response. These facts can pose challenges, particularly for field datasets. Nevertheless, the method has been successfully applied to several marine field datasets for imaging and monitoring (Ravasi et al., 2016; Jia et al., 2018; Staring et al., 2018; Mildner et al., 2019; Zhang and Slob, 2020; van IJsseldijk et al., 2024). These advances have opened up a new opportunity for applying it to land seismic data. However, applying the method to land seismic data is more problematic, not only because a reflection dataset free of surface waves and surface-related multiples is required, but also because the recorded data are inherently elastic.

Here, we aim to apply the Marchenko-based isolation method to isolate the target response, removing the overburden and underburden using an SH-wave seismic dataset acquired close to the town of Scheemda, Groningen province, the Netherlands. The province of Groningen has been experiencing induced seismicity due to gas production since 1963 (Muntendam-Bos et al., 2022). Down to 800 m depth, the subsurface in Groningen comprises a sequence of soft, unconsolidated sediments, mainly composed of sand and clay (Kruiver et al., 2017). Achieving an accurate depiction of the geometry and characteristics of these layers is crucial for precise earthquake studies. However, as known from Cone Penetration Testing (CPT) data, the first 30 meters of this site con-

sist of alternating layers capable of generating strong internal multiples, interfering with the response of all layers in the subsurface. Additionally, the deeper layers may generate arrivals that interfere with multiple reflections from the shallower layers. We acquired the reflection dataset specifically in this region to showcase the effectiveness of the Marchenko-based isolation method on land data and to enhance the visualisation of the reflection dataset in this region.

In the following section, we first review the method. Next, we describe the seismic acquisition parameters and the steps for preparing the input data for the Marchenko application. Finally, we discuss the results and how this study enables future utilisation of the method, particularly for land-based applications.

6.2. METHOD

Using the Marchenko method, we aim to isolate responses from a target layer by eliminating undesired events, including primaries and multiples, originating from both the overburden and underburden. To achieve this, the medium is divided into three units: overburden $\langle a \rangle$, target zone $\langle b \rangle$, and underburden $\langle c \rangle$, as shown in Figure 6.1. In the first step, the extrapolated Green's functions are determined with a focal level situated between the overburden $\langle a \rangle$ and the target zone $\langle b \rangle$ by using the focusing functions.

Next, the overburden is removed, and the reflection response of the combined target zone $\langle b \rangle$ and underburden $\langle c \rangle$ is retrieved by applying SI by multidimensional deconvolution (MDD, Broggini et al., 2014) with the extrapolated Green's functions. In the following step, the newly obtained reflection response is used to retrieve the extrapolated focusing functions between the target zone $\langle b \rangle$ and the underburden $\langle c \rangle$. These retrieved focusing functions are then used to remove the underburden using SI by MDD, effectively isolating the response of the target layer $\langle b \rangle$.

In the following subsections, we present the representations of Green's functions and then demonstrate how to isolate the responses of the target layer by eliminating the effects of the overburden and underburden.

6.2.1. GREEN'S FUNCTIONS REPRESENTATION

The Marchenko method relies on two equations that relate the Green's functions and the focusing functions, derived from the one-way reciprocity theorems of the correlation and convolution types (Slob et al., 2014; Wapenaar et al., 2014; Wapenaar et al., 2021). Focusing functions are wavefields specifically designed to focus the wave field at a particular location within the subsurface. These functions are defined in a truncated medium, which matches the actual medium above the chosen focal level and is homogeneous below it. In the actual medium, focusing functions enable the wavefield to converge at the focal point, thereby facilitating the retrieval of a virtual source that generates Green's functions between the focal depth and the surface. The Marchenko method is a data-driven method that only requires the reflection responses at the surface and the direct arrivals of the focusing functions which can be estimated using a macro velocity model of the subsurface.

Meles et al. (2016) and Van der Neut and Wapenaar (2016) proposed extrapolating the virtual sources and receivers, obtained through Marchenko redatuming, back to the

surface. This approach ensures that the travel times of events in the processed response remain consistent with those in the original reflection data, allowing for easier comparison of results before and after applying the Marchenko method. Both the focusing and Green's functions are extrapolated using the direct arrival of the transmission response from the focal depth to the surface (van der Neut and Wapenaar, 2016), ensuring that the coordinates of all functions are located at the acquisition surface, S_0. Following this approach, the coupled Marchenko extrapolated representations are defined as (Wapenaar et al., 2021; van IJsseldijk et al., 2024):

$$U^{-,+}(\mathbf{x}_R,\mathbf{x}'_S,t)+v^{-}(\mathbf{x}_R,\mathbf{x}'_S,t)=\int_{S_0}R(\mathbf{x}_R,\mathbf{x}_S,t)*v^{+}(\mathbf{x}_S,\mathbf{x}'_S,t)\,d\mathbf{x}_S, \tag{6.1}$$

$$U^{-,-}(\mathbf{x}_R,\mathbf{x}'_S,-t)+v^{+}(\mathbf{x}_R,\mathbf{x}'_S,t)=\int_{S_0}R(\mathbf{x}_R,\mathbf{x}_S,-t)*v^{-}(\mathbf{x}_S,\mathbf{x}'_S,t)\,d\mathbf{x}_S \tag{6.2}$$

which relate the extrapolated Green's function $U^{-,\pm}$ to the extrapolated focusing functions ($v^{\pm}$) using the reflection response $R(\mathbf{x}_R,\mathbf{x}_S,t)$ at the acquisition surface (S_0). Here, $\mathbf{x}_R$ and $\mathbf{x}_S$ describe the receiver and source positions at the surface, respectively, and the superscripts $(-)$, $(\pm)$ of the extrapolated Green's functions represent an up-going receiver field from an up- $(-)$ or down-going $(+)$ source field, respectively. The asterisk $(*)$ denotes temporal convolution.

Given that R is known, Equations 6.1 and 6.2 involve four unknowns:($U^{-,-}$, $U^{-,+}$, v^{-}, and v^{+}). To solve these equations, a window function is applied to suppress the extrapolated Green's functions. This approach relies on the fact that the extrapolated focusing functions and Green's functions are separable in time (van der Neut and Wapenaar, 2016). This causality constraint can be applied after estimating the two-way travel time between the focal depth and the surface, which is obtained by convolving the transmission response with itself. The transmission response can be derived from a smooth macro velocity model using an Eikonal solver. By restricting Equations 6.1 and 6.2 to the interval from t=0 s to the calculated two-way travel time, the Green's functions on the left-hand side vanish. This simplifies the system to two equations with two unknowns (the extrapolated focusing functions), which can be solved iteratively (Thorbecke et al., 2017) or through inversion (van der Neut et al., 2015). Once the focusing functions are found, the extrapolated Green's functions follow from Equations 6.1 and 6.2 without the time restriction. A detailed derivation of the Marchenko method is beyond the scope of this paper; however, a comprehensive derivation and background can be found in Wapenaar et al. (2021).

6.2.2. OVER- AND UNDERBURDEN REMOVAL

The isolated responses of the target layer are retrieved through a two-step procedure. First, the overburden is removed, followed by the underburden removal. As introduced above, the medium is divided into as three units: $\langle a\rangle$ for the overburden, $\langle b\rangle$ for the target layer, and $\langle c\rangle$ for the underburden, as shown in Figure 6.1. In the first step, for the overburden removal, a focal level is selected between the overburden $\langle a\rangle$ and the target zone $\langle b\rangle$, and Equations 6.1 and 6.2 are employed to determine the extrapolated Green's functions using the regular reflection responses (R_{abc}). For the overburden removal, the

retrieved extrapolated Green's functions are employed to retrieve the reflection response isolated from the overburden interferences using (Wapenaar et al., 2021, van IJsseldijk, 2023):

$$U^{-,+}_{a|bc}(\mathbf{x}_R,\mathbf{x}'_S,t) = -\int_{S_0} U^{-,-}_{a|bc}(\mathbf{x}_R,\mathbf{x}'_R,t) * R_{bc}(\mathbf{x}'_R,\mathbf{x}'_S,t)\,d\mathbf{x}'_R, \tag{6.3}$$

where, $U^{-,\pm}_{a|bc}$ represents the extrapolated Green's functions. The vertical line in the subscript indicates the location of the focal level, i.e., between the overburden $\langle a\rangle$ and the target zone and underburden $\langle bc\rangle$. Using Equation 6.3, the reflection response R_{bc} is retrieved employing SI by MDD. The retrieved R_{bc} contains all primary and multiple reflections from the target zone $\langle b\rangle$ and underburden $\langle c\rangle$ but it is devoid of overburden interactions from $\langle a\rangle$. Additionally, the coordinates $\mathbf{x}'_R$ and $\mathbf{x}'_S$ are situated at the surface, owing to the utilisation of extrapolated Green's functions (van IJsseldijk et al., 2023).

For the next step, which is the underburden removal, this new reflection response (R_{bc}) can be utilised to retrieve the extrapolated focusing functions for a focal level between the target zone $\langle b\rangle$ and the underburden $\langle c\rangle$ using Equations 6.1 and 6.2 (Wapenaar and Staring, 2018, van IJsseldijk et al., 2024). Then, to remove the underburden, we employ the following relation between the extrapolated focusing functions and the reflection response of the target (R_b):

$$v^{-}_{b|c}(\mathbf{x}_R,\mathbf{x}'_S,t) = \int_{S_0} v^{+}_{b|c}(\mathbf{x}_R,\mathbf{x}'_R,t) * R_b(\mathbf{x}'_R,\mathbf{x}'_S,t)\,d\mathbf{x}'_R. \tag{6.4}$$

The subscript $b|c$ indicates that the extrapolated focusing functions have been obtained from the reflection response without overburden interaction, utilising a focal depth between the target zone $\langle b\rangle$ and underburden $\langle c\rangle$. Once again, the isolated reflection response (R_b) can be retrieved from this equation through SI by MDD. Effectively, the target zone response has now been isolated, consisting of the reflections (primaries and multiples) from inside it (van IJsseldijk et al., 2024). Figure 6.1 shows this two-step procedure for removing the overburden and underburden using the Marcenko-based isolation.

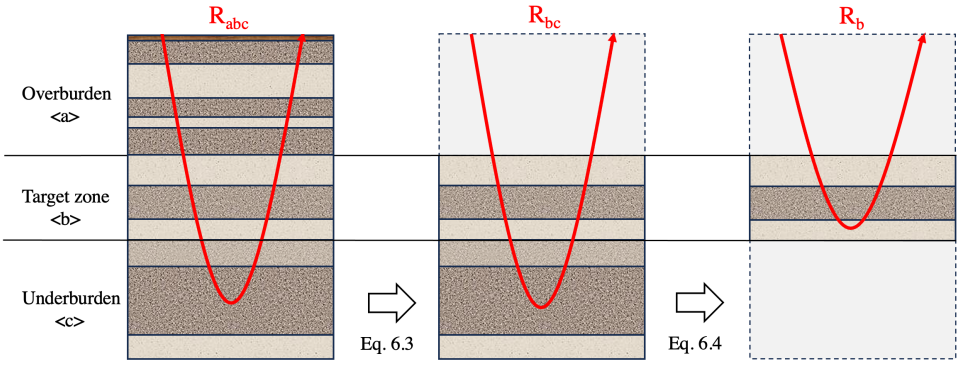

Figure 6.1: Visual representation of the concept of Marchenko-based isolation. The medium is segmented into three units: overburden $\langle a\rangle$, target zone $\langle b\rangle$, and underburden $\langle c\rangle$. The initial step involves the removal of the overburden from the response, as outlined in Equation 6.3. Following this, the response of the underburden is removed using Equation 6.4 (Adapted from van IJsseldijk et al., 2024).

6.3. SEISMIC DATA ACQUISITION

We use the same seismic reflection data along a 2D line close to the town of Scheemda in the Groningen province of the Netherlands as described in Section 5.3 of Chapter 5. Figures 6.2a shows the geometry of the line. Figure 6.2b shows two examples of the CPT data from this site. To apply the Marchenko method, we then use the data recorded by the crossline horizontal component of the geophones. Because of the orientation of the sources and the receivers, and assuming no scattering from the crossline direction, the SH-waves we record are generally decoupled from the compressional and vertically polarised S-waves. This makes the dataset more convenient for applying the Marchenko method. Three examples of common-source gathers at different source positions are shown in Figure 6.3.

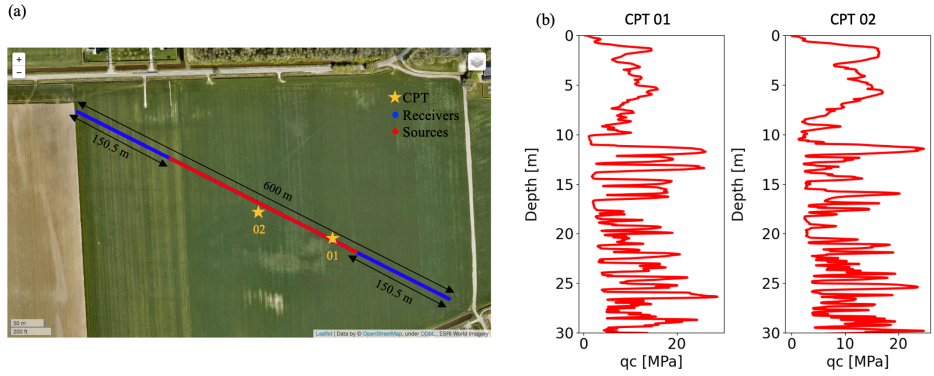

Figure 6.2: (a) The geometry of the reflection line. (b) Two examples of cone penetration test data.

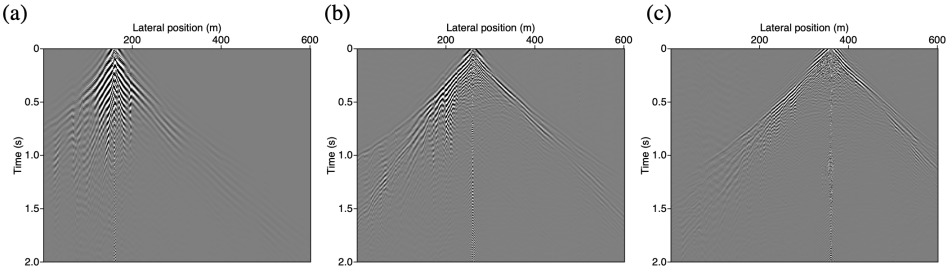

Figure 6.3: Raw common-source gathers for active sources at lateral positions (a) 165.5 m, (b) 260.5 m, and (c) 360.5 m.

6.4. DATA PRE-PROCESSING

The raw seismic reflection data cannot directly be used by the Marchenko method because when the method uses these data, it does not converge to a solution. As data pre-processing, first, we apply source-signature deconvolution as using high-resolution zero-phase reflection responses as input is crucial for the Marchenko method.

In seismic land surveys with sources and receivers at the surface, the surface waves are most of the times dominant and mask reflections. This is also the case for our data. To eliminate surface waves, we apply surgical muting in the time domain and then employ bandpass filtering between 30 Hz and 100 Hz based on the power spectrum of the common-source gathers. We also compare this result with the result using data after RISS-muteR for surface-wave suppression which we showed it yielded better results as shown in Chapter 5.

The subsequent steps involved in preparing the reflection data for applying the Marchenko method represent amplitude corrections. First, we correct the amplitudes for recording a 2D line in a 3D world. The effects of having geometric spreading in a 3D world while applying a 2D Marchenko scheme are corrected by applying a time-dependent gain on the data. This gain is approximately equal to $\sqrt{t}$ (Helgesen and Kolb, 1993; Brackenhoff et al., 2019). After that, we correct for absorption effects and an overall amplitude mismatch that, for example, is related to the source signature. This is achieved by minimizing a cost function as described in Brackenhof (2016). Different gains and linear factors are considered to find an optimal correction factor (van IJsseldijk, 2023).

Our survey has more receivers positions than source positions. On the other hand, the Marchenko-method application uses the same number of sources and receivers due to the requirement for square matrices in the calculations. Therefore, we constrain our receivers to the extent and number of the sources, i.e., to the range 150 − 450 m with 2.0 m spacing.

Figures 6.4a and 6.4c show two common-source gathers after the application of the above-mentioned pre-processing steps. In these figures, it is evident that some pronounced surface waves persist at receivers positioned laterally between 150 m and 220 m, as indicated by the white arrows. Additionally, when comparing the common-source gathers shown in Figure 6.3, variations in the frequency content of the surface waves become apparent for sources located at lateral positions 150 m − 220 m. This variation may occur due to local scattering in the shallow subsurface. Therefore, we further limit our sources and receivers to the range 220 m − 450 m. Moreover, we see from the pre-processed gathers that the traces closest to the source location appear to have too strong amplitudes, i.e., are influenced by the source, which would result in difficulties during the inversion. Thus, we mute the 20 nearest traces around each source location, and then finally we apply a bandpass filter between 30 Hz and 100 Hz. Figures 6.4b and 6.4d show the common-source gathers from Figures 6.4a and 6.4c, respectively, after all pre-processing steps, showcasing enhancement in the visibility of reflections. Additionally, we select only the earliest 1.6 s, as our primary focus lies in improving reflections up to this time. These processed data are then utilised as input for the Marchenko-based isolation technique.

As discussed in Section 6.2, we also require a smooth velocity model of the subsur-

face below the acquisition line to separate the focusing functions from the Green's functions by estimating the two-way travel time between the surface and the focal depth. We obtain the smooth velocity model by NMO analysis applied to CMP gathers.

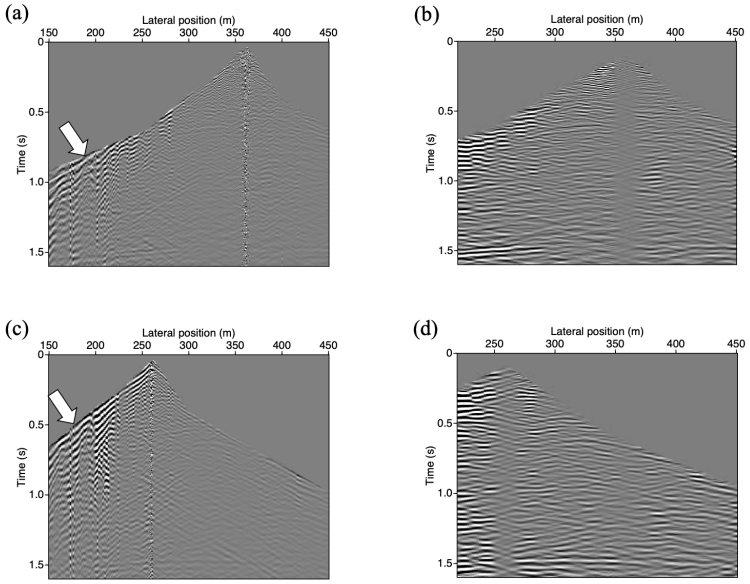

Figure 6.4: Common-source gathers: (a) after the initial pre-processing steps and (b) after the final pre-processing steps for a source at a lateral position at 360.5 m. (c) and (d) same as (a) and (b), respectively, but for a source at 260.5 m. The white arrows show strong surface waves at the receiver positions at 150 – 220 m.

6.5. RESULTS

After completing the pre-processing steps, we employ the processed reflection data to extract the Green's functions and isolate responses of the target region using the Marchenko-based isolation technique with one iteration. To account for both overburden and underburden effects, we employ the two-step procedure explained in Section 6.2. In the first step, we eliminate the overburden effect by choosing a focal depth of 30 m. Subsequently, using the results obtained from the first step, we eliminate the underburden effect by choosing a focal depth of 270 m. This two-step approach leaves the isolated response of the target region between 30 m and 270 m depth. Figure 6.5 shows two common-source gathers before and after the Marchenko-based isolation. By comparing the common-source gathers before (Figures 6.5a and 6.5c) and after the Marchenko-based isolation (Figures 6.5b and 6.5d), it is evident that the resolution of some reflections is enhanced, as indicated by the cyan, yellow, and red arrows.

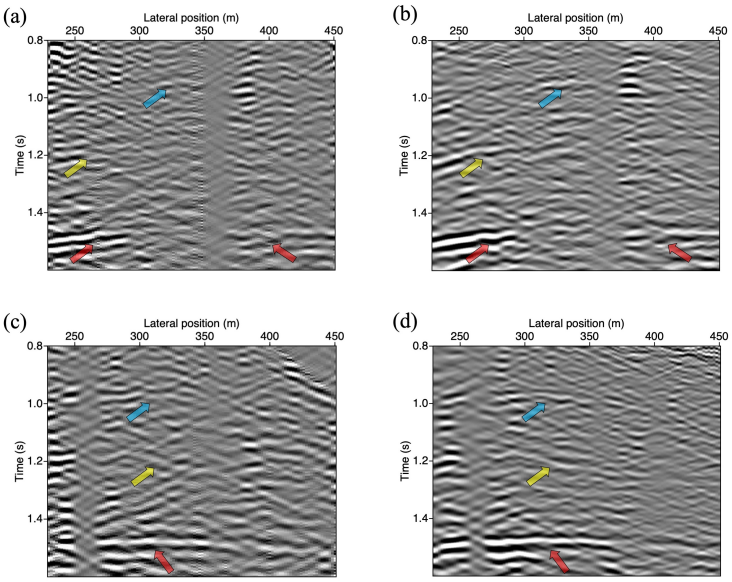

Figure 6.5: A common-source gather for a source at 360.5 m (a) before and (b) after the Marchenko-based isolation. (c) and (d) same as (a) and (b), respectively, but for a source at 260.5 m. The cyan, yellow, and red arrows indicate reflections. Same bandpass filtering between 30 Hz and 100 Hz applied for better comparison.

To facilitate a further comparison of the results, we perform NMO correction and stacking using CMP gathers for both the regular and the Marchenko-isolated responses. For the NMO correction and stacking, we use a constant velocity of 350 m/s, which results in optimal stacking. We then apply an AGC to aid the visual comparison. The stacked sections for both the regular and Marchenko-based isolated responses are shown in Figure 6.6.

The stacked section obtained from the Marchenko-based isolated responses in Figure 6.6b is significantly cleaner than the stacked section using the regular reflection response (with the same spatial extend)in Figure 6.6a. Moreover, the Marchenko-isolated stacked section exhibits more continuity, helping interpreting the data better. The events marked with cyan, yellow, orange, and red arrows indicate improvements in the stacked section of the Marchenko-based isolation.

To assess the individual effects of the overburden and underburden on the final result, we perform overburden and underburden removal separately. Figure 6.6c shows the stacked section after overburden removal, while Figure 6.6d shows the stacked section after underburden removal. By comparing Figure 6.6c and Figure 6.6d with Figure 6.6b, it becomes evident that most of the interaction originates from the overburden. The removal of the underburden does not improve the interpretability of the stacked sections, as enhancements are expected for arrivals after 1.42 s for a focal depth of 270 m using the estimated average velocity of 380 m/s from the smooth velocity model. This is likely due to small velocity variation in the underburden and attenuation of the reflected S-waves from the deeper layers. Additionally, the noise observed in Figure 6.6d may be attributed

to the influence of the overburden.

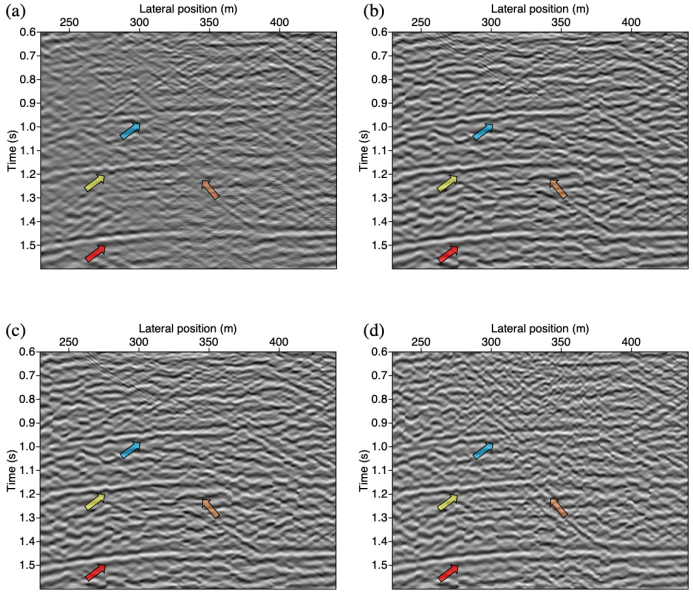

Figure 6.6: The stacked sections obtained from (a) the regular reflection response and (b) the reflection response after the Marchenko-based isolation for overburden and underburden removal, (c) same as (b) but after only overburden removal, (d) same as (b) but after only underburden removal. The colour-coded arrows indicate reflections.

To better visualise the shallow part of the section, we further zoom in from 0.6 s to 1.0 s, see Figure 6.7. The geology in the top 30 m at this site, known from the CPT profiles (Figure 6.2c), comprises alternating clay and sand layers that contribute to the generation of internal multiples in this shallow section. Comparing the stacked section before Marchenko-based isolation in Figure 6.7a with the stacked section after Marchenko-based isolation in Figure 6.7b suggests a potential elimination of such internal multiples originating from the overburden down to 30 m in our case. Similar to the deeper reflectors, these shallow reflectors appear clearer and more continuous, as indicated by the colour-coded arrows.

In Chapter 5, we demonstrated that for the same reflection dataset, utilising RISS-muteR for surface-wave suppression results in more detailed features in the shallow subsurface. To evaluate whether there is any improvement in the results of Marchenko-based isolation by utilising data with RISS, we apply the same pre-processing steps discussed in Section 6.4 to the data after RISS-muteR. Then, we apply the Marchenko-based isolation to remove the overburden and underburden for the same focal depths at 30 m and 270 m, respectively. As we previously observed in chapter 5 a substantial improvement in the shallower part, we focus here on the shallower section, as shown in Figure 6.7c. Upon comparison with Figures 6.7c and 6.7b, we observe the enhanced reflections but with more clarity, exemplified by the events indicated by the white and green

arrows. Moreover, there are fewer artefacts, likely from surface waves, as indicated by the black ellipse.

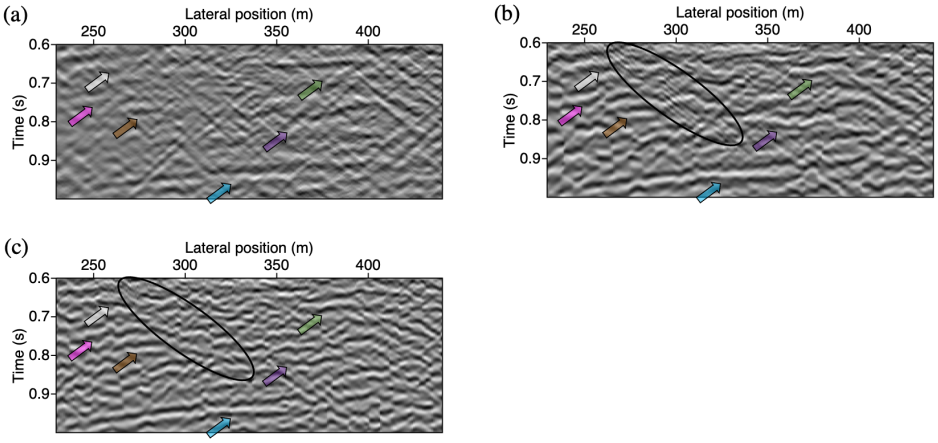

Figure 6.7: Stacked sections, zoomed in between 0.6 s and 1.0 s, obtained using (a) the regular reflection response, (b) the reflection response after Marchenko-based isolation for overburden and underburden removal, and (c) similar to (b) but using data after surface-wave suppression with RISS-muteR instead of surgical muting. The colour-coded arrows indicate reflectors. The black ellipse highlights potential artefacts from surface waves that are suppressed in (c).

6.6. DISCUSSION

As demonstrated in the preceding section, the application of the Marchenko-based isolation to the target zone between 30 m and 270 m yields promising outcomes - it enhances the quality of the reflection data and provides a clearer image of the target zone with more continuous reflectors. Even though we observe clear improvements in the reflection-data resolution, there are potential options for further enhancement in future studies but also some points to discuss.

First, the method is intentionally designed to minimise the reliance on a priori information, utilising only a smooth version of the velocity model and the recorded reflection responses. However, a careful processing step is crucial to ensure a reflection response free from the surface waves and surface-related multiples. In this study, we suppressed surface waves using surgical muting in the time domain and frequency filtering. We also showed the results after the RISS-muteR, which shows clearer and more continuous reflections in the shallow part. So, it is advantageous to eliminate all surface waves using techniques such as SI for surface-wave suppression (Chapter 5 and Balestrini et al., 2020).

Second, one significant challenge in applying the Marchenko method to field data lies in the amplitude-scaling requirements on the reflection data. We tried to overcome amplitude mismatches by applying three gain factors for: geometrical spreading, absorption effects, and an overall scaling. The overall scaling factor has been investigated and tested for marine data (Brackenhof, 2016). As this is an important correction, it

might be useful to investigate the overall scaling specifically for land seismic data and SH-waves.

Third, in this study, we applied the Marchenko-based isolation technique by selecting focal depths at 30 m and 270 m. We observed that the most significant contribution comes from the overburden removal. However, choosing different focal depths with smaller intervals and focusing on the improvement of specific reflections could be valuable for future studies.

Finally, we propose the application of velocity analysis followed by migration, with a subsequent comparison of the migration results. This additional step could contribute to a more comprehensive understanding and improvement of the Marchenko-based isolation technique.

6.7. CONCLUSION

We showed the result of applying the Marchenko-based isolation technique to SH-wave land seismic data that we acquired in the Groningen province, the Netherlands. Land data are intrinsically elastic, known for dominant surface waves and low signal-to-noise ratio, and hence pose a challenge for the Marchenko method, which requires high-quality reflection data.

After careful implementation of surface-wave suppression, selection of the same spatial extent of sources and receivers, and scaling-factor corrections as pre-processing steps, we retrieved the extrapolated Green's functions, and the isolated target responses after the combined removal of the overburden and the underburden. We showed that the resulting stacked section is cleaned up, providing a better image of the target zone compared to the stacked regular reflection response. Our results open the door for future applications of the Marchenko method to land seismic datasets, particularly in time-lapse monitoring of deeper structures, for example for CO_2 and H_2 storage, or for shallow applications such as monitoring waste management and hydrology/water tables.

6.8. DATA AVAILABILITY

Codes associated with this chapter are available and can be accessed via the following URL: https://gitlab.com/geophysicsdelft/OpenSource in the "vmar" folder. More explanation can be found in van IJsseldijk et al. (2023).

REFERENCES

Balestrini, F., Draganov, D., Malehmir, A., Marsden, P., & Ghose, R. (2020). Improved target illumination at Ludvika mines of Sweden through seismic-interferometric surface-wave suppression. *Geophysical Prospecting*, *68*(1), 200–213. https://doi.org/10.1111/1365-2478.12890

Brackenhof, J. (2016). *Rescaling of incorrect source strength using Marchenko redatuming* [M.Sc. thesis]. Delft University of Technology [Available at http://resolver.tudelft.nl/uuid:0f0ce3d0-088f-4306-b884-12054c39d5da].

Brackenhoff, J., Thorbecke, J., & Wapenaar, K. (2019). Virtual sources and receivers in the real earth: Considerations for practical applications. *Journal of Geophysical*

Research: Solid Earth, *124*(11), 11802–11821. https://doi.org/https://doi.org/10.1029/2019JB018485

Broggini, F., Wapenaar, K., van der Neut, J., & Snieder, R. (2014). Data-driven green's function retrieval and application to imaging with multidimensional deconvolution. *Journal of Geophysical Research: Solid Earth*, *119*(1), 425–441. https://doi.org/https://doi.org/10.1002/2013JB010544

Helgesen, J., & Kolb, P. (1993). Multi-offset acoustic inversion of a laterally invariant medium: Application to real data. *Geophysical Prospecting*, *41*(5), 517–533. https://doi.org/https://doi.org/10.1111/j.1365-2478.1993.tb00868.x

Jia, X., Guitton, A., & Snieder, R. (2018). A practical implementation of subsalt marchenko imaging with a gulf of mexico data set. *Geophysics*, *83*(5), S409–S419. https://doi.org/10.1190/geo2017-0646.1

Kruiver, P. P., van Dedem, E., Romijn, R., de Lange, G., Korff, M., Stafleu, J., Gunnink, J. L., Rodriguez-Marek, A., Bommer, J. J., van Elk, J., & Doornhof, D. (2017). An integrated shear-wave velocity model for the Groningen gas field, the Netherlands. *Bulletin of Earthquake Engineering*, *15*, 3555–3580. http://link.springer.com/10.1007/s10518-017-0105-y

Meles, G. A., Wapenaar, K., & Curtis, A. (2016). Reconstructing the primary reflections in seismic data by Marchenko redatuming and convolutional interferometry. *Geophysics*, *81(2)*, Q15–Q26. https://doi.org/10.1190/geo2015-0377.1

Mildner, C., Broggini, F., da Costa Filho, C. A., & Robertsson, J. O. (2019). Source wavelet correction for practical marchenko imaging: A sub-salt field-data example from the gulf of mexico. *Geophysical Prospecting*, *67*(8), 2085–2103. https://doi.org/https://doi.org/10.1111/1365-2478.12822

Muntendam-Bos, A. G., Hoedeman, G., Polychronopoulou, K., Draganov, D., Weemstra, C., van der Zee, W., Bakker, R. R., & Roest, H. (2022). An overview of induced seismicity in the Netherlands. *Geologie en Mijnbouw/Netherlands Journal of Geosciences*, *101*(2), 1–20. https://doi.org/10.1017/njg.2021.14

Ravasi, M., Vasconcelos, I., Kritski, A., Curtis, A., Filho, C. A. d. C., & Meles, G. A. (2016). Target-oriented Marchenko imaging of a North Sea field. *Geophysical Journal International*, *205*(1), 99–104. https://doi.org/10.1093/gji/ggv528

Slob, E., Wapenaar, K., Broggini, F., & Snieder, R. (2014). Seismic reflector imaging using internal multiples with Marchenko-type equations. *Geophysics*, *79*(2), S63–S76. https://doi.org/10.1190/GEO2013-0095.1

Staring, M., Pereira, R., Douma, H., van der Neut, J., & Wapenaar, K. (2018). Source-receiver Marchenko redatuming on field data using an adaptive double-focusing method. *Geophysics*, *83*(6), S579–S590. https://doi.org/10.1190/geo2017-0796.1

Thorbecke, J., Slob, E., Brackenhoff, J., van der Neut, J., & Wapenaar, K. (2017). Implementation of the Marchenko method. *Geophysics*, *82*, WB29–WB45. https://doi.org/10.1190/GEO2017-0108.1

van IJsseldijk, J. (2023). *Time-lapse monitoring with virtual seismology* [Ph.D. thesis]. Delft University of Technology [Available at https://doi.org/10.4233/uuid:98b24420-219b-438e-a28c-4b12e5f450e6].

van IJsseldijk, J., Brackenhoff, J., Thorbecke, J., & Wapenaar, K. (2024). Time-lapse applications of the Marchenko method on the troll field. *Geophysical Prospecting*, *72*, 1026–1036. https://doi.org/https://doi.org/10.1111/1365-2478.13463

van IJsseldijk, J., van der Neut, J., Thorbecke, J., & Wapenaar, K. (2023). Extracting small time-lapse traveltime changes in a reservoir using primaries and internal multiples after Marchenko-based target zone isolation. *Geophysics*, *88*(2), R135–R143. https://doi.org/10.1190/geo2022-0227.1

van der Neut, J., Thorbecke, J., Wapenaar, k., & Slob, E. (2015). Inversion of the multidimensional Marchenko equation. *77th EAGE Conference and Exhibition 2015: Earth Science for Energy and Environment*, 1–5. https://doi.org/10.3997/2214-4609.201412939

van der Neut, J., & Wapenaar, K. (2016). Adaptive overburden elimination with the multidimensional Marchenko equation. *Geophysics*, *81*(5), T265–T284. https://doi.org/10.1190/GEO2016-0024.1

Wapenaar, K., & van IJsseldijk, J. (2021). Employing internal multiples in time-lapse seismic monitoring, using the Marchenko method. *82nd EAGE Conference and Exhibition 2021*, 1–5. https://doi.org/10.3997/2214-4609.202011576

Wapenaar, K., Brackenhoff, J., Dukalski, M., Meles, G., Reinicke, C., Slob, E., Staring, M., Thorbecke, J., van der Neut, J., & Zhang, L. (2021). Marchenko redatuming, imaging, and multiple elimination and their mutual relations. *Geophysics*, *86*(5), WC117–WC140. https://doi.org/10.1190/geo2020-0854.1

Wapenaar, K., & Staring, M. (2018). Marchenko-based target replacement, accounting for all orders of multiple reflections. *Journal of Geophysical Research: Solid Earth*, *123*(6), 4942–4964. https://doi.org/https://doi.org/10.1029/2017JB015208

Wapenaar, K., Thorbecke, J., van der Neut, J., Broggini, F., Slob, E., & Snieder, R. (2014). Marchenko imaging. *Geophysics*, *79*(3), WA39–WA57. https://doi.org/10.1190/GEO2013-0302.1

Zhang, L., & Slob, E. (2020). A field data example of Marchenko multiple elimination. *Geophysics*, *85*(2), S65–S70. https://doi.org/10.1190/geo2019-0327.1

7

CONCLUSIONS AND FUTURE OUTLOOK

This chapter will conclude the thesis by summarising the most important findings from the preceding chapters and discussing future perspectives and research recommendations derived from the findings presented in this thesis.

7.1. CONCLUSIONS

In Chapter 2, we presented the application of ghost reflections retrieved from SI for layer-specific characterisation of the shallow subsurface. By applying the correlation operator in seismic interferometry (SI), the common ray paths between primary reflections from different depth levels are removed, and ghost (non-physical) reflections are retrieved. Ghost reflections propagate only within specific layers as if observed by a ghost receiver from a ghost source placed just above the specific layers. Using numerically modelled data for a horizontally layered subsurface, we demonstrated the utility of ghost reflections for monitoring specific layers. We showed that ghost reflections are sensitive only to changes within specific target layers, including lateral changes in velocity, velocity gradients in depth, and thickness changes. We applied the ghost-reflection SI technique to shallow subsurface field data. The retrieved ghost zero-offset section directly displayed the geometry of a layer at a depth of 4-6 m. The retrieved ghost zero-offset section allowed the interpretation of localised thinning within this specific layer. Using the ghost zero-offset section directly allows for such interpretations, as the retrieved ghost reflections depend kinematically only on the properties of the layer (or layers) that caused them to be retrieved. In this chapter, we also demonstrated that eliminating surface-related multiples in active-source gathers and muting undesired events before applying SI improves the retrieval of ghost reflections.

In Chapter 3, we presented the feasibility of monitoring pore-pressure changes in the Groningen gas field in the Netherlands through the application of ghost reflections. We retrieved ghost reflections that are exclusively sensitive to velocity changes inside the

reservoir, effectively eliminating the kinematic influence of the overburden and underburden. The monitoring surveys represented the changes in reservoir pore pressure to 30, 20, 10, and 5 MPa from the base survey value of 8 MPa. The time differences between the ghost reflection retrieved for the base survey and the four monitoring surveys were determined using a correlation operator. To effectively detect minor changes, we showed the importance of employing ghost reflections with increased temporal sampling (using interpolation) and retrieving ghost reflections for surface receivers illuminated optimally by sources from both sides of the receivers. We found that the geometry of the sources and receivers, the number of ghost sources and receivers, as well as the spacing between traces used for stacking for SI all play significant roles in ensuring clear retrieved ghost reflections.

In Chapter 4, we introduced the application of the relative amplitude of ghost reflections as a monitoring tool to detect small changes in the Groningen reservoir. We analysed the amplitude of ghost reflections retrieved using SI by autocorrelation (AC) applied to muted common-source gathers, SI by AC applied to separated reflections, SI by AC applied to normalised separated reflections, and using SI by trace deconvolution. We found the relative amplitude trends of the ghost reflections retrieved for both the base survey and monitoring survey to be consistent across these approaches. We showed that applying SI by AC using normalised separated reflections and applying SI by trace deconvolution, which are similar in the frequency domain, yield particularly promising results. Thus, detecting changes in the relative amplitude of ghost reflections, combined with their detected time shifts, could offer a precise tools to monitor small changes within reservoir, independent of overburden influences.

In Chapter 5, we discussed the application of SI for surface-wave suppression using land seismic data acquired in Scheemda, Groningen province, the Netherlands. Application of SI to retrieve dominant surface waves followed by adaptive subtraction, was proposed earlier, but only as a single iteration. Here, we showed that using a single iteration might suppress only part of the surface-wave energy. We thus proposed to apply the interferometric surface-wave suppression in an iterative way. We showed in this chapter that applying two iterations for retrieving surface waves through SI and adaptive subtraction yields better results in terms of clearer and continuous reflections compared to a single iteration. In comparison with other approaches for surface-wave suppression, such as surgical muting or frequency-wavenumber filtering, the recursive interferometric surface-wave suppression can be effective for enhancing the resolution of the reflections. The procedure we proposed in this chapter can serve as a standalone technique for suppressing surface waves or as a preceding step for retrieving ghost reflections or other reflection-based methods such as the Marchenko-redatuming method.

In Chapter 6, we demonstrated for the first time the application of the Marchenko-based isolation technique to land data using the reflection dataset employed in Chapter 5. We highlighted the importance of applying pre-processing steps to prepare the data for the application of the Marchenko redatuming. We demonstrated that after the application of the Marchenko-based isolation, the obtained common-source gathers and the resulting stacked sections exhibit cleaner images of the target zone compared to the results using the full reflection data. We emphasised the straightforward application of the Marchenko method to land seismic data using SH-wave surveys. The results of this

chapter can serve as a preprocessing step for removing primaries and internal multiples from the overburden and underburden for further application of other reflection-based methods, such as ghost-reflection retrieval.

In conclusion, we demonstrated the application of seismic data-driven methods for layer-specific characterisation using numerically modelled datasets of the shallow subsurface and deep structures and field datasets. The first three chapters focused on the retrieval of ghost reflections from SI. The main findings of these chapters are as follows:

- Applying SI to surface reflection data, ghost reflections are retrieved from the correlation of the primary reflections from the top and bottom of target layers.
- The ghost reflections can be used for layer-specific characterisation of the shallow subsurface or deep structures.
- The retrieved ghost reflections depend kinematically only on the properties of the layers that cause them to appear, without any influence from the layers above.
- The ghost reflections are sensitive to changes within the specific target layer(s): velocity changes, thickness changes, density changes, or a combination of these factors.
- Some preprocessing steps are required for the application of ghost-reflection retrieval, including surface-related multiple elimination, surface-wave suppression, or muting all other events except the specific primary reflections from the top and bottom of the target layers.
- The application of SI by AC results in zero-offset sections, while SI by cross correlation (CC) results in multi-offset sections. Ghost reflections resulting from SI by AC or SI by CC can be retrieved by turning receivers into virtual sources or active sources into virtual receivers. The choice would be dictated by the acquisition geometry of the available dataset.
- The interpretability resolution of the ghost reflections depends not only on the resolution of the reflection dataset but also on the geometry of the sources and receivers, the number of retrieved ghost sources and receivers, as well as the spacing between traces used for stacking in SI.
- When retrieving a strong ghost reflection from a specific layer is problematic, such as due to a thin layer above the target layers, it is possible to look at ghost reflections that propagate inside more than one layer.
- The stacked time or depth section of the original data can be used to interpret changes in ghost reflections by observing the specific primary reflections used for retrieval. However, it cannot be directly compared with the retrieved ghost reflections retrieved because these can only be observed in the virtual stacked section retrieved from SI.
- Relative amplitude changes and the time shift of the ghost reflections can serve as tools for monitoring specific small changes inside target reservoir.

The last two chapters focused on seismic data-driven techniques for enhancing the resolution of the reflection dataset, which can serve as standalone techniques or as preprocessing steps for the application of ghost reflection retrieval using land seismic data. Chapter 5 covered surface-wave suppression using SI, while Chapter 6 showcased the removal of primaries and internal multiples from the overburden and underburden using the Marchenko-based isolation technique. The main findings of these two chapters are as follows:

- Interferometric surface-wave suppression can be used to suppress effectively surface waves in land seismic datasets by applying SI to estimate surface waves followed by their adaptive subtraction from the original data.
- We proposed to apply these two steps recursively, i.e., several times (in our case twice), which results in a fully data-driven effective suppression of surface waves, yielding better results than a single application in terms of clearer and more continuous reflections.
- Considering some other processing steps in recursive interferometric surface-wave suppression, including bottom muting of the SI results, results in better preservation in the reflection energy after the interferometric surface-wave suppression.
- Using SH-wave seismic surveys and careful preprocessing steps, such as amplitude corrections and surface-wave suppression, creates a suitable dataset for applying the Marchenko-based isolation technique to land seismic datasets.
- The application of the Marchenko-based isolation to the target zone yields very promising results. It enhances the quality of the reflection data and provides a clearer image of the target zone with more continuous reflectors.

7.2. FUTURE OUTLOOK

This section will focus on the recommendations for future work on the seismic data-driven techniques discussed in this thesis. The recommendations for possibly improving these techniques are as follows:

- Chapters 2, 3, and 4 showed that eliminating the surface-related multiples and muting all other events except the specific primary reflections from the top and bottom of the target layer(s) results in clearer and more robust retrieved ghost reflections. However, internal multiples can also interfere with the target primaries used for ghost-reflection retrieval. Thus, application of the Marchenco redatuming for internal-multiple elimination from the overburden could be very useful and is recommended.
- Chapter 2 showed the application of ghost reflections for monitoring changes within the target layer, specifically focusing on velocity and thickness changes. However, ghost reflections are also sensitive to density changes in the target layer. Therefore, it is recommended to investigate ghost reflections for density changes or a combination of density, velocity, and thickness changes. This investigation should consider both time and amplitude changes.

- Chapter 2 showed that ghost reflections from SI by CC can also be retrieved, resulting in retrieved multi-offset gathers. It is recommended to use the results of SI by CC for velocity analysis to estimate the velocity inside specific layers.
- The impact of the stationary-phase region on retrieving clear ghost reflections was analysed qualitatively using the correlation gathers in Chapter 3 and 4. However, accurately defining the stationary-phase zone could be challenging. Thus, it is suggested to delve deeper into the stationary-phase region to better understand and potentially enhance the ghost reflections for both shallow subsurface and deep structures, which could greatly benefit field-data applications.
- Chapters 2, 3, and 4 demonstrated that ghost reflections can serve as a tool for monitoring changes in specific layers under various scenarios. It would be beneficial to apply the methodology of ghost reflection retrieval for time-lapse monitoring using field datasets, especially for CO_2 or H_2 storage.
- In Chapters 5 and 6, the application of SI for surface-wave suppression and the Marchenko method was demonstrated using a field dataset. However, it is recommended that this technique be applied to numerically modelled dataset that describes the field situation to further validate the results of these two techniques.
- In Chapter 5, it was demonstrated that higher modes of surface waves cannot be accurately kinematically retrieved using SI. Consequently, effectively suppressing these higher modes from the dataset poses a significant challenge. Further investigation into the suppression of higher modes using SI is recommended.
- In Chapter 5, the application of SI for surface-wave suppression was discussed. However, it is also recommended to utilise the same technique for surface-wave retrieval at each receiver, which would be beneficial in cases where more sources are needed, such as for full waveform inversion of surface waves.
- In Chapter 6, it was demonstrated that careful pre-processing is crucial to ensure a reflection response free from surface waves and surface-related multiples. Eliminating surface-related multiples is also recommended to further enhance the result of the Marchenko redatuming.
- A significant challenge when applying the Marchenko method to field data is ensuring the proper amplitude scaling of reflections to achieve convergence and, thus, effective multiple removal. Therefore, further investigation into the amplitude correction, particularly for land seismic data and SH waves, would be beneficial.
- In Chapter 6, unmigrated stacked sections were used for comparing the results using the full reflection response and the results after applying the Marchenko-based isolation technique. The application of advanced velocity analysis followed by prestack depth migration is recommended, with subsequent comparison of the migration results. This additional step could contribute to a more comprehensive understanding and improvement of the Marchenko-based isolation technique.

ACKNOWLEDGEMENTS

My PhD journey has been filled with amazing experiences and adventures, made possible by the incredible people I met and the unwavering support I received along the way. This journey was exciting because of them.

First and foremost, I want to express my sincere gratitude to my promotors, **Deyan Draganov** and **Kees Wapenaar** for their valuable support and guidance throughout the entirety of my PhD journey. **Deyan**, thank you for granting me the freedom to explore, fail, and succeed, while you were always available to support, guide, and steer me in the right direction. You helped me grow as an independent researcher, giving me the confidence to interpret results, ask questions, and recognize that challenges are not always as difficult as they seem— and, without a doubt, chocolate can help too! **Kees**, I still remember my first encounter with the world of seismic interferometry a few years before I started my PhD at TU Delft. It felt like magic to me then (and it still does!). At that time, your comprehensive responses to my simple questions were extremely helpful. As my promotor, your insights during our discussions and your detailed, critical review of my thesis have been invaluable. I will always be grateful for your guidance.

Throughout various stages of my PhD, I had the privilege of collaborating with many wonderful individuals in our section. I would like to thank **Ranajit Ghose** for our fieldwork in Scheemda and our intensive collaboration on seismic processing. I learned so much from you about the importance of every single piece of information in the data. **Jan Thorbecke**, your expertise and courses have been invaluable resources for every researcher, and I am incredibly thankful for all your guidance. **Eric Verschuur**, thank you for your incredible collaboration on two chapters. Your brilliant ideas helped push everything forward. **Auke Barnhoorn**, I appreciate your guidance during our lab experiments. **Kees Weemstra**, I am truly grateful for everything I learned from you. You and Deyan taught me how to effectively frame and structure research for publication.

In the summer of 2022, we conducted fieldwork in Scheemda, experiencing a heatwave, rain, cool windy weather, and intense work. Despite all the challenges, it was a fun and rewarding experience with all of you: **Ranajit, Deyan, Shohei, Eddy, Yusuke, Jingming, Jens** and **Yuan**. I would like to also thank **Aukje** and **Milad** for helping me in the lab and supporting our research. Thank you, **Johno**, for sharing your experiences with the Marchenko method, and **Florencia**, for the fascinating discussions on seismic interferometry. **Yusuke**, collaborating with you on retrieving surface waves was a pleasure. **Aydin**, thank you for all your explanations about the Marchenko method, and **Amin**, thank you for our scientific discussions and for sharing your knowledge.

Without a doubt, one of the key figures who guided me throughout my journey in geophysics, during my bachelor's studies and afterwards, is **Mohsen Eliassi**. You were right: it is worth pursuing what you love. I would like extend my gratitude to several important individuals: **Mohammad Reza Hatami, Ahmad Sadidkhoy**, and **Ali Moradi**. I will never forget your support in shaping my path as a researcher.

I feel incredibly fortunate to have worked on the same project and shared an office with such wonderful people. I truly believe that a positive and friendly environment makes everything more enjoyable. Thank you, Aukje, Milad, Jingming, Aleks, Iban, Hamed, Samantha, and Sara. **Aukje**, you motivated me to come in early, and I am grateful for all the information you shared about Dutch culture, life in the Netherlands, and everything in between. **Jingming**, I will always remember our morning coffee talks with you and Aukje, as well as all your efforts to keep the plants in our office alive. **Iban**, thank you for that beautiful picture of all of us in the DeepNL office; it will always remind me of you and our time there. **Hamed**, your enthusiasm for learning and hard working is inspiring. **Aleks**, thank you for sharing the wall in front of you for putting up those quotes. I know how distracting it can be, but you manage it well! And **Milad**, thank you for the positivity and energy you bring to our office, especially your unique taste in office decoration. It really makes a difference!

I want to express my sincere gratitude to my friends and colleagues. Our time together during lunches, coffee gatherings, and conversations has enriched my day. Thank you all: **Azin, Alireza, Andrea, Billy, Boris, Camille, Eddy, Eli, Entela, Evgeniia, Fardad, Joeri, Jasper, Jianhuan, IIshat, Lukas, Mahnaz, Martha, Maria, Marat, Mahmoud, Menno, Mohammad, Musab, Parvin, Sepi, Shihao, Siamak, Sverre,** and **Wen**. Special thanks to my new colleagues in the office: **David, Lada, Rick, Fan**, and **Jordan** for their friendly, positive energy and the fresh vibe they bring. I would also like to express my gratitude to the support staff of the department, **Marlijn**, **Ralf**, **Lydia** and **Barbara**, for their kindness and assistance.

It is always good to have people with whom you can share your failures and successes, knowing they will support and empower you. Thank you, **Atiyeh**, **Ebrahim**, and your adorable little one, **Elena**. You are truly my family. I also want to express my gratitude to my old friends. Even though we are far apart, your video calls have made me feel close. **Pegah, Shima, Maryam, Elham, Najmieh**, and **Toktam**, you have shown me that distance does not matter when it comes to friendship.

Special thanks to my family; you are my greatest treasure. **Leila** and **Atefeh**, you are incredible sisters, and I am so lucky to have you both by my side. To my nieces, **Mobina**, **Zeinab**, and **Zahra**, our video calls always provide the best breaks. And my nephew, **MohammadHossein**, throughout these years, you have been the only one who could completely disconnect me from the real world with your funny jokes and endless entertaining conversations.

To my beloved parents, **(maman) Khojasteh** and (**baba) Ahmad** words cannot fully express the depth of my gratitude for everything you have done for me. Your unwavering support and boundless kindness have given me the strength to overcome challenges and pursue my dreams. Thank you for being my guiding light and for always being there for me.

Finally, my endless love and gratitude go to **Morteza**. Your belief in me has opened doors I never thought possible, and your support and encouragement inspire me daily. I cherish every moment we share and look forward to the exciting adventures that await us in the years ahead.

CURRICULUM VITÆ

Faezeh SHIRMOHAMMADI

01-06-1989 Born in Tehran, Iran.

EDUCATION AND EXPERIENCES

2007–2011 B.Sc. Geology
University of Tehran, Iran

2011–2014 M.Sc. Geophysics
University of Tehran, Iran

2014–2018 Researcher, Geophysics
University of Tehran, Iran

2018–2019 Visiting researcher, Geophysics
Delft University of Technology, the Netherlands

2019–2024 Ph.D. Applied Geophysics
Delft University of Technology, the Netherlands
Thesis: Layer-specific imaging and monitoring using seismic interferometry and the Marchenko method
Promotors: Dr. ir. D.S. Draganov
Prof. dr. ir. C.P.A. Wapenaar

PUBLICATIONS

LIST OF PUBLICATIONS

5. **F. Shirmohammadi**, D. Draganov, J. IJsseldijk, R. Ghose, J. Thorbecke, E. Verschuur, & K. Wapenaar, *Application of Marchenko-based isolation to a land S-wave seismic dataset*, Submitted to Geophysical Prospecting, preprint available on arXiv: arXiv:2304.09956 (2024).

4. **F. Shirmohammadi**, D. Draganov, & R. Ghose, E. Verschuur, & K. Wapenaar, *Recursive interferometric surface-wave suppression for improved reflection imaging*, under preparation, preprint available on arXiv: arXiv.2411.02620 (2024).

3. **F. Shirmohammadi**, D. Draganov, A. Veltmeijer, M. Naderloo,& A. Barnhoorn, *Feasibility of reservoir monitoring in the Groningen using ghost reflections from seismic interferometry*, Geophysical journal International **237(2)**, (2024).

2. **F. Shirmohammadi**, D. Draganov, & R. Ghose, *The utilization of ghost reflections retrieved by seismic interferometry for layer-specific characterization of the shallow subsurface*, Near Surface Geophysics **22**, (2024).

1. **F. Shirmohammadi**, D. Draganov, M.R. Hatami, & C. Weemstra, *Application of seismic interferometry by multidimensional deconvolution to earthquake data recorded in Malargüe, Argentina*, Remote Sensing **13(23)**, (2021).

LIST OF CONFERENCE PROCEEDINGS

8. **F. Shirmohammadi**, D. Draganov, J. IJsseldijk, R. Ghose, J. Thorbecke, E. Verschuur, & K. Wapenaar, *Application of Marchenko-based isolation to a land seismic dataset*, 85th EAGE Annual Conferenc (2024).

7. **F. Shirmohammadi**, D. Draganov, A. Veltmeijer, M. Naderloo, & A. Barnhoorn, *Monitoring pore-pressure depletion in the Groningen reservoir using ghost reflections from seismic interferometry*, 84th EAGE Annual Conference & Exhibition Workshop Programme (2023).

6. **F. Shirmohammadi**, & D. Draganov, *Surface-waves suppression using seismic interferometry for imaging and monitoring of the Groningen subsurface*, Nederlanders Aardwetenschappelijk Congres (2023).

5. **F. Shirmohammadi**, D. Draganov, F. Balestrini, & R. Ghose, *Application of seismic interferometry with non-physical reflections using near-surface seismic field data*, NSG2022 28th European Meeting of Environmental and Engineering Geophysics (2022).

4. **F. Shirmohammadi**, D. Draganov, P. Ras, & K. Wapenaar, *Layer-specific imaging and monitoring in the Groningen subsurface using seismic interferometry*, EGU General Assembly (2022).

3. **F. Shirmohammadi**, D. Draganov, & K. Wapenaar, *Monitoring changes in the Groningen subsurface using non-physical arrivals in seismic interferometry*, Nederlanders Aardwetenschappelijk Congres (2021).

2. **F. Shirmohammadi**, D. Draganov, & K. Wapenaar, *Monitoring changes inside subsurface layers using non-physical reflections retrieved from seismic interferometry*, Nederlanders Aardwetenschappelijk Congres (2020).

1. **F. Shirmohammadi**, D. Draganov, C. Weemstra, & K. Wapenaar, *Application of seismic interferometry by multidimensional deconvolution to earthquakes data recorded in Malargüe, Argentina*, EGU General Assembly (2019).